

Magnetic field distribution and relaxation effects  
in the presence of interstitial and intracellular  
contrast agents for magnetic resonance imaging

DISSERTATION

zur Erlangung des Grades eines Doktors  
der Naturwissenschaften

der Fakultät für Mathematik und Physik  
der Eberhard-Karls-Universität zu Tübingen

vorgelegt von

**Jörg Pintaske**

aus Marienberg

2007

Tag der mündlichen Prüfung:	14. Februar 2007
Dekan:	Prof. Dr. Nils Schopohl
1. Berichterstatter:	Prof. Dr. Dr. Fritz Schick
2. Berichterstatter:	Prof. Dr. Reinhold Kleiner

# Abstract

## Introduction and objective

For many diagnostic tasks the inherent soft-tissue contrast is sufficient to distinguish different tissues on Magnetic Resonance Imaging (MRI) without the need for exogenous contrast agent. However, the native contrast between different tissues is not always sufficient to distinguish or characterize pathologic changes unambiguously. In order to enhance the contrast between normal and diseased tissue, and hence to improve the likelihood of detecting tumors or lesions associated with the tissue, MRI benefits from dedicated contrast agents.

By far the most commonly employed contrast media are based on the paramagnetic properties of gadolinium (Gd). The distribution of this agent is the extracellular or interstitial space. Gd based contrast media primarily affect longitudinal ( $T_1$ ) and transversal ( $T_2$ ) relaxation mechanism and, hence, induce measurable changes in the image contrast. Often they are used to reveal tissue perfusion characteristics by means of MRI.

Furthermore, exploiting the capability of certain cell types to ingest superparamagnetic iron oxide (SPIO) nanoparticles through phagocytosis the *in vivo* labeling of macrophages has been used for the detection and delineation of focal lesions associated with tissue. In contrast to Gd based contrast agents, due to large magnetic moments, iron oxide particles generate intense field inhomogeneities over fairly large distances. Thus, labeled cells have significant effects on MRI signal dephasing induced in water molecules near the cells. In practice, labeled cells are reflected either as low-intensity signal spots or signal voids, particularly in  $T_2^*$ -weighted gradient echo MRI. In addition to the administration of SPIO for organ-specific MRI, the transplantation or transfusion of *ex vivo* labeled cells in living organism has led to a growing research interest to monitor the cellular biodistribution *in vivo* by means of MRI including stem cell migration.

The purpose of this work was to achieve a profound and systematic understanding of magnetic susceptibility and relaxation effects of interstitial and intracellular contrast agents in MRI. The emphasis was on the investigation of relaxation and field inhomogeneity effects due to magnetically labeled cells and to exploit these effects to develop MR techniques for cell detection.

## Materials and methods

*In vitro* measurements of longitudinal ( $R_1$ ) and transversal relaxation rates ( $R_2$ ,  $R_2^*$ ) of extracellular contrast agents in human blood plasma and cells labeled with intracellular

## ABSTRACT

contrast agents were conducted. For the latter experiments, proper preparation techniques of labeled cells in agar gel suspensions were developed and evaluated. This allowed studying concentration effects of labeled cells on the magnetic field distribution and relaxation in isolation. The measurements were performed on MRI whole-body systems operating at 0.2, 1.5, and 3 Tesla.

Magnetic field inhomogeneity effects of magnetic dipoles, magnetic material and labeled cells were studied by means of a three-dimensional numerical model simulating magnetostatics. This model was developed in order to study both microscopic as well as macroscopic magnetic field distortions related to paramagnetic and superparamagnetic contrast media, and magnetically labeled cells. Various geometries of intracellular particle distributions were scrutinized and the extracellular field distortions were computed. Effects of the spatial distribution of magnetic material on the intravoxel Larmor frequency distribution and static MR signal decay were assessed. This comprised the investigation of magnetic field perturbations in liver tissue after SPIO injection and in case of pathological liver iron overload as well as in case of division of labeled cells.

Macroscopic magnetic field inhomogeneities due to aggregations of labeled cells were studied by means of simulations and MR measurements. The effects on spatial accuracy and sensitivity in MRI of labeled cells were addressed, and implications for the quantification of labeled cells were worked out. A proper preparation technique was developed in order to quantify effects related to aggregations of SPIO particles as well as cluster of magnetically labeled cells under well-defined experimental conditions in vitro.

In further experiments, the inhomogeneous spectral broadening due to labeled cells was exploited to achieve selective imaging of labeled cells by means of an alternative 'positive contrast'. For this purpose, the principle of spectral selective saturation was developed. Frequency selective radiofrequency pulses with varying bandwidth were implemented in a spin echo sequence. This technique was evaluated in vitro applying proper preparations of samples containing low cell concentrations, reflecting a homogeneous cell distribution in tissue, or cluster of labeled cells, reflecting tissue-specific cell aggregations.

## Results

As measured in suspensions of magnetically labeled cells, a significant dependency between cellular transverse relaxation enhancement and cell concentration was found for all field strengths investigated. Specifically, a linear relationship could be revealed. The gradient echo sequences demonstrated higher transverse cellular relaxivities as compared to spin echo sequences. Similar results were found for extracellular contrast media.

As based on numerical simulations, the magnetic field created by a magnetically labeled cell is sensitive to its shape and intracellular distribution of magnetic moments only in close proximity to the cell. Far from the cell, the effects of the intracellular particle distribution are less pronounced, but depend on the cell's magnetization.

The effect of the intravoxel spatial distribution of a constant amount of magnetic material was investigated. For larger randomly distributed magnetic aggregations non-Lorentzian frequency distributions and non-monoexponential signal decay were found whereas, for

## ABSTRACT

smaller aggregations, the frequency distribution was more Lorentzian and the signal decay was well fitted monoexponentially.

The signal void characteristics, induced by aggregations of magnetically labeled cells, were scrutinized systematically for fundamental sequence parameters including echo time, voxel size, and image orientation, using numerical simulations based on magnetostatics. For all variables examined significant changes in geometry as well as extension of signal void were found. The diameter of signal void varied non-linearly with magnetization, cell concentration, echo time, and voxel size. These dependencies were verified under in vitro conditions applying proper experimental set ups. In addition, the quantification of magnetically labeled cells with respect to the diameter of the induced image signal void was achieved in vitro.

Furthermore, the Larmor frequency shift near labeled cells was exploited to obtain bright visualization applying spectral selective saturation pulses. This radiofrequency preparation was used to suppress the on-resonance water signal. The off-resonance water signal surrounding the labeled cells contributed to the MR image, so that only the fluid immediately adjacent to the labeled cells was visible in the MR image. Positive contrast imaging was achieved for volume elements containing labeled cells as well as for volume elements close to cell cluster. This led to an alternative contrast and provided significant improvements in image contrast.

## Discussion and conclusions

This work contributes to the better understanding of relaxation and magnetic susceptibility effects in MRI induced by extracellular or interstitial contrast agents and by cells labeled with iron oxide nanoparticles. The relaxation effects and magnetic field distortions were studied systematically for distances smaller than the MRI voxel size (i.e., the microscopic scale) as well as for distances larger than the imaging voxel (i.e., the macroscopic scale). It was demonstrated, that signal dephasing effects and Larmor frequency shifts can be exploited to generate various kinds of image contrast in presence of interstitial and intracellular contrast agents.

Relaxation effects of intra- and extracellular contrast agents were studied systematically for various concentrations of contrast agents and at different magnetic field strengths. In order to improve the image contrast or to optimize the sensitivity and the specificity of MRI to detect magnetically labeled entities, such a systematic study is crucial to establish optimal parameters for MR pulse sequences at each magnetic field strength.

Studying field inhomogeneity effects is of major importance in MRI, because field gradients cause dephasing of the transverse magnetization. It was demonstrated, that different spatial arrangements of magnetic material in combination with intracellular contrast agents produce characteristic changes in the local magnetic field distribution and, hence, in MR signal dephasing.

In addition, the present work contributes to the understanding of the geometry as well as the extension of signal voids in gradient echo MRI induced by aggregations of magnetically labeled cells. In order to study the physical characteristics of these signal voids, basic sequence parameters like echo time, voxel size, and plane of view orientation have been varied over a wide range in numerical simulations and in vitro MR measurements. The results

## *ABSTRACT*

are considered to be of importance in optimizing MR sequence parameters with regard to spatial accuracy and sensitivity to detect cluster of labeled cells in vitro or even in vivo.

The findings of this work, both experimental data and data obtained from numerical simulations, are anticipated to be transferable to each type of cell, since the physics describing magnetic susceptibility, relaxation and signal dephasing effects is indifferent to cell type. Furthermore, the theoretical and the in vitro findings are anticipated to apply under in vivo conditions, since the underlying physical principles are comparable.

# Zusammenfassung

## Einleitung und Zielstellung

Für eine Vielzahl diagnostischer Fragestellungen ist der inhärente Weichteilkontrast der Magnetresonanztomographie (MRT) ausreichend, um gesunde Gewebe auch ohne eine zusätzliche Medikation mit exogenen Kontrastmitteln differenzieren zu können. Jedoch ist der erreichbare Kontrast oft nicht ausreichend, um pathologische Veränderungen im Gewebe eindeutig charakterisieren zu können. Um den Bildkontrast in der MRT zwischen Normalgewebe und krankhaft verändernden Gewebe zu verbessern, werden oft dedizierte Kontrastmittel eingesetzt.

Viele der üblicherweise einsetzbaren MR Kontrastmittel basieren auf den paramagnetischen Eigenschaften von Gadolinium (Gd). Die Verteilung derartiger Kontrastmittel erfolgt im extrazellulären oder interstitialen Raum. Gadolinium-basierende Kontrastmittel beeinflussen die Relaxationsprozesse und führen zu einer Verkürzung der Relaxations-Zeitkonstanten. Oft finden diese Kontrastmittel Anwendung in der Charakterisierung der Gewebeperfusion mittels MRT.

Zur Erhöhung der Spezifität werden häufig superparamagnetische (SPIO; superparamagnetic iron oxide) MR Kontrastmittel eingesetzt, welche sich nach intravenöser Applikation in speziellen Zelltypen des mononukleären phagozytierenden Systems der Leber, Milz, Lymphknoten und des Knochenmarks anreichern. Es ist aber auch möglich, verschiedene Zelltypen (z.B. hämatopoetische Stammzellen) bereits ex vivo mit SPIO zu markieren, um die Migrationswege markierter Zellen mittels MRT nach Injektion oder Transplantation der Zellen zu erfassen. Im Unterschied zu herkömmlichen, hauptsächlich  $T_1$ -verkürzenden Kontrastmitteln wie paramagnetischen Gd-Chelaten bewirkt das große magnetische Moment superparamagnetischer Verbindungen eine relativ weit reichende Verzerrung des statischen Grundmagnetfeldes. Diese Störungen der lokalen Feldverteilung führen bei entsprechender Stärke zu messbaren Verkürzungen der Zeitkonstanten  $T_2$  in Spinecho- und  $T_2^*$  in Gradientenecho-Sequenzen bzw. zu Signalauslöschungen.

Das Anliegen dieser Arbeit war ein systematisches Verständnis der Einflüsse der magnetischen Suszeptibilität und der Relaxivität interstitialer und intrazellulärer Kontrastmittel in der MRT. Schwerpunkte lagen auf der Untersuchung der Relaxations- und Feldstörungseffekte in Gegenwart markierter Zellen und darauf basierender methodischer Ansätze zu deren Nachweis.

## Material und Methoden

In vitro Messungen longitudinaler ( $R_1$ ) und transversaler Relaxationsraten ( $R_2$ ,  $R_2^*$ ) verschiedener extrazellulärer Kontrastmittel in menschlichem Blutplasma und magnetisch markierter Zellen wurden durchgeführt. Um Relaxations- und Feldstörungseffekte verschiedener Konzentrationen markierter Zellen von anderen Einflussfaktoren isoliert untersuchen zu können, wurden geeignete Präparationen magnetisch markierter Zellen in Gelsuspensionen hergestellt. Die Messungen erfolgten an MR Ganzkörpertomographen der magnetischen Induktion 0.2, 1.5, und 3 Tesla.

Magnetfeldinhomogenitäten durch magnetische Dipole, magnetischen Materials und magnetisch markierte Zellen wurden in einem dreidimensionalen numerischen Modell der Magnetostatik studiert. Dieses wurde etabliert, um mikroskopische als auch makroskopische Feldstörungseffekte durch paramagnetische und superparamagnetische Kontrastmittel als auch durch magnetisch markierte Zellen zu untersuchen. Verschiedene intrazelluläre Verteilungsmuster magnetischer Partikel wurden simuliert und die daraus resultierende extrazelluläre Feldverzerrung berechnet. Weitere Simulationen betrachteten die Einflüsse der räumlichen Verteilung magnetischen Materials auf die Intravoxel-Verteilung der Resonanzfrequenzen und den MR-Signalzerfall. Dies beinhaltete die Simulation der Feldverteilungen in Gewebe nach SPIO Injektion, im Falle einer Eisenüberbeladung im Gewebe und im Falle der Zellteilung magnetisch markierter Zellen.

Makroskopische Magnetfeldinhomogenitäten durch Aggregationen markierter Zellen wurden berechnet und mittels MR Messungen überprüft. Die Einflüsse auf die Abbildungsgenauigkeit, die Sensitivität und die Quantifizierung markierter Zellen wurden herausgearbeitet. Dafür wurde eine geeignete Präparationstechnik zur systematischen Untersuchung von Aggregationen magnetischer Partikel und magnetisch markierter Zellen unter in vitro Bedingungen entwickelt.

Weitere Experimente nutzten die spektrale Verbreiterung der Wasserresonanz bei Anwesenheit markierter Zellen zur selektiven Abbildung der Zellen mittels ‚positivem Kontrast‘. Das Prinzip der spektral selektiven Sättigung wurde entwickelt und dafür geeignete frequenzselektive Hochfrequenzpulse in eine Spinechosequenz implementiert. Die Methodik wurde an passenden in vitro Prüfkörpern evaluiert: gleichmäßige Verteilungen markierter Zellen, welche eine homogene Verteilung im Gewebe repräsentierten, und lokalisierte Cluster markierter Zellen, welche spezifische Aggregationen magnetischen Materials im Gewebe widerspiegeln.

## Ergebnisse

Die Messungen in Suspensionen magnetisch markierter Zellen zeigten bei allen untersuchten Feldstärken eine signifikante Abhängigkeit transversaler Relaxation und Signaldephasierung bezüglich der Zellkonzentration. Im Speziellen konnte dieser Zusammenhang im betrachteten Konzentrationsbereich als linear dargestellt werden. Gradientenechosequenzen demonstrierten dabei wesentlich höhere Werte transversaler Relaxivität als Spinechosequenzen. Äquivalente Ergebnisse ergaben sich in den Messungen mit extrazellulären Kontrastmitteln.



## ZUSAMMENFASSUNG

Die numerischen Simulationen zeigten, dass die Magnetfeldstörung markierter Zellen nur in unmittelbarer Umgebung zur Zelle von der intrazellulären Verteilung der Partikel beeinflusst wurde. Mit zunehmender Entfernung waren geringere Einflüsse der intrazellulären Partikelverteilung auf die extrazelluläre Feldverzerrung nachweisbar.

Für größere, statistisch gleichverteilte Aggregationen magnetischen Materials zeigten sich nicht-lorentzförmige Frequenzverteilungen und nicht-monoexponentielle Signalzerfälle. Dagegen konnten für kleinere Aggregationen, bei gleicher Volumenkonzentration magnetischen Materials im Voxel, in guter Näherung lorentzförmige Frequenzverteilungen und ein monoexponentielles Signalverhalten beobachtet werden.

Die MR Signalauslöschungen wurden systematisch für fundamentale Sequenzparameter wie Echozeit, Ortsauflösung, und Schichtorientierung untersucht. Für alle betrachteten Variablen wurden signifikante Änderungen in Ausdehnung und Geometrie der Signalauslöschung aufgezeigt. Eine nicht-lineare Zunahme im Durchmesser der Signalauslöschung mit der Magnetisierung, der Zellkonzentration, der Echozeit und der Voxelgröße wurde beobachtet. Die *in vitro* Experimente ermöglichten eine Quantifizierung markierter Zellen über die Größe der Signalauslöschung mittels geeigneter Präparation der Zellen in einem Probekörper.

Des Weiteren wurde die Verschiebung der Larmorfrequenzen durch markierte Zellen zur Visualisierung der Zellen über eine Signalaufhellung in Sequenzen mit frequenzselektiven Sättigungspulsen verwendet. Die Präparationspulse erlaubten, die unverschobenen Frequenzanteile der Wasserresonanz zu unterdrücken. Dagegen konnten die durch markierte Zellen verschobenen Frequenzanteile zum MR Signal beitragen, so dass die Volumenanteile in unmittelbarer Nähe zur markierten Zelle selektiv im MR Tomogramm abgebildet wurden. Positiver Kontrast wurde sowohl für Volumenelemente mit markierten Zellen als auch für solche Volumenelemente erzielt, welche sich in unmittelbarer Nähe zu Zellaggregationen befanden. Dies führte zu einer deutlichen Verbesserung im Bildkontrast unter *in vitro* Bedingungen.

## Diskussion und Schlussfolgerung

Diese Arbeit trägt zu einem besseren Verständnis der Einflüsse der magnetischen Suszeptibilität und der Relaxation in der MRT durch extrazelluläre oder interstitiale Kontrastmittel und mit Eisenoxidpartikeln markierten Zellen bei. Relaxationseffekte und Magnetfeldstörungen wurden systematisch innerhalb der Bildelemente (mikroskopische Größenordnung) und auf der Ebene der Bildelemente und darüber (makroskopische Größenordnung) untersucht. Es konnte gezeigt werden, dass die durch paramagnetische/superparamagnetische Kontrastmittel bedingte verstärkte Signaldephasierung und die Verschiebungen der Resonanzfrequenzen zur Erzeugung von Bildkontrasten ausgenutzt werden können.

Relaxationseffekte verschiedener Konzentrationen intra- und extrazellulärer Kontrastmittel wurden systematisch bei unterschiedlichen Feldstärken untersucht. Mit der Zielsetzung, den Bildkontrast zu verbessern sowie die Sensitivität und Spezifität der MRT zum Nachweis magnetisch markierter Zellen zu optimieren, ist eine derartige systematische Untersuchung notwendig. Ziel ist dabei eine möglichst optimale Wahl der Sequenzparameter bei jeder Feldstärke zu treffen.

## ZUSAMMENFASSUNG

Das Studium der Feldverzerrungen ist von grundlegender Bedeutung für die MRT, da die Präzessionsfrequenz der magnetischen Kernmomente in Gegenwart von Feldgradienten verändert ist. Es wurde demonstriert, dass eine unterschiedliche Verteilung des magnetischen Materials lokale Störungen in der Magnetfeldverteilung bedingt. Damit verbunden sind charakteristische Veränderungen in der Signaldephasierung.

Zusätzlich trägt diese Arbeit zum Verständnis der Geometrie und der Ausdehnung der mittels Aggregationen markierter Zellen induzierten Signalauslöschungen in der Gradientenecho-Bildgebung bei. Um die physikalischen Ursachen der beobachtbaren Signalauslöschungen zu verstehen, wurden Sequenzparameter wie Echozeit, Voxelgröße und Schichtorientierung über einen großen Bereich variiert. Die numerischen Simulationen wurden mittels *in vitro* Messungen verifiziert. Diese Ergebnisse werden als grundlegend erachtet, um Sequenzparameter hinsichtlich Abbildungsgenauigkeit und Sensitivität im Nachweis von Aggregationen markierter Zellen, sowohl *in vitro* als auch *in vivo*, zu optimieren.

Die auf theoretischen und experimentellen Untersuchungen basierenden Erkenntnisse dieser Arbeit sollten für jeden Typ einer markierten Zelle zutreffend sein. Dies begründet sich aus den allgemeinen physikalischen Prinzipien, welche die Einflüsse der magnetischen Suszeptibilität, der Relaxation und der Signaldephasierung in der MRT in Gegenwart intrazellulärer Kontrastmittel determinieren. Des Weiteren ist die Übertragung der Erkenntnisse auf *in vivo* Situationen grundsätzlich möglich, da auch hier die zugrunde liegenden physikalischen Phänomene in guter Näherung vergleichbar sind.

# Contents

1	Introduction and objectives .....	1
2	Physical basics .....	5
2.1	Principle of Nuclear Magnetic Resonance .....	5
2.2	Bloch equations and relaxation.....	7
2.3	Magnetic susceptibility and magnetic field inhomogeneities.....	10
2.3.1	Magnetic susceptibility	
2.3.2	Magnetic field inhomogeneities	
2.4	Diffusion regimes .....	14
2.4.1	Bloch-Torrey equation	
2.4.2	Characterization of diffusion regimes	
2.5	MR signal formation in the static dephasing regime .....	19
3	Relaxivities of intra- and extracellular contrast agents .....	23
3.1	Physical and biological background .....	23
3.1.1	Interstitial or extracellular contrast agents	
3.1.2	Intracellular contrast agents - Magnetically labeled cells	
3.2	Measurement of relaxation rates and relaxivities .....	30
3.2.1	Measurement of the longitudinal relaxation rate $R_1$	
3.2.2	Measurement of the transverse relaxation rates $R_2$ and $R_2^*$	
3.2.3	Determination of relaxivities of contrast media	
3.3	Materials and methods.....	36
3.3.1	Relaxivity of gadolinium contrast agents in human blood plasma	
3.3.2	Relaxivity of iron oxide labeled human melanoma cells	
3.4	Results of relaxivity measurements .....	44
3.4.1	Relaxivity of gadolinium contrast agents in human blood plasma	
3.4.2	Relaxivity of iron oxide labeled human melanoma cells	
3.5	Interpretation of the results .....	51
3.5.1	Relaxivity of gadolinium contrast agents in human blood plasma	
3.5.2	Relaxivity of iron oxide labeled human melanoma cells	

4	Microscopic intra- and extracellular magnetic field inhomogeneities.....	56
4.1	Physical and biological background .....	56
4.2	3d numerical model .....	58
4.3	Materials and methods .....	63
4.3.1	Magnetic field distortion around magnetically labeled cells	
4.3.2	Spatial distribution of magnetic material	
4.4	Numerical simulations .....	68
4.4.1	Magnetic dipole field	
4.4.2	Magnetic field distortion around magnetically labeled cells	
4.4.3	Effect of spatial distribution of magnetic material	
4.5	Interpretation of the results .....	74
4.5.1	Magnetic field distortion around magnetically labeled cells	
4.5.2	Effect of spatial distribution of magnetic material	
5	Macroscopic extracellular magnetic field inhomogeneities .....	78
5.1	Physical and biological background .....	78
5.2	Materials and methods .....	79
5.2.1	Numerical simulations	
5.2.2	MR measurements	
5.3	Numerical and experimental results .....	89
5.3.1	Simulations on geometry and extension of signal voids in MR images	
5.3.2	Quantitative investigation of SPIO-containing solutions and SPIO-labeled cells	
5.4	Interpretation of the numerical and the experimental results .....	95
5.4.1	Spatial accuracy in MRI of magnetically labeled cells	
5.4.2	Sensitivity in MRI of magnetically labeled cells	
5.4.3	Relevance for cell quantification	
5.4.4	Limitations of the numerical model	
6	Positive contrast MRI of magnetically labeled cells .....	100
6.1	Introduction .....	100
6.2	Materials and methods.....	102
6.2.1	Frequency selectivity of radiofrequency pulses	
6.2.2	Principle of spectrally selective saturation	
6.2.3	Pulse sequence timing	
6.2.4	Preparation of cell samples	
6.2.5	MR measurements	
6.3	Results ..	111
6.3.1	Fat-water phantom	
6.3.2	Low concentrations of magnetically labeled cells	
6.3.3	Aggregations of magnetically labeled cells	
6.4	Interpretation of the results .....	114

*CONTENTS*

7	Discussion and conclusions.....	118
i.	References .....	123
ii.	Journal papers .....	133
iii.	Curriculum vitae .....	135
iv.	Danksagung .....	136

## Chapter 1

# Introduction and objectives

The Nuclear Magnetic Resonance (NMR) phenomenon was observed in bulk matter independently by Felix Bloch et al. at Stanford [Blo46] and Edward Purcell et al. at Harvard [Pur46] in 1946. NMR involves atomic nuclei (spin  $\neq 0$ ) of macroscopic objects, strong and static magnetic fields (about  $10^4 - 10^5$  times the earth's magnetic field), oscillating magnetic fields, and the resonance phenomenon due to the interactions of the atomic nuclei with the magnetic fields. Since then, two main applications of NMR have been evolved: NMR spectroscopy and magnetic resonance imaging. NMR spectroscopy utilizes high field spectrometer (up to a magnetic induction  $B_0$  of 21.1 Tesla, resonance frequency 900 MHz for  $^1\text{H}$  [Buck04]) for the chemical analysis of liquid and solid specimen.

Magnetic resonance imaging (MRI) is a tomographic imaging technique that produces diagnostic images of inherent physical characteristics of an object from externally measured and spatially encoded NMR signals [Dam71, Lau73, Man73]. MRI operates in the radio-frequency range (wavelength  $\approx 10^0$ - $10^2$  m, energy  $\approx 10^{-6}$ - $10^{-8}$  eV). The imaging procedure does not involve the use of ionizing radiation. Nevertheless, safety issues are important aspects in MRI. Regulatory agencies such as the Food and Drug Administration (FDA) revise proper safety limits with respect to potential bioeffects induced by static magnetic fields, gradient fields and radiofrequency fields [US03].

MRI for clinical use is an ever-improving technology towards higher speed (ultra-fast imaging, parallel imaging), higher resolution (microimaging), and more diagnostic information due to combined anatomical, metabolic, and functional imaging. The combination of MRI with other imaging modalities (e.g., positron-emission-tomography) is aspired.

MRI can non-invasively produce images from any biological system revealing structure, metabolism or function of internal tissues and organs. In general, the image signal intensity is dependent on a host of intrinsic variables including nuclear spin density, the relaxation time constants  $T_1$  ('spin-lattice relaxation') and  $T_2$  ('spin-spin relaxation'), molecular motion such as diffusion and perfusion, chemical shift differences, and magnetic field inhomogeneities due to magnetic susceptibility gradients. By the proper choice of the sequence design and the sequence parameters the MR images can be weighted with respect to certain variables, such as  $T_1$ -weighted images or susceptibility weighted images.

There are numerous sources of magnetic field variation in the body. Some are problematic such as those caused by internal susceptibility differences between tissues (e.g., tissue-air interfaces in the lung), which may cause severe image distortions, precluding for the extraction of diagnostic information in that case. On the other hand, local variations in magnetic susceptibility refer to special properties or metabolic states of the body, including the tissue structure and the oxygenation level of red blood cells [Paul36, Oga90]. The latter is used as a measure for localized brain activity and characterization of tissue and tissue compartments.

For many diagnostic tasks the inherent soft-tissue contrast is sufficient to distinguish different tissues on MRI without the need for exogenous contrast agent. However, the native contrast between different tissues is not always sufficient to distinguish or characterize pathologic changes unambiguously. In order to enhance the contrast between normal and diseased tissue, and hence to improve the likelihood of detecting tumors or lesions associated with the tissue, MRI benefits from dedicated contrast agents. By far the most commonly employed contrast media are based on the paramagnetic properties of gadolinium, with the agent being distributed in the extracellular space. Furthermore, exploiting the capability of certain cell types to ingest iron oxide nanoparticles through phagocytosis (i.e., intracellular contrast

agents) the in vivo labeling of macrophages has been used for the detection and delineation of focal liver lesions.

In addition to the application in organ specific MRI, superparamagnetic iron oxide nanoparticles are currently used for the trafficking of labeled cells such as stem cells [Stroh05]. Due to the limited spatial resolution, MRI is in fact not capable to visualize single labeled cells in the body. However, the high magnetic moment of iron oxide particles generates intense field inhomogeneities. Thus, in MRI ex vivo magnetically labeled cells produce signal loss in regions where they are deposited or to which they have migrated [Hoe02]. Whereas most of these experimental studies to date have been mere the ‘proof of principle’, further exploitation of this technique will provide deeper insight into the dynamics of cell homing, cancer cell migration, and the monitoring of stem cell based therapies. The results of the first clinical trials using ex vivo magnetically labeled cells have been published previously [DeVr05].

## Thesis’ purpose

The application of iron oxide nanoparticles to monitor the migration pathways of ex vivo labeled cells by means of MRI is an emerging field of research. However, a coherent understanding of the various effects of labeled cells in MRI has not been achieved so far. The objective of this work was to study magnetic susceptibility and relaxation effects of intra- and extracellular contrast agents in magnetic resonance imaging, providing the basis for the proper interpretation of experimental results under in vivo conditions.

The main emphasis was on the profound and the systematic understanding of magnetic field inhomogeneity effects of magnetically labeled cells at both the microscopic and the macroscopic scale. These effects were exploited to generate various kinds of image contrast in MRI. A numerical model was developed in order to study magnetic field inhomogeneity effects related to magnetic particles as well as magnetically labeled cells. Different techniques to prepare proper cell phantoms were devised and in vitro MR measurements were conducted. Furthermore, an alternative approach for generating contrast that is sensitive to magnetically labeled cells was developed and demonstrated under in vitro conditions. Attention was paid to



attempts that aim to quantify the number of labeled cells and to improve the sensitivity as well as the specificity to detect these cells.

## Thesis' structure

The principle of Nuclear Magnetic Resonance and the physical basics of signal formation in magnetically inhomogeneous systems, including tissues partly consisting of magnetically labeled cells, are described in the following chapter (Chapter 2).

Chapter 3 is concerned with the measurement of the longitudinal ( $T_1$ ) and the transverse relaxation time constants ( $T_2$ ,  $T_2^*$ ) of solutions of extracellular paramagnetic gadolinium based contrast agents and suspensions of cells labeled with intracellular superparamagnetic iron oxide nanoparticles.

Based on magnetostatics, the magnetic field distortions in homogeneous external magnetic fields can be calculated for specimen and tissues with a well-defined spatial distribution of magnetic susceptibility. A numerical model to compute magnetic field inhomogeneity effects in presence of magnetically labeled cells is presented in Chapter 4. Various geometries including the intra- and the extracellular iron particle distribution, different spatial distributions of labeled cells as well as the effect of cell division of iron loaded cells on the resonance frequency distribution and the static signal decay are studied.

The emphases of Chapter 5 are macroscopic field inhomogeneities due to aggregations of labeled cells. Results from simulations and in vitro MR measurements are presented and the effects on spatial accuracy, sensitivity and quantification of labeled cells are pointed out.

In Chapter 6, the magnetic field perturbations close to labeled cells are exploited to selectively visualize cells and aggregations of cells in the MR image by means of a 'positive contrast MR technique' employing frequency selective radiofrequency pulses.

Chapter 7 is devoted to the overall discussion and the conclusions of this work.

## Chapter 2

# Physical basics

### 2.1 Principle of Nuclear Magnetic Resonance

Nuclear Magnetic Resonance (NMR) is concerned with the interaction of atomic nuclei and electromagnetic radiation, with the absorption and emission of electromagnetic radiation being observed when the nuclei are placed in a strong magnetic field.

One of the fundamental postulates in quantum mechanics is that the angular momentum or ‘spin’  $\vec{I}$  of protons ( $^1\text{H}$  isotopes are considered throughout this work) cannot have an arbitrary value: the magnitude of  $\vec{I}$  is quantized. The magnetic moment  $\vec{\mu}$  related to  $\vec{I}$  is

$$\vec{\mu} = \gamma \cdot \vec{I}. \quad (2.1)$$

The magnitude of  $\vec{\mu}$  is

$$\mu = \gamma \cdot \hbar \cdot \sqrt{I \cdot (I+1)}. \quad (2.2)$$

For  $^1\text{H}$  the ‘gyromagnetic ratio’ is  $\gamma = 42.58 \text{ MHz/T}$ , the spin quantum number is  $I = \frac{1}{2}$ , and  $\hbar$  is Planck’s constant ( $\hbar = h/2\pi = 1.054572 \cdot 10^{-34} \text{ Js}$ ).

In contrast to a given magnetic moment, the magnitude of the macroscopic magnetization (i.e., the average magnetic dipole moment density) is not fixed, since it is the vector sum of many proton spins.

$$\vec{M} = \frac{1}{V} \cdot \sum_{n=1}^N \vec{\mu}_n \quad (2.3)$$

The set of spins  $N$  in volume  $V$  is referred to as a ‘spin ensemble’. In absence of a strong magnetic field, due to thermal fluctuations, the direction of each magnetic moment within this spin ensemble is distributed arbitrarily. Under these circumstances there is no macroscopic magnetization around an object that can be attributed to nuclear paramagnetism.

Applying a strong magnetic field with magnetic induction vector  $\vec{B}_0 = B_0 \cdot \vec{e}_z$  causes Zeeman splitting of the energy levels of the spin  $\frac{1}{2}$  system. Under this condition, the essential characteristic of the quantum system is that the magnetic moment of Zeeman eigenstates is confined to a discrete set of orientations determined by the magnetic quantum number  $m$  (Fig. 2.1). Permitted orientations of the magnetic moment correspond to well-defined energy levels  $E$ .

$$E = -m \cdot \gamma \cdot \hbar \cdot B_0 = -\mu_z \cdot B_0 \quad (2.4)$$

$$m = -I, -I + 1, \dots, I$$

For a spin  $\frac{1}{2}$  system two different energy levels are permitted according to quantum mechanics. Between these energy levels an oscillating magnetic field  $\vec{B}_{rf}$  may induce coherent dipole transitions with frequency

$$\omega_0 = \gamma \cdot B_0 \quad (2.5)$$

The resonance frequency  $\nu_0$  is referred to as the ‘Larmor frequency’. This is the frequency a magnetization vector precesses about the axis of the static magnetic field  $\vec{B}_0$ . In thermal equilibrium, the number of spins  $n(E_i)$  in a certain energy level  $E_i$  is given according Boltzmann to

$$n(E_i) = \frac{N}{\sum_{E_i} \exp\left\{-\frac{E_i}{k_B \cdot T}\right\}} \cdot \exp\left\{-\frac{E_i}{k_B \cdot T}\right\}. \quad (2.6)$$

At room temperature and for an external magnetic field with magnetic induction  $B_0 = 1.5$  Tesla the energy  $E_i$  is  $E_i \ll k_B \cdot T$ , and the macroscopic magnetization along the vector of the  $\vec{B}_0$  field obeys Curie's law.

$$\vec{M}_0 = \frac{\gamma^2 \cdot \hbar^2 \cdot N \cdot I \cdot (I+1)}{3 \cdot k_B \cdot T} \cdot \vec{B}_0 \quad (2.7)$$

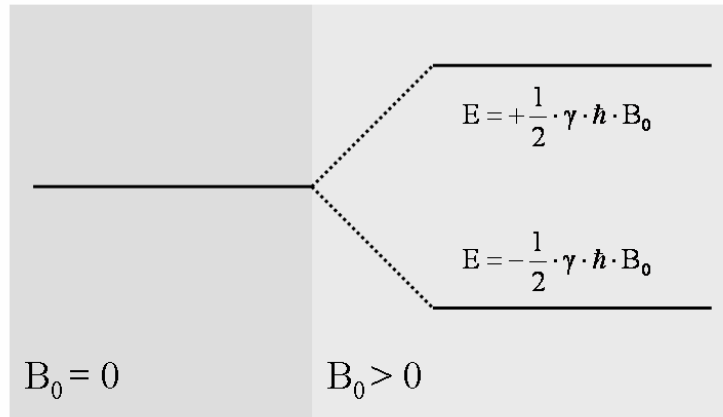


**Figure 2.1** Zeeman splitting of the energy levels for a spin  $1/2$  system in presence of a magnetic field with magnetic induction  $B_0$ .

## 2.2 Bloch equations and relaxation

Quantum mechanics allow for probability predictions about the behavior of isolated nuclear spins due to oscillating electromagnetic fields. According to the Ehrenfest-Theorem an appropriate large spin ensemble can be treated by means of classical physics. In presence of a magnetic field  $\vec{B}_0$  the magnetization vector  $\vec{M}$  of the spin ensemble senses a torque, and the equation of motion of the magnetization vector for non-interacting spins in the spin ensemble without relaxation terms is

$$\frac{d}{dt}\vec{M} = \gamma \cdot \vec{M} \times \vec{B}. \quad (2.8)$$

In the NMR experiment an oscillating magnetic field  $\vec{B}_{rf}$  is superposed perpendicularly to the static magnetic field  $\vec{B}_0$ . Due to this electromagnetic field a rotational force rotates the magnetization vector  $\vec{M}$  about an angle  $\alpha$  with respect to  $\vec{B}_0$ , providing the resonance condition  $\nu_{rf} \approx \nu_0$  is satisfied.

It is most advantageous to analyze the magnetization, and its differential equation, in terms of parallel and perpendicular components defined relative to the static main magnetic field  $\vec{B}_0 = B_0 \cdot \vec{e}_z$ . The parallel or ‘longitudinal’ component of the magnetization is  $M_z$ . The perpendicular or ‘transverse’ components are

$$\vec{M}_{xy} = M_x \cdot \vec{e}_x + M_y \cdot \vec{e}_y. \quad (2.9)$$

Breaking the radiofrequency irradiation at time  $t = 0$ , the components of  $\vec{M}$  parallel and perpendicular to the  $\vec{B}_0$  field ‘relax’ differently in the approach to their equilibrium values. Since the protons are considered to be in thermal contact with the lattice of nearby atoms and molecules, a spin can exchange a quantum of energy with the lattice. Although the transverse components can be ignored in discussing the energy, it follows that, as the longitudinal magnetization returns to its equilibrium value  $M_0$ , the transverse magnetization must vanish. Usually, the transverse magnetization vanishes more quickly due to dephasing of the magnetic moments, because variations in the local fields lead to different local precession frequencies and to the loss of phase coherence between the spins of the spin ensemble.

The magnetization  $\vec{M}(t)$  in presence of a magnetic field and with relaxation terms can be combined into one vector equation,

$$\frac{d\vec{M}}{dt} = \gamma \cdot \vec{M} \times \vec{B} + R_1 \cdot (M_0 - M_z) \cdot \vec{e}_z - R_2 \cdot \vec{M}_{xy}. \quad (2.10)$$

This empirical vector equation is referred to as the ‘Bloch equation’. In a rotating frame and in absence of radiofrequency pulses the complete set of solutions is

$$M_{xy}(t) = M_{xy}(0) \cdot \exp\{-R_2 \cdot t\} \quad (2.11a)$$

$$M_z(t) = M_z(0) \cdot \exp\{-R_1 \cdot t\} + M_0 \cdot (1 - \exp\{-R_1 \cdot t\}) \quad (2.11b)$$

As displayed in Fig. 2.2, the equilibrium or steady-state solution can be found from the asymptotic limit  $t \rightarrow \infty$  of (2.11).

$$M_x(\infty) = M_y(\infty) = 0 \quad (2.12)$$

$$M_z(\infty) = M_0$$

The relaxation rate  $R_1$  characterizes so called ‘spin-lattice-relaxation’ (longitudinal relaxation), and the relaxation rate  $R_2$  accounts for ‘spin-spin-relaxation’ (transverse relaxation).

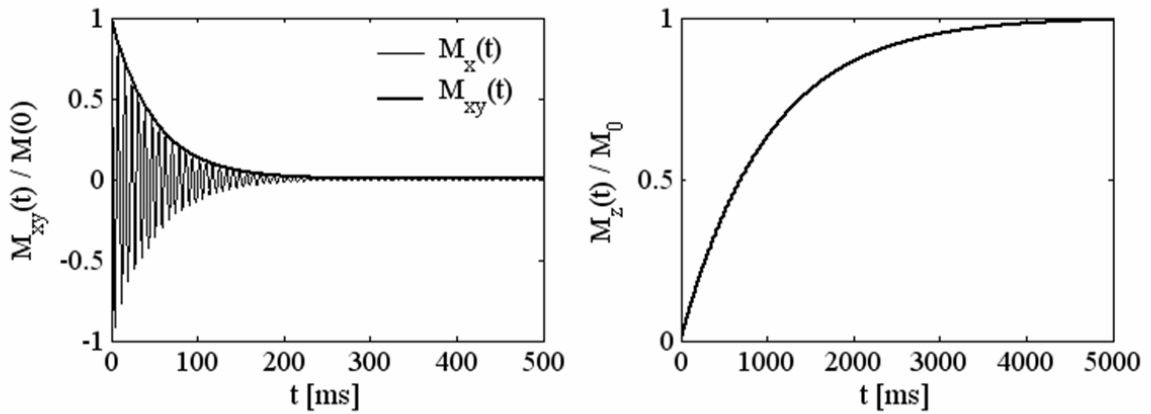


**Figure 2.2** Evolution of the transverse ( $M_{xy}$ ) and the longitudinal ( $M_z$ ) magnetization components after applying a  $\pi/2_x$  pulse.  $B_0 = 1.5$  T,  $T_1 = 1,000$  ms,  $T_2 = 50$  ms

## 2.3 Magnetic susceptibility and magnetic field inhomogeneities

### 2.3.1 Magnetic susceptibility

All magnetic fields can be characterized by the magnetic induction  $\vec{B}$  and the magnetic field strength  $\vec{H}$ . The field  $\vec{H}$  is a convenient vector quantity which would be identical (within a constant universal factor  $\mu_0$ ) to the field  $\vec{B}$  if there is no material present. In the presence of matter, however, these fields must be distinguished rigorously. Within a system with magnetic susceptibility  $\chi$  and permeability  $\mu_r$ ,

$$\vec{B} = \mu_0 \cdot (\vec{H} + \vec{M}_m) = \mu_0 \cdot (1 + \chi) \cdot \vec{H} = \mu_0 \cdot \mu_r \cdot \vec{H}. \quad (2.13)$$

Thus, knowing the magnetic susceptibility of a material is equivalent to knowing its relative permeability and the two quantities are redundant.

The magnetic properties of any sample are determined by the inherent spatial composition of subunits with well-defined values of magnetic susceptibility  $\chi$ . The magnetic susceptibility is a quantitative measure for the magnetization  $\vec{M}_m$  of the sample due to the external magnetic field and reflects a material's tendency to interact with and distort an applied magnetic field. The magnetic susceptibility is negative ( $\chi < 0$ ), positive ( $\chi > 0$ ), or zero ( $\chi \approx 0$ ) for diamagnetic, paramagnetic, or non-magnetic materials, respectively. The largest susceptibility values ( $\chi \gg 1$ ) occur in materials which have unpaired electron spins on some or all of their atoms. Some common, naturally occurring minerals such as magnetite or lodestone ( $\text{Fe}_3\text{O}_4$ ) and hematite ( $\text{Fe}_2\text{O}_3$ ) can maintain permanent magnetic domains even over geological time spans. Certain materials including iron, cobalt, and nickel have permanent domains of electron spin magnetic moments which conspire to produce very strong macroscopic fields existing independently of an external magnetic field ('remanent magnetization'), providing the temperature is not too high (the critical or Curie temperature  $T_c$  for iron, for example, is  $T_c = 744$  °C, for cobalt  $T_c = 1131$  °C, and for nickel  $T_c = 372$  °C [Mes06]).

The term ‘ferromagnetism’ is used as a generic term for an ordered phase of electron spins. However, many distinct spin patterns occur in nature and it is convenient to distinguish those using specific terms: for example ‘ferromagnetism’ (e.g., iron, cobalt, nickel), ‘antiferromagnetism’ (e.g., chromium), or ‘ferrimagnetism’ (e.g., magnetite). The alignment of the magnetic domains is referred to as ‘magnetization saturation’ when it involves essentially all magnetic domains, producing the maximum magnetic moment density. In some cases, particularly in strong fields,  $\vec{M}_m$  does not vary linearly with  $B_0$ , and higher order susceptibility coefficients corresponding to terms in the magnetization proportional to quadratic, cubic and higher powers of  $B_0$  are required.

Subdividing ferromagnetic material leads to particles that are each just one magnetic domain behaving like a set of very large magnetic moments, producing ‘superparamagnetism’ [Wang01]. The magnetic susceptibility of a heterogeneous material containing small, single domain magnetic particles dispersed in a non-ferromagnetic matrix (e.g., water, blood) differs markedly from that of the bulk material. In absence of an external magnetic field, due to thermal motion, such magnetic domains are free to rotate and are randomly oriented, which leads to vanishing magnetization.

Thus, superparamagnetic suspensions lack remanent magnetization without an external magnetic field. In MRI, superparamagnetic particles create intense local fields and ferric oxide or iron particles are used as a contrast agent to produce signal loss in regions where they are deposited [Dal03]. However, depending on the particle’s size (hydrodynamic diameter) and the temperature of the surrounding matrix, the magnetic moments of superparamagnetic particles become completely oriented at relatively low field strengths, because of the large magnetic moment per particle.

The parameters ‘magnetic susceptibility’ and ‘magnetization’ determine, from a magnetic standpoint, the suitability of a material for use in or near an MR imaging system. Bulk samples of hard (large remanent magnetization) and soft (large magnetic susceptibility) materials experience strong magnetic forces in presence of intense magnetic field gradients, and should be excluded from the vicinity of MRI systems for safety reasons [Shel06].



**Table 2.1** Magnetic susceptibilities of selected magnetic materials. The values were taken from [Sch96]. The susceptibility spectrum extends from  $\chi = -1$  for superconductors to  $\chi > 100,000$  for soft ferromagnetic materials. In the absence of pathological iron deposition, the magnetic susceptibilities of the various human soft tissues are estimated to be within  $\pm 20\%$  of  $\chi_{\text{water}}$ .

material	density [ $10^{-3}$ kg/m <sup>3</sup> ]	atomic or molecular weight	magnetic susceptibility
superconductors			-1
water (37 °C)	0.933	18.015	$-9.05 \times 10^{-6}$
human tissues	~1.00 – 1.05		$\sim(-11.0 \text{ to } -7.0) \times 10^{-6}$
hemoglobin molecule (deoxygenated)	1.335	64,650	$0.15 \times 10^{-6}$
air	0.00129	28.97	$0.36 \times 10^{-6}$
ferritin molecule	1.494	929,850	$520 \times 10^{-6}$
$\alpha$ -Fe <sub>2</sub> O <sub>3</sub> (hematite)	5.277	159.70	$1,460 \times 10^{-6}$
Fe <sub>3</sub> O <sub>4</sub> (magnetite)	5.18	231.54	70
cobalt	8.9	58.93	250
nickel	8.9	58.69	600
stainless steel (magnetic)	8.0		400-1,100
iron	7.874	55.847	200,000
supermalloy (16% Fe, 5% Mo, 79% Ni)	8.77		1,000,000

The magnetic susceptibilities of materials vary over several orders of magnitude. A susceptibility spectrum, including magnetic susceptibility characteristics of biological entities relevant for MRI, is given in Table 2.1. Objects such as the human body are composed of various subunits with different values of magnetic susceptibility. Since human tissues contain 65-99 % water, the susceptibility of most of human tissues is close to that of water, which is  $\chi = -9.05 \times 10^{-6}$  at 37 °C [Sch96]. Since susceptibility measurements on tissue specimens are difficult, because of the heterogeneous tissue structure, many susceptibility studies have been conducted in tissue extracts and biochemical components such as lipids, hemoglobin and ferritin [Paul36, Sch96].

However, paramagnetic or ferromagnetic structures or entities within the body cause susceptibility gradients and uttermost complex patterns of magnetic field distribution. A single paramagnetic molecule (e.g.,  $O_2$ ) or ion (e.g.,  $Fe^{2+}$ ,  $Fe^{3+}$ ) can cancel the diamagnetism of thousands of water molecules [Sch96]. Iron is about 30 times more abundant in the human body than all the other paramagnetic ions combined. Thus, the paramagnetic component of the magnetic susceptibility of human tissues is generally determined by the tissue iron concentration which is essentially entirely concentrated in certain tissues: in the blood as hemoglobin, the red bone marrow, the liver, the spleen, and the basal ganglia of the brain.

### 2.3.2 Magnetic field inhomogeneities

During MRI examinations the specimen are positioned within a static magnetic field with high magnitude of magnetic induction  $B_0$ . Advanced superconductive coils and a secondary compensating magnetic field generated by so called ‘shim coils’ allow for high spatial and temporal homogeneity of the static magnetic field in appropriately small measurement volumes. However, any sample under investigation cause magnetic field inhomogeneities. In MRI these field inhomogeneities manifest themselves as signal changes in both magnitude and phase images.

There are numerous sources of magnetic field variation in the body. Some are problematic such as those caused by internal susceptibility differences between tissues (e.g., tissue-air interfaces in the lung). These can cause image distortions and MR signal loss, especially in gradient echo imaging [Lüd85, Rei97]. On the other hand, local or temporal variations in magnetic susceptibility refer to special properties or states of the body, including the oxygenation level of red blood cells [Bel91], iron deposits (ferritin) in the liver [Jen02], and bone structure evaluation relying on the susceptibility difference between bone and marrow [Ford93].

Furthermore, high susceptibility materials can affect tissue water and several potential contrast agents have been proposed and developed for MRI. These include paramagnetic or superparamagnetic contrast media such as gadolinium chelates or suspensions of iron oxide nanoparticles [Bul04]. Microscopic air bubbles, as used for ultrasound image contrast enhancement, have also been proposed as potential MR agents because they differ in their susceptibility relative to tissue or blood [Alex96].

It is most convenient to categorize the relative scale of magnetic field inhomogeneity compared with the MR imaging voxel into macroscopic and microscopic inhomogeneities. The ‘macroscopic scale’ refers to magnetic field gradients over distances that are larger than the imaging voxel. These arise from magnet imperfections, tissue-air interfaces in the body, or high concentrations of paramagnetic material (e.g., after contrast media administration). ‘Microscopic field inhomogeneities’ refer to changes in the magnetic field over distances that are comparable to molecular and cellular size, that is, over distances smaller than the voxel size.

Magnetic field inhomogeneities and relaxation mechanism affect the MRI signal. Fluctuating fields on the atomic and the molecular scale lead to irreversible signal dephasing ( $R_2$  relaxation) and also longitudinal magnetization changes ( $R_1$  relaxation). In practice, there is an additional dephasing of the magnetization introduced by microscopic and macroscopic magnetic field inhomogeneities. In that case, the reduction in the magnetization vector  $\vec{M}_{xy}$  can be characterized by a separate relaxation rate  $R_2^*$  (apparent transverse relaxation) in gradient echo experiments.

## 2.4 Diffusion regimes

In addition to the intensity of microscopic magnetic field inhomogeneities, the diffusion of nuclear spins within magnetic field gradients affects the MRI signal. Diffusion of water molecules through microscopic inhomogeneous magnetic fields can rival and even dominate the intrinsic irreversible signal dephasing. Whereas spin echo sequences can correct the static dephasing due to the variations in the magnetic field experienced by different molecules at different positions, the change in position of a given molecule, because of diffusion, cause more complex signal dephasing effects in MRI.

It can be shown that signal dephasing effects are dependent on both the intensity of the field inhomogeneities within tissue and the strength of spin diffusion [Yab94]. The following paragraph deals with the additional term in the Bloch equation required for the consideration of spin diffusion. In the second paragraph, Brownian motion models (‘diffusion regimes’) are analyzed for the transverse relaxation effects due to both the microscopic fluctuations in the local magnetic field experienced by a nuclear spin and in the spatial position of the spin due to diffusion effects.

### 2.4.1 Bloch – Torrey equation

Brownian motion of the spin magnetic moment arises from the random transport of the proton from one region to another. In magnetically inhomogeneous tissues or in external magnetic field gradients, the magnetic field may have slightly changed in that region. The diffusing spin undergoes random walk fluctuations in its position and, hence, in its phase, due to the rapid changes in the magnetic field it experiences. In the rotating frame the Bloch equation (2.8) must be expanded by an additional diffusion term.

$$\frac{d\vec{M}}{dt} = \gamma \cdot \vec{M} \times \vec{B} + D \cdot \Delta \vec{M} \tag{2.14}$$

$$\Delta = \frac{\partial^2}{\partial x^2} + \frac{\partial^2}{\partial y^2} + \frac{\partial^2}{\partial z^2}$$

Note that relaxation terms have been neglected in (2.14). In order to solve this partial differential equation, it is convenient to assume macroscopic linear field gradients. This allows for the treatment of diffusion sensitive field gradients in ‘diffusion weighted MRI’. In isotropic media the diffusion coefficient  $D$  is a scalar. Otherwise, due to tissue boundaries, the diffusion may be anisotropic and  $D$  is a tensor [Enn06].

### 2.4.2 Characterization of diffusion regimes

In tissue, the actual field distribution is generally unknown and the signal dephasing effects due to diffusion of spins through microscopically inhomogeneous magnetic fields rely on statistical approaches [Yung03]. It is convenient to treat the heterogeneous medium as a system composed of randomly distributed stationary magnetic objects such as magnetic spheres surrounded by proton spins undergoing unrestricted, isotropic diffusion motion (Fig. 2.3). The restriction to spherical geometries is no major limitation since it characterizes several magnetic objects including paramagnetic/superparamagnetic particles, magnetically labeled cells, and red blood cells. Within these models only signal dephasing caused by magnetic field inhomogeneity and diffusion effects within the effective range of the dipole field is considered, whereas the dipole-dipole interaction among the spins is generally neglected. In the literature

the analytical predictions of those models agree quite well with simulation and experiments, implying that the model comprises the dominant physical processes [Ken94, Yab94, Yung03].

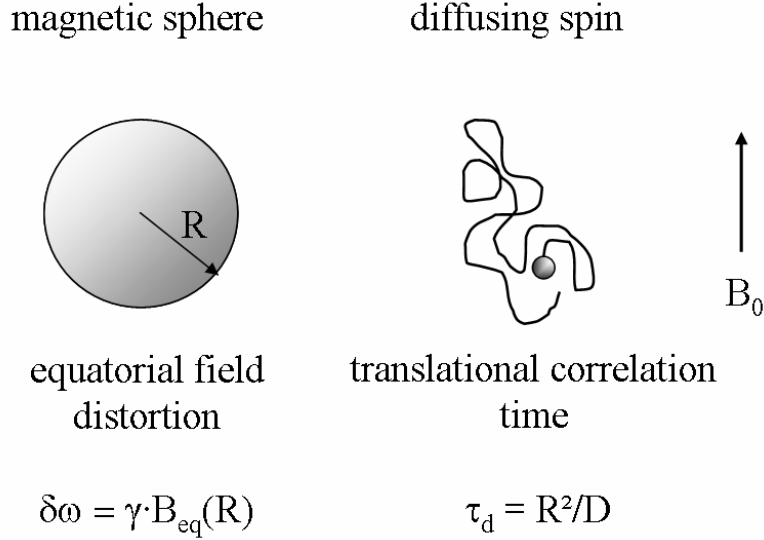


**Figure 2.3** Sketch of the ‘diffusing spin’ – ‘magnetic sphere’ system. Based on the relative magnitudes of the magnetic field distortion and the spin diffusion relative to the sphere, it is convenient to categorize the system’s relaxation behavior into so-called ‘diffusion regimes’.

The relaxation behavior of the spin-sphere system can be categorized in so-called ‘diffusion regimes’, which are determined by the magnetic, geometric and dynamic properties of the system. These are classified based on the relative magnitudes of two competing relaxation mechanism: the dynamic frequency scale and the magnetic frequency scale [Ken94]. The dynamic frequency scale is the inverse of the translational diffusion correlation time

$$\tau_d = R^2/D, \tag{2.15}$$

where  $R$  is the radius of the microscopic magnetic sphere and  $D$  is the translational diffusion coefficient of the spins relative to the stationary spheres. The magnetic frequency scale accounts for the variation in the Larmor frequency at the equator surface due to the field perturbation caused by the sphere, as sensed by nearby spins. It is defined as the equatorial field  $\delta B_{\text{eq}}(R)$  evaluated on the surface of the particle in frequency units, to read

$$\delta\omega = \gamma \cdot \delta B_{\text{eq}}(R). \tag{2.16}$$

## Outersphere regime and fast diffusion regime

In the ‘outersphere regime’ ( $\delta\omega \ll 1/\tau_d$ ) [Gill87] the relaxation effect due to spin diffusion exceeds the relaxation effect due to magnetic field variation. Thus, the motion of spins averages out the effects of individual perturbers such as metallic complexes or free radicals with a few nanometers. In the ‘fast diffusion regime’ ( $\delta\omega < 1/\tau_d$ ) [Weis94], for slightly larger perturbers, the solvent spins appear to move slower than in the outersphere regime. However, since the motion is fast enough it is expected that the relaxation is still dominated by the  $1/\tau_d$  mechanism. In both the outersphere and the fast diffusion regime, the gradient echo  $R_2^*$  relaxation rate is expected to be about the same as the spin echo  $R_2$  relaxation rate.

$$R_2 \approx R_2^* = k \cdot f \cdot (\delta\omega)^2 \cdot \frac{R^2}{D} \quad (2.17)$$

Here  $f$  is the volume fraction of spherical perturbers in the medium and  $k$  is the proportionality constant, which is  $k = 16/235$  for the outersphere regime [Gill87]. For the fast diffusion regime it is anticipated that  $k > 16/235$  since motional averaging is less effective.

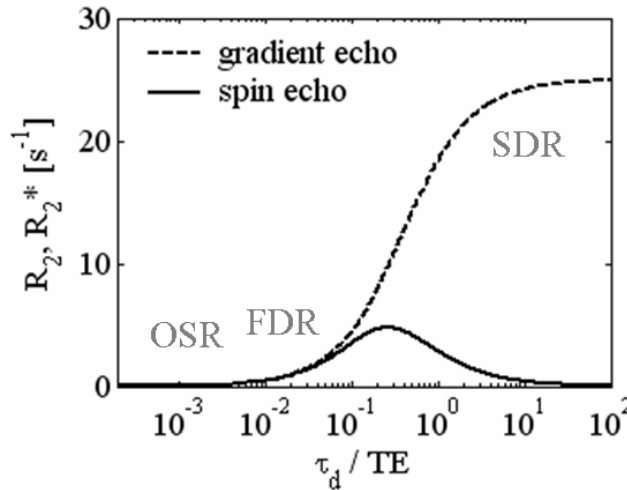


**Figure 2.4** Dephasing of the transverse magnetization vector due to the diffusion of spins in inhomogeneous magnetic fields. The enhancement in spin echo ( $R_2$ ) and gradient echo ( $R_2^*$ ) relaxation versus diffusion correlation time  $\tau_d$  is displayed. The relaxation rates were calculated according to Anderson and Weiss [And53] and Kennan et al. [Ken94]. Mean square frequency fluctuation  $\langle \omega_0^2 \rangle = 1,000(\text{rad/s})^2$ ,  $TE = 50$  ms. Outersphere regime (OSR), fast diffusion regime (FDR), slow diffusion and static dephasing regime (SDR).

## Slow diffusion regime and static dephasing regime

In the situation when  $\delta\omega > 1/\tau_d$  ('slow diffusion regime'), the spins appear to move very slowly, so that the diffusive effect is minimal and the relaxation mainly comes from the loss of phase coherence due to magnetic field inhomogeneities. This occurs when the perturber size is relatively large and the magnetic field distortion is relatively strong. For the spin echo case in the slow diffusion regime [Yung03],

$$R_2 = f \cdot \frac{\sqrt{D}}{R}. \quad (2.18)$$

In the gradient echo case the  $R_2^*$  relaxation is expected to be in similar function to that of the static dephasing regime.

In case of large magnetic objects and intense magnetic field gradients, the spins move very slowly and appear to be stationary, so that diffusion has practically no effects on signal dephasing. As described by Yablonskiy and Haacke [Yab94] the system is in the 'static dephasing regime' ( $\delta\omega \gg 1/\tau_d$ ) in that case. For the spin echo experiment the magnetic field inhomogeneity effects are completely recovered by the formation of the spin echo, because the loss of phase coherence is entirely restored due to the  $180^\circ$  refocusing pulse, yielding  $R_2 = 0$ . On the other hand, in the gradient echo case this loss of phase coherence is not recovered due to the lack of refocusing pulses, yielding maximum  $R_2^*$  relaxation [Bro61]

$$R_2^* = \frac{2\pi}{3\sqrt{3}} \cdot f \cdot \delta\omega. \quad (2.19)$$

## Intermediate regime

In the region of compromise where the competing relaxation mechanisms of  $1/\tau_d$  and of  $\delta\omega$  are equally effective, the system is in the 'intermediate regime'. The coherent analytic understanding of signal dephasing is lacking in that case, and the problem is usually treated by Monte Carlo simulations [Har89, Ken94, Wei94]. Moreover, it is generally unknown before-

hand in which particular diffusion regime one system might fall, making interpreting either simulation or experimental data difficult.

A limited number of approaches focus on the whole dynamic range. Assuming a Gaussian probability distribution of the phase angle over time, Anderson and Weiss [And53] developed the ‘mean field theory’, in which diffusion leads to modulations in the local fields experienced by the protons (Fig. 2.4). This theory was introduced in MRI by Kennan et al. [Ken94] and Sukstanskii and Yablonskiy [Suk03].

When  $\tau_d$  is short compared to TE there is little difference between the gradient echo and spin echo signal decay rates. However as  $\tau_d$  is increased the spin echo relaxation reaches a maximum, and then begins to decrease as refocusing becomes more effective. In contrast, the gradient echo relaxation approaches the static limit. Another approach approximates the diffusion dynamics by stochastic transition dynamics (‘strong collision approximation’) [Zie05a].

## 2.5 MR signal formation in the static dephasing regime

Simulations indicated that for magnetic objects above some critical size, diffusion effects quickly become less important. In those cases signal dephasing and relaxation is dominated by the magnetic field inhomogeneity effects. Several models have been developed in conjunction with MR imaging to investigate the static dephasing regime under the influence of different sources of static field inhomogeneities including line broadening in lung tissue [Case87], contrast agent studies [Pint06a], magnetically labeled cells [Pint06c], bone marrow [Ford93, Sch96], and blood vessel networks [Ken94].

In the last paragraph, it was pointed out that motion averaging plays an important role for small magnetic objects. Apparently the outersphere theory is not valid for the larger ferromagnetic particles due to their relatively strong fields over fairly large distances, implying that the field superposition effects of neighboring magnetic centers must be accounted for. In fact, in microscopic MR images of magnetite particles (average size 3.5  $\mu\text{m}$ ) Lauterbur et al. [Lau86] observed the characteristic dipole field indicating that the criterion of motion averaging fails. This dipole pattern was also observed for cells labeled with superparamagnetic iron oxide (SPIO) nanoparticles [Pint05b]. Thus, for magnetically labeled cells considered in this



work, signal dephasing is dominated by their magnetic field inhomogeneity effects and for aggregations of labeled cells it is reasonable to neglect spin diffusion effects.

The most pronounced susceptibility induced effect is due to static line broadening in a gradient echo experiment when  $\delta\omega \cdot \tau_d \gg 1$  ('static dephasing regime'). In general, the signal obtained from within a voxel at echo time TE is

$$S(\text{TE}) = S_0 \cdot \langle \exp\{-i \cdot \Phi_j\} \rangle_{\text{TE}} = S_0 \cdot \langle \exp\{-i \cdot \gamma \cdot B_{\text{int}} \cdot \text{TE}\} \rangle. \quad (2.20a)$$

$$S(\text{TE}) = S_0 \cdot \int_{-\infty}^{\infty} p(B_{\text{int}}) \cdot \exp\{-i \cdot \gamma \cdot B_{\text{int}} \cdot \text{TE}\} dB_{\text{int}} \quad (2.20b)$$

The brackets in (2.20a) denote the spatial average over the entire voxel and  $B_{\text{int}}$  denotes the microscopic field generated by the heterogeneous susceptibility variation. The phase shifts due to spin precession in  $B_{\text{int}}$  for time TE are denoted  $\phi_j$ . In practice the precise microscopic field distribution  $p(B_{\text{int}})$  is in general unknown. However, for statistical reasons it is convenient to consider Gaussian or Lorentzian field distributions (Fig. 2.5).

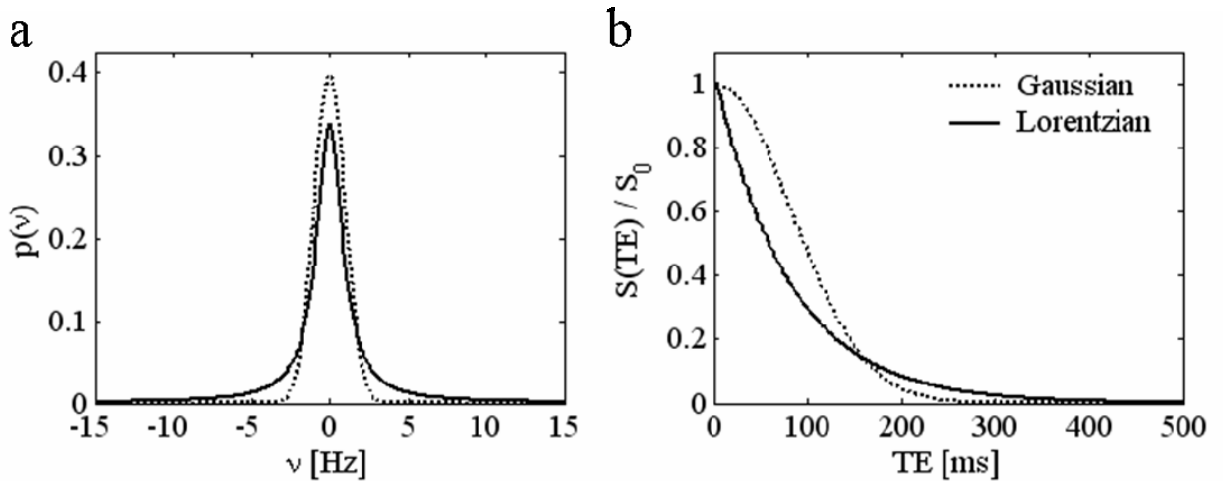


**Figure 2.5** contrasts the static signal decay resulting from Gaussian and Lorentzian frequency distributions with unit variance.

If the magnetic field distribution within a voxel is random with a ‘Gaussian’ distribution

$$p(\mathbf{B}_{\text{int}})_{\text{Gauss}} = \frac{1}{\sqrt{2\pi \cdot \sigma_B^2}} \cdot \exp\left\{-\frac{\mathbf{B}_{\text{int}}^2}{2 \cdot \sigma_B^2}\right\} \quad (2.21)$$

than the average in equation (2.20) can be evaluated over all values of  $\mathbf{B}_{\text{int}}$ .

$$S(\text{TE}) = S_0 \cdot \frac{1}{\sqrt{2\pi \cdot \sigma_B^2}} \int_{-\infty}^{\infty} \exp\{-i \cdot \gamma \cdot \mathbf{B}_{\text{int}} \cdot \text{TE}\} \cdot \exp\left\{-\frac{\mathbf{B}_{\text{int}}^2}{2 \cdot \sigma_B^2}\right\} d\mathbf{B}_{\text{int}} \quad (2.22a)$$

$$S(\text{TE}) = S_0 \cdot \exp\left\{-\frac{\gamma^2 \cdot \sigma_B^2 \cdot \text{TE}^2}{2}\right\} \quad (2.22b)$$

The effective transverse relaxation rate due to static line broadening produced by a Gaussian field distribution with variance  $\sigma_B$  is [Ken94]

$$R_2^* = \frac{\gamma^2 \cdot \text{TE} \cdot \sigma_B^2}{2}. \quad (2.23)$$

If the magnetic field distribution within a voxel is random with a ‘Lorentzian’ distribution

$$p(\mathbf{B}_{\text{int}})_{\text{Lorentz}} = \frac{1}{\pi} \cdot \left[ \frac{\sigma_B}{\sigma_B^2 + \mathbf{B}_{\text{int}}^2} \right] \quad (2.24)$$

the signal at TE for a gradient echo is

$$S(\text{TE}) = S_0 \cdot \frac{\sigma_B}{\pi} \int_{-\infty}^{\infty} \exp\{-i \cdot \gamma \cdot \mathbf{B}_{\text{int}} \cdot \text{TE}\} \cdot \left( \frac{1}{\sigma_B^2 + \mathbf{B}_{\text{int}}^2} \right) d\mathbf{B}_{\text{int}} \quad (2.25a)$$

$$S(\text{TE}) = S_0 \cdot \exp\{-\gamma \cdot \sigma_B \cdot \text{TE}\}. \quad (2.25b)$$

This gives a relaxation rate of [Ken94]

$$R_2^* = \gamma \cdot \sigma_B. \quad (2.26)$$

Only in the limit of no diffusion the signal decay rate will represent the true field distribution  $p(B_{\text{int}})$ . For a distribution of the Gaussian form, the relaxation rate  $R_2^*$  varies linearly with TE, whereas for a distribution of the Lorentzian form,  $R_2^*$  is independent of TE. In absence of diffusion, Lorentzian distributed frequency components within the voxel lead to a monoexponential signal decay, whereas for non-Lorentzian frequency distributions, a non-monoexponential signal decay is observed. Generally, in presence of magnetic field inhomogeneities, the frequency distribution is of a mixed ‘Lorentzian-Gaussian’ type. In that case the precise magnitudes and the relationship of gradient echo and spin echo decay depend on factors such as the intensity and the geometry of the magnetic field inhomogeneities, the field strength, and the echo time.

## Chapter 3

# Relaxivities of intra- and extracellular contrast agents

### 3.1 Physical and biological background

Magnetic field inhomogeneities affect the signal acquired in Magnetic Resonance Imaging. Fluctuating atomic and molecular magnetic fields lead to irreversible signal dephasing ( $R_2$  relaxation) and also to longitudinal magnetization changes ( $R_1$  relaxation). In addition, dephasing of the magnetization may be due to magnetic field inhomogeneities and susceptibility gradients within the sample, particularly in gradient echo imaging (so-called  $R_2^*$  relaxation).

This work seeks to determine the longitudinal and transverse relaxation rates as well as the relaxivities for extracellular gadolinium (Gd) contrast agents and cells labeled with superparamagnetic iron oxide nanoparticles. Various concentrations of Gd contrast agents in human blood plasma were investigated under well-defined experimental conditions (temperature, albumin protein concentration, etc.) at different magnetic field strengths.

Furthermore, magnetically labeled cells were suspended in agar gel. In vitro samples of single labeled cells were prepared successfully employing proper labeling and suspension

techniques. This allowed for the systematic examination of the relaxation and signal dephasing effects due to magnetically labeled cells. Such systematic studies of both Gd contrast media and labeled cells are crucial to establish optimal parameters for MR sequences at each magnetic field strength.

### 3.1.1 Interstitial or extracellular contrast agents

For many diagnostic tasks the inherent soft-tissue contrast is sufficient to distinguish different tissues on MRI without the need for exogenous contrast agent. However, the native contrast between different tissues is not always sufficient to distinguish or characterize pathologic changes unambiguously. In order to enhance the contrast between normal and diseased tissue, and hence to improve the likelihood of detecting tumors or lesions associated with the tissue, MRI benefits from dedicated contrast agents.

Although a number of different types of contrast agents are available today for a variety of MRI applications, by far the most commonly employed agents are based on the paramagnetic properties of gadolinium. These are clear, colorless fluids, formulated with bacteriostatic additives for intravenous administration. The distribution of the agents is the extracellular and interstitial space.

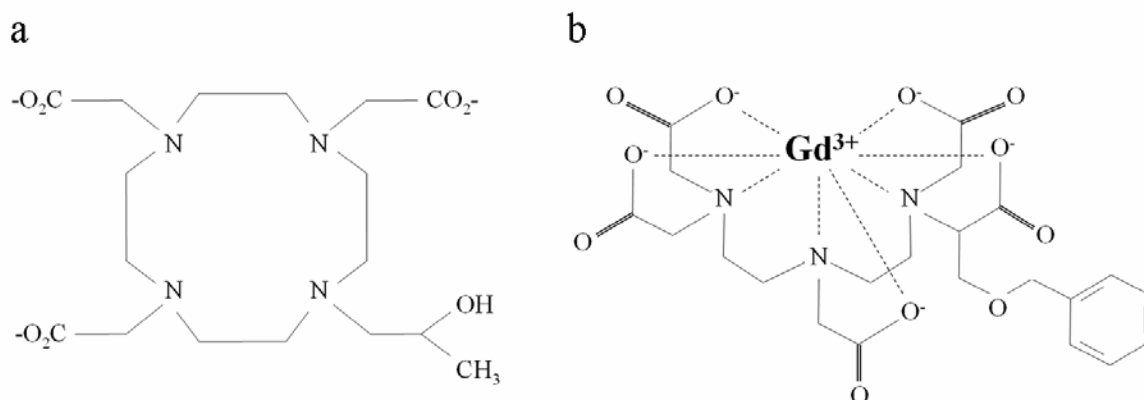


**Figure 3.1** The safety basis of the gadolinium chelates rests with the ability of the chelate to hold extremely tightly the gadolinium ion. The word ‘chelate’ comes from the Greek root ‘chelos’, meaning claw. (a) Cyclic chelates demonstrating higher *in vivo* stability and thus a theoretical safety margin [DeHa99]. (b) Chemical structure of gadobenate dimeglumine.

Gd is a member of the transition elements (atomic number 64) and as such extremely toxic in  $Gd^{3+}$  elemental form. The safety basis of the Gd chelates rests with the ability of the chelate to hold extremely tightly the  $Gd^{3+}$  (Fig. 3.1). This assures an almost complete excretion using renal and hepatobiliary pathways. Although the complex can dissociate into metal ion and ligand in an aqueous solution, the dissociation constant of the complex is in the order of  $10^{-17} - 10^{-27}$ , so that free metal ions cannot appear in concentrations which would induce adverse toxic side effects under in vivo conditions.



**Fig. 3.2** High-resolution whole-body MR image (a), and contrast-enhanced MR angiography (b). (University Hospital Tübingen, Department of Diagnostic Radiology).

Lesion enhancement occurs by disruption of the blood-brain barrier or lesion vascularity. Due to the paramagnetism of the ion, gadolinium contrast agents induce local magnetic field

fluctuations and reductions in the tissue relaxation time constants  $T_1$  and  $T_2$ . In  $T_1$  weighted MR images this is visualized as an increase in signal intensity. In clinical practice, the contrast enhancement due to Gd contrast agents is used for lesion detection and characterization as well as for contrast-enhanced MR angiography (Fig. 3.2).

Gd-DTPA (gadopentetate dimeglumine) was the first to be approved for clinical use in 1988. By slight changes in structure, agents with improved relaxivity and altered distribution have been developed. These gadolinium agents have different molecular structures but similar pharmacokinetic profiles and physicochemical properties (Table 3.1), and, in most cases, few differences can be discerned when these agents are used in routine clinical practice at equivalent dose [Kir03].

**Table 3.1** Physicochemical properties of low-molecular-weight gadolinium-based extracellular MR contrast agents, approved for clinical use in Europe. The values are reported according to the manufacturers [Hup04, DeHa99].

INN code	Gadopentetate dimeglumine	Gadobutrol	Gadobenate dimeglumine	Gadodiamide	Gadoteridol
	Gd-DTPA	Gd-BT-DO3A	Gd-BOPTA	Gd-DTPA-BMA	Gd-HP-DO3A
Trade name	Magnevist	Gadovist	Multihance	Omniscan	Prohance
Manufacturer	Schering AG	Schering AG	Bracco	Amersham Health	Bracco
Molecular weight	938.0	-	1,058.2	573.6	558.7
Concentration [M]	0.5	1.0	0.5	0.5	0.5
Osmolarity [mOsmol/kg H <sub>2</sub> O @ 37 °C]	1,960	1,603	1,970	780	630
Density [g/ml @ 20 °C]	1.21	-	1.22	1.13	1.14
Viscosity [mPA s @ 37 °C]	2.90	4.96	5.30	1.9	1.3

Just two of these agents (Gd-BT-DO3A [gadobutrol] and Gd-BOPTA [gadobenate dimeglumine]) have features that distinguish them from the remaining agents. In the case of Gd-BT-DO3A, the distinguishing feature is that it is commercially available as a 1.0 M formulation rather than as a 0.5 M formulation. Unlike Gd-DTPA and Gd-BT-DO3A, the Gd-BOPTA molecule interacts weakly and transiently with serum albumin resulting in a slowing of the tumbling rate of the Gd complex, which allows for a longer rotational correlation time with inner shell water protons [Ban91] and a more efficient energy exchange with respect to the surroundings. This leads to a significant enhancement of both longitudinal and transverse relaxation compared to the relaxation observed with other gadolinium agents [Cav97, Roh05, Pint06d, Lau06].

The purpose of the present study was to accurately determine the relaxation enhancement of a range of concentrations of Gd-DTPA, Gd-BT-DO3A, and Gd-BOPTA in human blood plasma (37 °C) under identical experimental conditions at 0.2 T, 1.5 T, and 3 T.

### 3.1.2 Intracellular contrast agents - Magnetically labeled cells

Cellular imaging is the ‘non-invasive and repetitive imaging of targeted cells and cellular processes in living organism’ [Bul04]. Over the past decade, the use of MRI for cellular imaging has been subject of extensive research since it provides anatomical, functional, and biochemical information as well as excellent image quality. Furthermore, MRI enables to acquire diagnostic images in arbitrary slice orientation and depth of penetration. The main objective of the current research is to combine these unique features of MRI with the specificity of dedicated contrast agents.

Due to its limited spatial resolution, MRI is in fact not capable of visualizing single cells. However, due to magnetic moments greater than  $10^3$  to those of paramagnetic contrast agents [Bul99], cells labeled with superparamagnetic iron oxide nanoparticles (SPIO) cause intense magnetic field distortions over fairly large distances. Thus, SPIO labeled cells become detectable due to their significant effects on MRI signal dephasing induced in water molecules near the cells. In practice, labeled cells are reflected either as low-intensity signal spots or signal voids, particularly in  $T_2^*$ -weighted gradient echo MRI. The high sensitivity of



MRI to SPIO induced field inhomogeneities even allows for the in vitro [Zha05, Pint06b] and the in vivo [Sha06, Heyn06] detection of single labeled cells.

SPIO agents include a wide range of physico-chemical preparations with the most of them still being in experimental study stages or clinical trials. The particles consist of an iron oxide crystal, which vary in size from agent to agent (their size is generally between 4-10 nm), and a coating material such as dextran or carboxydextran. The hydrodynamic diameter of SPIO particles differs between 20 nm and 300 nm, as stated by the manufacturers [Wang01]. The iron is biocompatible and can be recycled by cells using the normal biochemical pathways for iron metabolism.

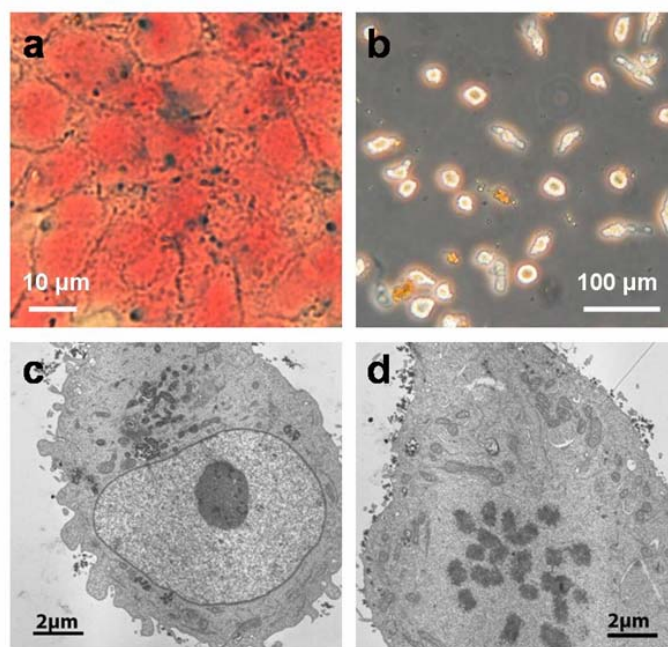


**Figure 3.3** Light microscopic (a, b) and electron microscopic images (c, d) of SK-Mel28 human melanoma cells, labeled by means of incubation with SH U 555A. The incubation time was 24 hours, and the iron concentration was 100 µg Fe / ml. Fig. (a) was acquired before washing the cells. The blue dots indicate the iron oxide label (iron blue staining). After incubation the cells were washed with phosphate-buffered saline in order to separate labeled cells from unbound fractions of iron oxide (b). Electron microscopy (c, d) revealed that the major fraction of iron oxide nanoparticles was taken up in the lysosomes within the cells.

Exploiting the capability of certain cell types to ingest small particles through phagocytosis the in vivo labeling of macrophages has been used for the detection and delineation of focal

liver lesions and to image inflammatory processes such as atherosclerosis. The imaging of macrophage activity is the most significant application of SPIO agents, in particular for tumor staging of the liver [Sta88] and lymph nodes [Wei90]. Following injection, SPIO is rapidly ingested by liver Kupffer cells, which are specialized macrophages, so that normal liver tissue appears hypointense in the image even though the Kupffer cells containing the particles comprise only 2 % of the mass of the liver. In presence of primary liver tumor or liver metastasis, liver tissue lacks of Kupffer cells and the signal intensity remains unaltered and thus contrasts to the surrounding tissue that turns hypointense.

Cell labeling can be also performed by incubating cells with the contrast agent *in vitro*. The labeled cells can be easily detected by light and electron microscopy (Fig. 3.3). The transplantation or transfusion of labeled cells in living organism has led to a growing research interest to monitor cellular dynamics *in vivo* by means of MRI including cell migration and homing [Hoe02].

Whereas most of these studies to date have been mere the ‘proof of principle’, further exploitation of this technique will provide deeper insight into the biodistribution of cells and also at monitoring stem cell based therapies. The reports of first clinical trials using *ex vivo* labeled cells have been published [DeVr05]. As described in the current work, attention should be paid to attempts that aim to quantify the number of labeled cells, and improve the sensitivity as well as the specificity to detect magnetically labeled cells.

In order to establish a reliable calibration standard for the *in vivo* and *ex vivo* quantification of labeled cells, numerous groups investigated the effects of concentration of SPIO labeled cells on the MRI signal decay [Mat05, Dal03, Metz04]. In these studies, concentration effects were analyzed for large cellular aggregations by measuring the observable signal voids in the MR images. Further, a fixed magnetic field strength was used, or the experiments were performed for either spin echo or gradient echo sequences [Sim05, Bow02]. No studies have been performed to accurately quantify the cellular relaxation enhancement of low concentrations of labeled cells on the microscopic scale. Those concentration effects on both spin echo and gradient echo transverse relaxation within the entire range of clinical magnetic field strengths up to 3 T have not been addressed so far.

In the present work, the effect of the concentration of SH U 555A labeled SK-Mel28 human melanoma cells on the cellular transverse relaxivity was systematically studied for both spin echo and gradient echo sequences. Proper labeling and suspension techniques allowed for the examination of homogeneously suspended cells in agar gel phantoms. The experiments were carried out at 0.2 T, 1.5 T, and 3 T using clinical MR whole body scanners.

## 3.2 Measurement of relaxation rates and relaxivities

Relaxation rate measurements in MRI involve the generation of an image, in which each pixel holds the mean signal intensity value given as the complex summation over all nuclear spin magnetic moments confined to the corresponding volume element ('voxel'). If several images are obtained with different sets of sequence parameters, for a specific imaging voxel the mean signal intensity values are weighted related to the local relaxation time constants assigned to that voxel.

The finite volume of the imaging voxel, however, suggests that even those relaxation rate maps, demonstrating the distribution of relaxation rates within the object of interest, can suffer from partial volume effects. These arise when the imaging voxel contains tissue fractions with a range of relaxation rate values so that only a weighted mean value of the relaxation rate is assigned to the imaging voxel. It is anticipated that partial volume effects are negligible in the current work since samples containing homogeneous solutions of extracellular contrast media and homogeneous suspensions of labeled cells were examined.

### 3.2.1 Measurement of the longitudinal relaxation rate $R_1$

Imaging techniques based on 'inversion recovery' and 'variable flip angles' were considered for the measurement of the  $R_1$  dependent MR signal intensity for solutions of extracellular Gd contrast agents.

## Inversion recovery sequence

The inversion recovery sequence begins with a preparatory  $180^\circ$  pulse (Fig. 3.4). This pulse inverts the initial magnetization  $M_0$  within the selected slice, which is then left to relax with the relaxation rate  $R_1$  [Kal93]. In abbreviated form, the sequence is written as

$$180^\circ - \text{TI} - 90^\circ - \frac{\text{TE}}{2} - 180^\circ - \frac{\text{TE}}{2} - \text{SE} \quad (3.1)$$

where TI is the ‘inversion time’ and, due to the second  $180^\circ$  pulse, the acquired signal is a spin echo (SE).

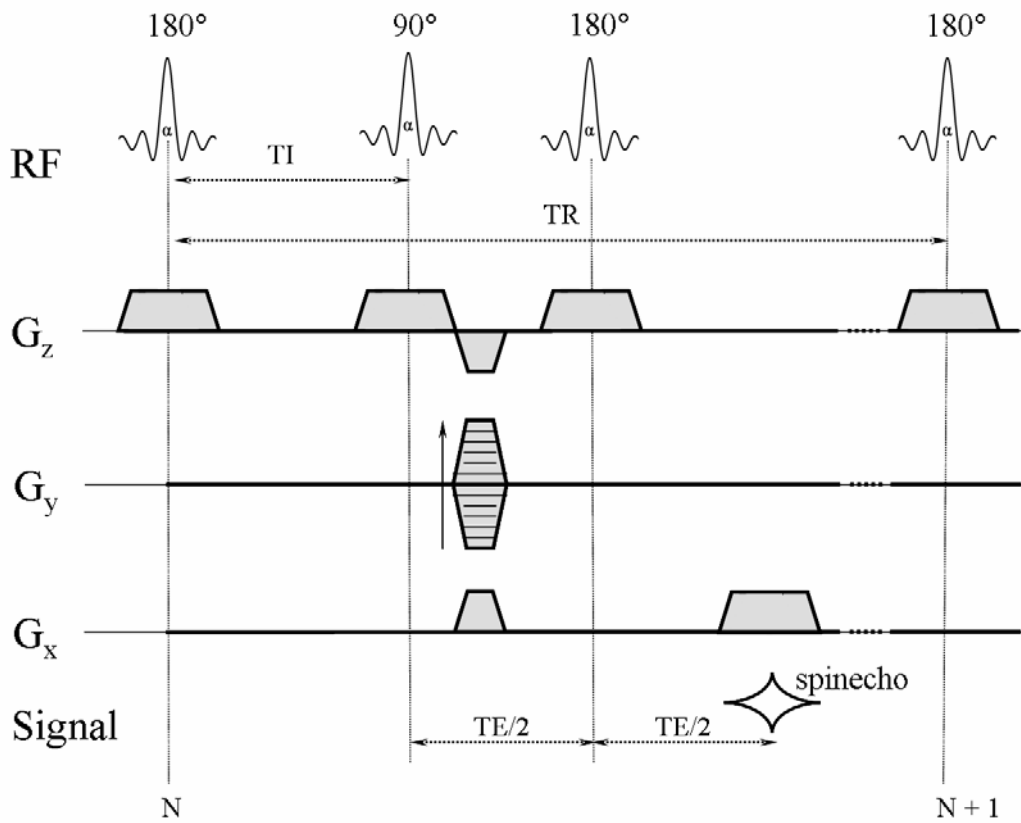


**Figure 3.4** Pulse diagram for a 2d spin echo sequence with inversion recovery preparation. The acquisition of several images with different inversion time TI (while other sequence parameters are kept constant) allows for the calculation of the longitudinal relaxation time constant  $T_1$ .  $G_z$ : slice selective magnetic field gradient,  $G_y$ : phase encoding gradient,  $G_x$ : read out gradient.

The image signal intensity  $S_{IR}$  is proportional to the fraction of the magnetization that has managed to relax during the TI interval.  $S_{IR}$  is a function of the  $R_1$  relaxation rate and the pulse timing parameter TI [Mac87], to read

$$S_{IR}(TI) = A \cdot [1 - k \cdot \exp\{-R_1 \cdot TI\} + \exp\{-R_1 \cdot TR\}]. \quad (3.2)$$

In this equation the parameter A accounts for both the thermal equilibrium magnetization  $M_0$  and the signal decay due to transverse  $R_2$  relaxation within the TE interval. In practice, due to an inaccurate adjustment of the sequence flip angle, the inversion of the magnetization can be insufficient. The parameter k in eq. 3.2 accounts for those deviations from the 180° inversion over the entire imaging slice, for which  $k = 2$ .

In addition, TR must be several times longer (i.e.,  $TR = 5 \times T_1$ ) than the maximal  $T_1$  values ( $T_1 = 1/R_1$ ) of the samples, so that the perturbed magnetization returns to its thermal equilibrium value prior to the next inversion pulse. However, in MRI this requirement is rarely met, since the imaging time would be unacceptable long. In eq. 3.2 the second exponential term  $\exp\{-R_1 \cdot TR\}$  corrects for the partial recovery of the magnetization.

If several images are obtained with different TI (while other sequence parameters are kept constant) the  $R_1$  relaxation rate can be extracted by a non-linear fit of  $S_{IR}(TI)$  against TI.

### Variable flip angle

In this approach, a radiofrequency pulse with variable flip angle  $\alpha$  is applied to perturb the magnetization [Fram87]. After excitation the magnetization is left to partially relax back to its thermal equilibrium value during the short repetition time TR. In dependence on the angle  $\alpha$ , only a fraction of magnetization is ‘flipped’ into the transverse plane. The signal intensity  $S_{vfa}$  is then a function of the flip angle  $\alpha$  and the amount of longitudinal relaxation that has occurred during the TR interval.

$$S_{vfa}(\alpha) = A' \cdot \frac{\sin\alpha \cdot [1 - \exp(-R_1 \cdot TR)]}{1 - \cos\alpha \cdot \exp(-R_1 \cdot TR)} \quad (3.3)$$

In this equation, the parameter  $A'$  accounts for both the thermal equilibrium magnetization  $M_0$  and the decay of the transverse magnetization due to an effective relaxation time constant  $T_2^*$ . The echo signal recorded is a gradient echo. A three-dimensional (3d) approach was applied (Fig. 3.5) because in a two-dimensional sequence the adjusted flip angles are present only in the central partitions inside the excited slab, rather than over the entire slice.

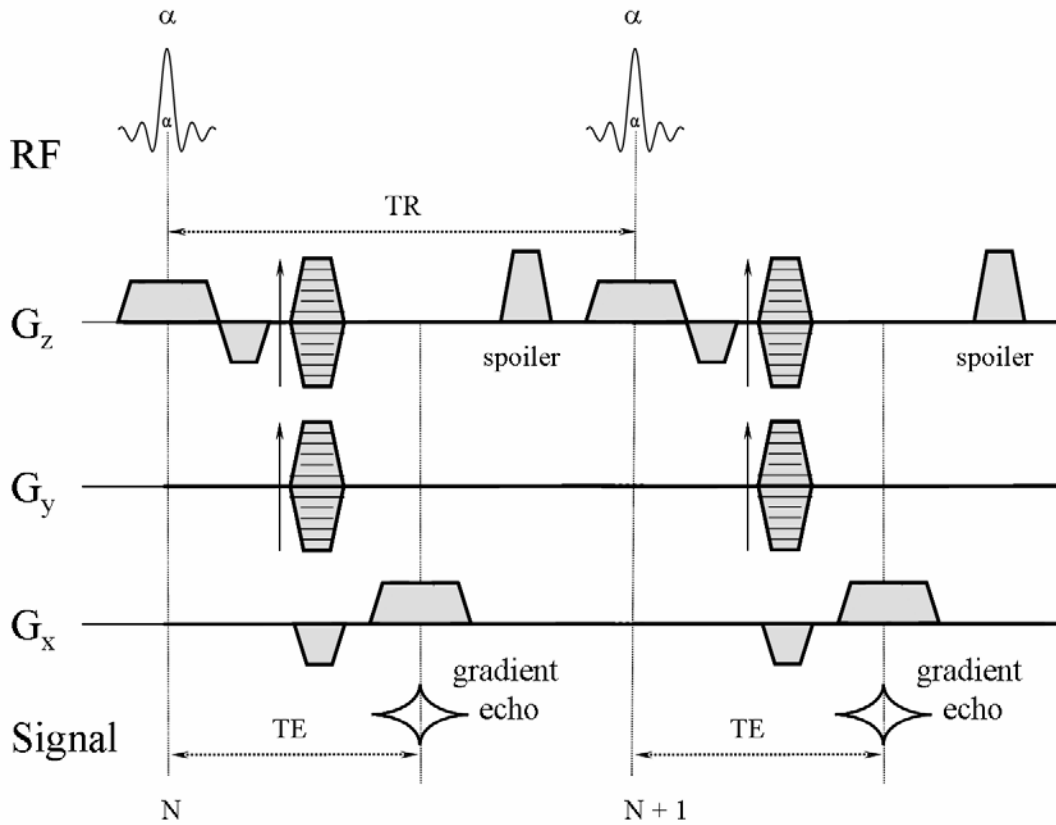


**Figure 3.5** Pulse diagram for a 3d gradient echo sequence. A spoil gradient pulse provides dephasing of the remaining magnetization prior to the next sequence repetition. The generation of a  $T_1$  map requires at least two repetitions of the imaging sequence with different values for the flip angle  $\alpha$  of the excitation pulse, whereas TE is kept constant.

### 3.2.2 Measurement of the transverse relaxation rates $R_2$ and $R_2^*$

Multi echo sequences may be used to obtain weighted data related to  $R_2$  or  $R_2^*$ . An echo signal is formed as a result of the refocusing of a large number of dephased spins and it peaks when the isochromats reach new phase coherence. The acquired echo signal can be generated either by multiple  $180^\circ$  radiofrequency pulses or gradient reversal. Signals of the

former type are termed ‘spin echoes’ and the latter ‘gradient echoes’. Thus, an echo train may be created by dephasing and rephasing the signal in a controlled fashion using subsequent application of refocusing pulses and gradient switching, respectively.

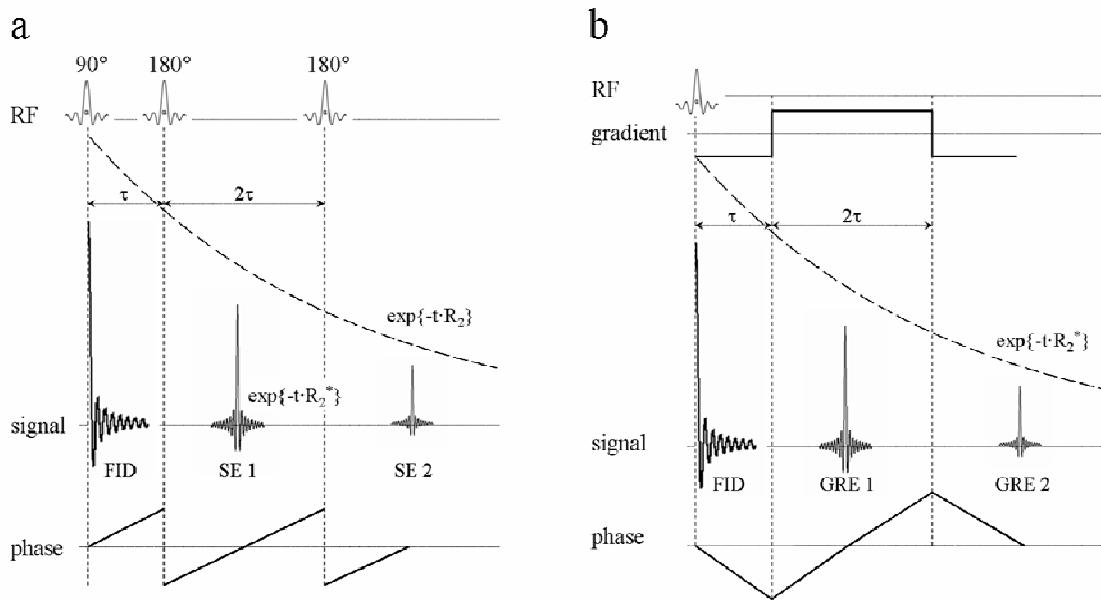


**Figure 3.6** Multi echo spin echo (a) and multi echo gradient echo (b) sequence timing scheme. After an excitation pulse the isochromats lose phase coherence due to spin-spin interactions and magnetic field inhomogeneities.

(a) A  $180^\circ$  pulse applied to the spin system at time  $\tau$  recreates phase coherence at time  $2\tau$ . During spin echoes (SE) time-invariant magnetic field inhomogeneities will be refocused, providing the spins are in a stationary state.

(b) Phase coherence may be achieved by the application of dephasing and rephasing magnetic field gradients. The phase dispersal introduced by the negative gradient is gradually reduced over time after the positive gradient is turned on. In gradient echoes (GRE), phase shifts due to static field inhomogeneities superimposed to the imaging gradients are not refocused and induce significant signal dephasing.

Fig. 3.6 illustrates the formation of the echo signal for both multi echo spin echo and multi echo gradient echo sequences. During spin echoes, time-invariant magnetic field inhomogeneities will be refocused, providing the spins are in a stationary state and spin diffusion effects can be neglected. Although each side of an echo carries a  $R_2^*$  decay, the amplitude of a spin echo is  $R_2$  weighted.

In contrast, for gradient echo techniques the loss of phase coherence within the ensemble of magnetic moments resulting from random field fluctuations is irreversible, and the gradient echoes amplitudes show a  $R_2^*$  decay. The presence of magnetic field inhomogeneities superimposed to the imaging gradients allows the spin system not to be completely rephased by the gradient reversal.

Anticipating a monoexponential decay, the signal intensity  $S(TE)$  in a spin echo experiment is related to the echo time  $TE$  according to [Mac87]:

$$S(TE) = A_1 \cdot \exp(-R_2 \cdot TE) + A_2. \quad (3.4)$$

In this regression,  $A_1$  refers to the equilibrium magnetization prior to sequence repetition, while  $A_2$  refers to the level of the noise. In the gradient echo case, the signal decay is related to the relaxation rate  $R_2^*$ .

### 3.2.3 Determination of relaxivities of contrast media

The longitudinal  $r_1$  and transverse  $r_2$  relaxivities of a contrast media complex are defined as the enhancement of the relaxation rates  $R_1$  and  $R_2$ , respectively, induced by 1 mmol of the paramagnetic center (bound to one water molecule) per liter [Aime99]. Usually it is measured on a range of concentrations and is defined as the slope of the regression line of relaxation rates  $R_1$  and  $R_2$ , respectively, against concentration. However, this description implies a constant relaxivity that is independent of the concentration (i.e., a linear relaxation rate – concentration response).

One aim of the present study was to determine, whether this standard definition applies for the dependency of relaxation rate and concentration over a large concentration range. The investigations were performed for each of the three gadolinium contrast agents examined and also for iron oxide labeled cells at magnetic fields  $0.2 \text{ T} \leq B_0 \leq 3 \text{ T}$ .



### 3.3 Materials and methods

#### 3.3.1 Relaxivity of gadolinium contrast agents in human blood plasma

##### Preparation of blood plasma samples

Commercially-available formulations of 0.5 mol/L Gd-BOPTA, 0.5 mol/L Gd-DTPA, and 1.0 mol/L Gd-BT-DO3A were mixed with samples of human blood plasma in small tubes ( $11 \times 1.6$  cm) to obtain final concentrations of 0.01, 0.02, 0.03, 0.06, 0.13, 0.25, 0.5, 1, 2, 4, 8, 16, 32 and 64 mM. These tubes were placed in a circulating water bath at a constant temperature of  $37 \pm 0.5$  °C (Fig. 3.7). The blood plasma samples were obtained from two healthy individuals and pooled to obtain a single plasma sample for use in all subsequent MR measurements. Aliquots of the plasma sample were drawn for subsequent mixing with contrast agent formulations. The total plasma protein concentration was 78 mg/ml.

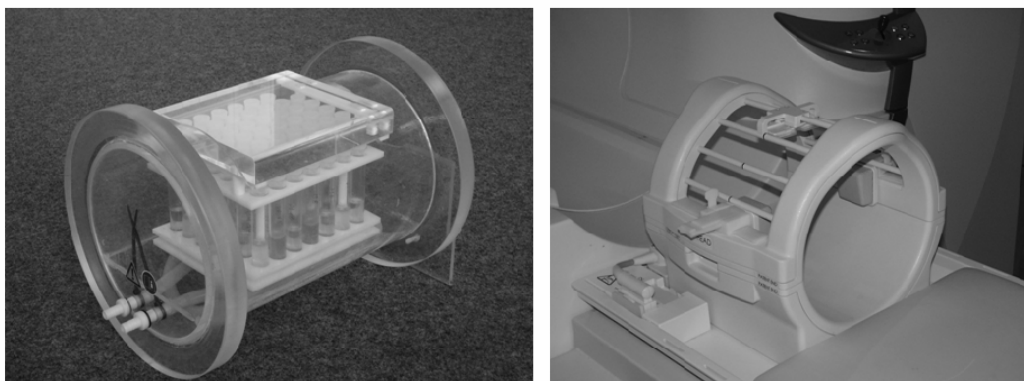


**Figure 3.7** The blood plasma samples were placed in a circulating water bath (left image) that was engineered to be accommodated in the head coil (right image) during MR measurements.

##### MR measurements

All measurements were performed using clinical whole body MR scanners operating at 0.2 Tesla (Magnetom Concerto<sup>®</sup>, Siemens Medical Solutions, Erlangen, Germany), 1.5 Tesla

(Magnetom Sonata<sup>®</sup>), and 3 Tesla (Magnetom Trio<sup>®</sup>). Signal detection was achieved in each case using the respective receiver head-coils, while radiofrequency transmission was performed using a body coil on the 0.2 Tesla and 1.5 Tesla systems and the transmit/receive head coil on the 3 Tesla system.

### Measurement of the longitudinal relaxation rate $R_1$

An inversion recovery (IR) imaging technique with fast spin-echo readout was used for reliable assessment of  $R_1$  data for all contrast agent concentrations examined. The inversion time TI was varied in 19 steps between 23 ms and 8 s. For derivation of  $R_1$  the MR signal intensity  $S_{IR}$  was registered as a function of TI. It was not necessary to introduce a variable parameter to account for an inaccurate inversion since the inversion was performed using an adiabatic inversion pulse without slice selection. This procedure led to a 180° inversion over the entire slice imaged.

In addition, TR was several times longer (i.e., TR was adjusted to 5000 ms + TI) than the maximal  $T_1$  values of the samples, even for low concentrations of contrast agent. The large number and the selection of sampled TI values allowed for an accurate determination of the longitudinal relaxation rates over a large range of values and contrast agent concentrations. The other sequence parameters were as follows: TE = 16 ms (0.2 T) or 9 ms (1.5 T, 3 T), bandwidth = 200 Hz/pixel, field of view (FoV) = 192×192 mm<sup>2</sup>, matrix size = 192×144, slice thickness = 8 mm (0.2 T) or 4 mm (1.5 T, 3 T).

The longitudinal relaxation rate of human blood plasma in the absence of contrast agent was determined by extrapolating the relaxation rate values of the measured samples. Given the wide range of concentrations and the fact that the measured relaxation rate for the lowest concentration (0.01 mM) would be expected to be not much greater than that of human plasma itself, this was considered a valid approach. Subsequent demonstrations of linearity between relaxation rate and concentration for each of the three contrast agents up to a concentration of 1 mM confirmed the validity of this approach.

Confirmation of the extremely short  $T_1$  determined using the IR technique for samples with Gd concentrations higher than 4 mM was achieved by additionally measuring the flip angle

dependent signal intensities using a 3D gradient echo sequence with short echo times (TE) of 8.6 ms (0.2 T), 2.6 ms (1.5 T) or 3.2 ms (3 T). The other sequence parameters were adjusted accordingly, as follows: TR = 18 ms (0.2 T) or 10 ms (1.5 T, 3 T), bandwidth = 90 Hz/pixel (0.2 T) or 260 Hz/pixel (1.5, 3 T), FoV = 192×192 mm<sup>2</sup>, matrix size = 192×192, slice thickness = 2 mm. Several images were acquired with unchanged TR and receiver adjustments while the flip angle was varied in steps of 5° from 10° to 90°.

The longitudinal relaxation rates determined using flip angle dependent signal intensities were in good agreement with those determined using the IR technique for both the 8 mM and 16 mM concentrations. This justified the use of the IR datasets to calculate representative values for the longitudinal relaxation rates for the contrast agent formulations and the specific concentrations.

### Measurement of the transverse relaxation rate $R_2$

The transverse relaxation rate  $R_2$  was assessed using multi echo sequences with spin echo readout. The sequence parameters at 0.2 Tesla were as follows: TR = 3000 ms, bandwidth = 130 Hz/pixel (0.2 T) and 250 Hz/pixel (1.5 Tesla, 3 Tesla), FoV = 192×192 mm<sup>2</sup>, matrix size = 192×192, slice thickness = 8 mm. The echo time TE used for calculation of relaxivity values was varied in 32 equidistant steps between 13.1 ms and 419.2 ms. Confirmation of the  $R_2$  relaxation rate observed at lower Gd concentrations was achieved with TE times between 20 ms and 640 ms. The transverse relaxation rate of the native human blood plasma was determined by extrapolating the relaxation rate values of the measured samples.

### Assessment of relaxivities $r_1$ and $r_2$

On the basis of the findings of the study, a linear relationship between relaxation rate and concentration was found for Gd-DTPA, Gd-BT-DO3A, and Gd-BOPTA up to a concentration of 1 mM. This permitted the relaxivity to be determined as the slope of the regression line of relaxation rate against concentration for each contrast agent. For Gd-BOPTA concentrations higher than 1 mM the relationship between relaxation rate and concentration was clearly non-linear. To determine relaxivity at these concentrations, the specific relaxation gain according to the standard definition of relaxivity was calculated, i.e.,

$$r_i(c) = \frac{R_i(c) - R_i(0)}{c} \quad (3.5)$$

for both longitudinal ( $i=1$ ) and transverse ( $i=2$ ) relaxation for each concentration greater than 1 mM. The relaxation rates for the native solvent  $R_i(0)$  were determined by extrapolation, as described above.

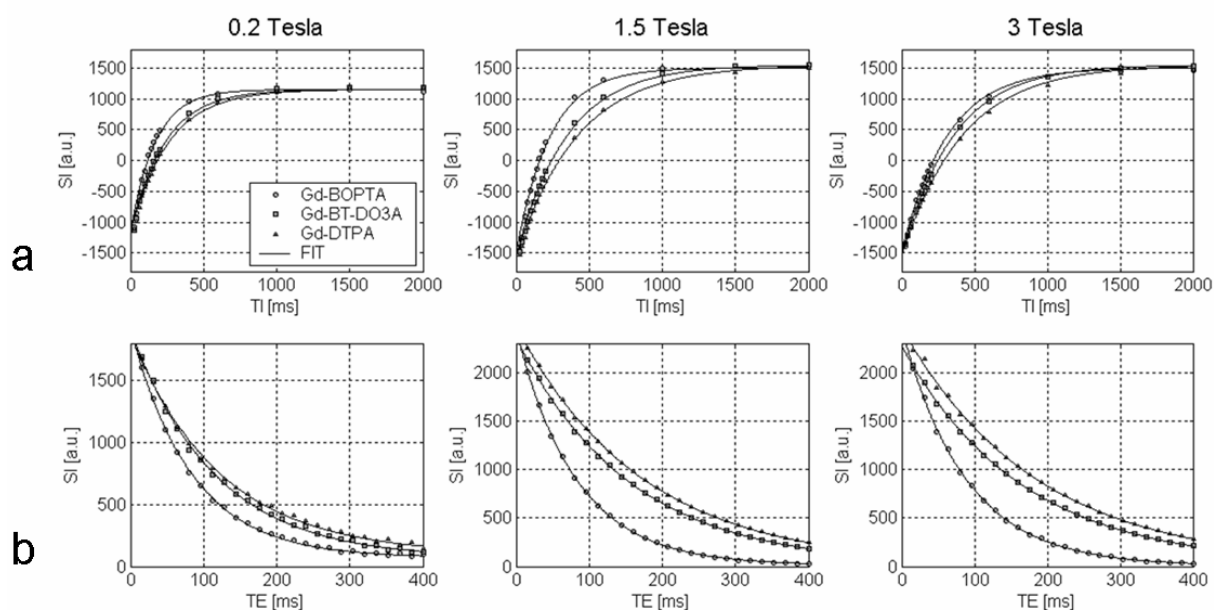


**Figure 3.8** Longitudinal (a) and transverse (b) relaxation curves obtained at 0.2 T, 1.5 T, and 3 T in human blood plasma (37 °C) for a contrast agent concentration of 0.5 mM. SI signal intensity, TI inversion time, TE echo time.

### Estimation of measurement uncertainty

All signal decay curves were assessed by means of individual measurements. The deviation of a data point from the fitted exponential curve was used for assessment of measurement uncertainty. The first regression process was performed to plot signal intensities versus TI or TE, respectively, in order to characterize the longitudinal and transverse relaxation (Fig. 3.8). The obtained deviation was regarded as the measurement uncertainty for determining  $R_1$  and  $R_2$  within our individual study design. The analytical description of error propagation is only possible under the assumption of independent errors. Instead, errors associated with

the determination of all calculated best-fit parameters in the present work were estimated taking into account the full variance-covariance matrix as calculated from the actual data.

Comparable measurements on all MR systems were performed using the same methodological approach. Thus, while pulse sequences and timing were optimized as fully as possible to avoid recalled magnetization from earlier excitations, any systematic errors deriving from non-ideal pulse profiles should at least have been similar for the different field strengths.

### 3.3.2 Relaxivity of iron oxide labeled human melanoma cells

#### Preparation of cell samples

SPIO labeled human melanoma cells (SK-Mel28, average cell size 20  $\mu\text{m}$ ) were used as a cell model. The cells were cultured in Dulbecco's modified Eagle's Medium supplemented with 10 % fetal calf serum, 1 % penicillin-streptomycin, and 1 % L-glutamine at 37 °C in a humidified atmosphere of 5.8 %  $\text{CO}_2$  / 94.2 % air in an incubator (Heraeus, Hanau, Germany). The cells were grown in flat-bottom flasks and labeled by means of incubation with SH U 555A (Resovist<sup>®</sup>, Schering AG, Berlin, Germany). The incubation time was 24 hours, and the iron concentration in the culture medium was 100  $\mu\text{g Fe / ml}$ . SH U 555A is a clinically approved SPIO based contrast media formulation. The SPIO particles are characterized by a crystalline iron oxide core of 4-6 nm and a carboxydextran coating. The hydrodynamic diameter is 63 nm as stated by the manufacturer.

Previous experiments revealed that the use of additional transfection agents yields a higher labeling efficiency. However, agglutination of cells causing inhomogeneities in labeling was observed. Consequently, no additional transfection agents were used in the current study. After incubation, the cells were washed with phosphate-buffered saline (PBS) in order to separate labeled cells from unbound fractions of SPIO particles. The cells were counted electronically (CASY, Schärfe System, Reutlingen, Germany).

Various numbers of approximately  $5 \cdot 10^4$ ,  $25 \cdot 10^4$ ,  $5 \cdot 10^5$ ,  $1 \cdot 10^6$ ,  $2 \cdot 10^6$ , and  $4 \cdot 10^6$  SPIO labeled cells were homogeneously suspended in 50 ml of agar gel (volume concentration agar per

water 1 %; Sigma Chemicals, Germany). Assuming a homogeneous distribution of cells throughout the samples, the preparation resulted in a concentration of  $N = 1, 5, 10, 20, 40,$  and  $80$  SPIO labeled cells /  $\mu\text{l}_{\text{gel}}$ . The potential aggregation of cells in the samples was checked using light microscopy. Those samples showing strong cell clustering were excluded from MR measurement. Only samples with non-agglutinated cells in suspension (Fig. 3.3) were selected for MRI experiments.

In general, SPIO particles are aggregated on the nanometer scale within the labeled cells. Due to the limited resolution of a light microscope (typically  $1 \mu\text{m}$  or somewhat less), the intracellular distribution of SPIO particles cannot be resolved, whereas the spatial distribution of cells can be identified. To investigate the intracellular SPIO distribution electron microscopy was used, which is also shown in Fig. 3.3.

The suspension was filled into plastic tubes. Care was taken to avoid air bubbles in the samples. The control consisted of agar gel (1 %) without any SPIO labeled cells. Prior studies indicated no differences in spin echo and gradient echo signal decay between plain gel and gel mixed with unlabeled cells at the above mentioned concentrations. Under these experimental conditions, the effects of unlabeled cells on water diffusion and magnetic field inhomogeneity were negligible.

## Photometry

Superparamagnetic iron oxide crystalline structures have the formula  $\text{Fe}_2^{3+}\text{O}_3\text{Fe}^{2+}\text{O}$ , where  $\text{Fe}^{2+}$  is the divalent iron ion which was assessed using photometric studies. After incubation with SH U 555A, the cells were washed 3 times with PBS, harvested, counted and the cell pellet was dried for 2 hours at  $80 \text{ }^\circ\text{C}$ . Afterwards, the samples were incubated overnight at room temperature and another 2 hours at  $60 \text{ }^\circ\text{C}$  in perchloric and nitric acid at a 3:1 ratio to completely digest the cells and expose the iron oxide from the carboxydextran coated iron oxide nanoparticles. For the photometric assessment of the iron content, a Ferrozine-based spectrophotometric assay (Eisen Ferene S Plus®, Rolf Greiner Biochemica, Flacht, Germany) was used. The  $\text{Fe}^{2+}$  forms a blue complex with Ferene which can be measured spectroscopically at an absorption wavelength of  $595 \text{ nm}$ . The extinction of the sample

relates directly to the iron concentration, calculated with the help of a defined standard curve. The average iron content was determined to 20 pg Fe / cell by means of photometry.

### Spin echo and gradient echo signal decay

In a spin echo experiment the signal loss at an echo time TE is characterized by the relaxation rate  $R_2$ . This constant includes both signal dephasing from transverse relaxation due to spin-spin interactions as well as signal dephasing arising from the diffusion of spins in inhomogeneous magnetic fields. The free induction signal decay (relaxation rate  $R_2^*$ ) in gradient echo images as a function of the echo time is affected by both transverse relaxation and signal dephasing due to magnetic field inhomogeneities inside the picture elements. Cells loaded with SPIO affect both transverse relaxation and signal dephasing due to magnetic field inhomogeneities. Comparing relaxation rates measured in samples containing SPIO labeled cells to those of unlabeled control samples, the enhancements  $\Delta R_2$  and  $\Delta R_2^*$  of the respective relaxation rate constants  $R_2$  and  $R_2^*$  were determined.

### MR measurements

MR measurements were carried out to study the spin echo and gradient echo signal decay for various concentrations of homogeneously suspended SPIO labeled cells. The volume of the MR imaging voxel was 1  $\mu\text{l}$ . Isotropic spatial dimensions (1.0 $\times$ 1.0 $\times$ 1.0 mm<sup>3</sup>) were chosen. According to the experimental set-up with a homogeneous distribution of cells throughout the sample, cell concentrations of  $N = 1, 5, 10, 20, 40,$  and 80 SPIO labeled cells per imaging voxel were examined.

During the MR examination the samples were accommodated in a water bath at room temperature (20 °C). All measurements were performed using clinical whole body MR scanners operating at 0.2 T (Magnetom Concerto<sup>®</sup>, Siemens Medical Solutions, Erlangen, Germany), 1.5 T (Magnetom Sonata<sup>®</sup>), and 3 T (Magnetom Trio<sup>®</sup>). The signal was detected in each case by means of the respective receiver head-coils, while the radio frequency transmission was performed using the body coil on the 0.2 T and 1.5 T systems and the transmit/receive head coil on the 3 T system, respectively.

Multi-echo spin echo and multi-echo gradient echo sequences were implemented for the measurement of the echo time dependent signal decay. The transverse relaxation rate  $R_2$  was determined using multi-echo sequences with spin echo readout, whereas the apparent relaxation rate  $R_2^*$  was measured using multi-echo sequences with gradient echo readout. For all field strengths the sequence parameters were as follows: field of view (FoV)  $256 \times 256$  mm<sup>2</sup>, matrix  $256 \times 256$ , slice thickness 1.0 mm, repetition time TR 4.000 ms, flip angle  $90^\circ$ , two averages. In the spin echo sequence the echo time TE was varied in equidistant steps between 12 ms and 240 ms. In the gradient echo case the echo time TE was varied in equidistant steps between 10 ms and 100 ms.

For each TE value, the signal intensity was measured in an appropriately large region-of-interest within the samples. Monoexponential functions were fitted to the measured signal decay curves using a least-square regression algorithm. The relaxation rate constants  $R_2$  and  $R_2^*$  as well as the cellular relaxation enhancements  $\Delta R_2$  and  $\Delta R_2^*$  were calculated. For all field strengths the values  $\Delta R_2$  and  $\Delta R_2^*$  were found to be linearly dependent on cell concentration. The slope of the regression line was used as a measure for cellular relaxivity.

### Statistical analysis

Overall, three samples of agar gel and three samples of agar gel doped with a particular concentration of SPIO labeled cells were prepared separately. The cell fractions were obtained from the same population of SPIO labeled cells. For all samples the arithmetic mean and the standard deviation of the measured relaxation rate constants ( $R_2$ ,  $R_2^*$ ) as well as the cellular relaxation enhancements ( $\Delta R_2$ ,  $\Delta R_2^*$ ) were determined.

It should be noted that the preparation technique used might not result in an exact homogeneous distribution of cells. The signal decay was measured in an appropriately large region-of-interest that contained a large number of voxels. Consequently, effects due to an inhomogeneous cell distribution were more than likely averaged out throughout the chosen volume. Furthermore, samples showing strong cell clustering were excluded from MR measurement and only non-agglutinated cells in suspension were selected.



## 3.4 Results of relaxivity measurements

### 3.4.1 Relaxivity of gadolinium contrast agents in human blood plasma

At the highest contrast agent concentrations (32 mM and 64 mM) very fast signal decay resulted in large measurement uncertainties. Since reliable determination of relaxation rates and relaxivities was not possible for these contrast agent concentrations, determination of the  $R_1$  and  $R_2$  relaxation rates for each contrast agent was performed only for concentrations up to and including 16 mM.

#### Relaxation rates of native human plasma

The  $R_1$  and  $R_2$  relaxation rates of human blood plasma alone, as assessed by extrapolating relaxation rate data points for contrast agent concentrations up to and including 1 mM, are shown in table 3.2.

**Table 3.2** Relaxation rates of human blood plasma (37 °C) at 0.2 T, 1.5 T, and 3 T as determined by extrapolation. Values represent mean  $\pm$  standard deviation for determinations with the three contrast agents.

$B_0$ [T]	$R_1$ [ $s^{-1}$ ]	$R_2$ [ $s^{-1}$ ]
0.2	$0.8 \pm 0.1$	$2.8 \pm 0.2$
1.5	$0.5 \pm 0.1$	$2.5 \pm 0.1$
3	$0.4 \pm 0.1$	$2.8 \pm 0.1$

#### Dependence of the relaxation rates on contrast agent concentration

The  $R_1$  and  $R_2$  relaxation rates of human blood plasma plotted against concentration of Gd-DTPA, Gd-BT-DO3A and Gd-BOPTA are shown in Figs. 3.9 and 3.10, respectively, for each magnetic field strength. At concentrations up to 1 mM the relaxation rates of all three contrast agents varied in an approximately linear manner as a function of concentration.

Higher concentrations of contrast agent resulted in higher overall  $R_1$  and  $R_2$  relaxation rates for each of the agents under consideration.

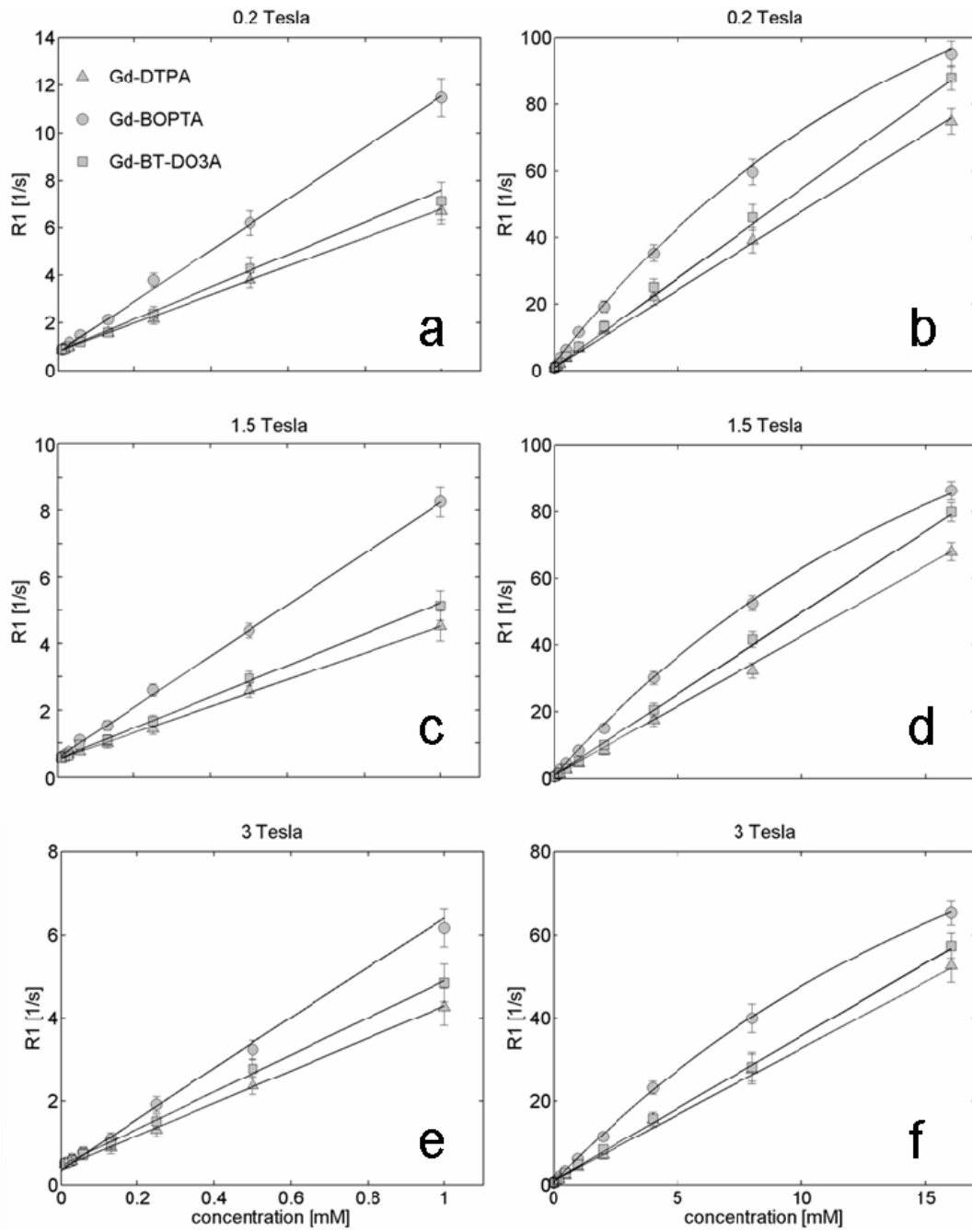


**Figure 3.9** Longitudinal relaxation rate  $R_1$  of human blood plasma (37 °C) for different concentrations of Gd-DTPA, Gd-BT-DO3A and Gd-BOPTA at field strengths of 0.2 T (a, b), 1.5 T (c, d), and 3 T (e, f). Relaxation rates were plotted versus contrast agent concentration up to 1 mM (a, c, e) and up to 16 mM (b, d, f).

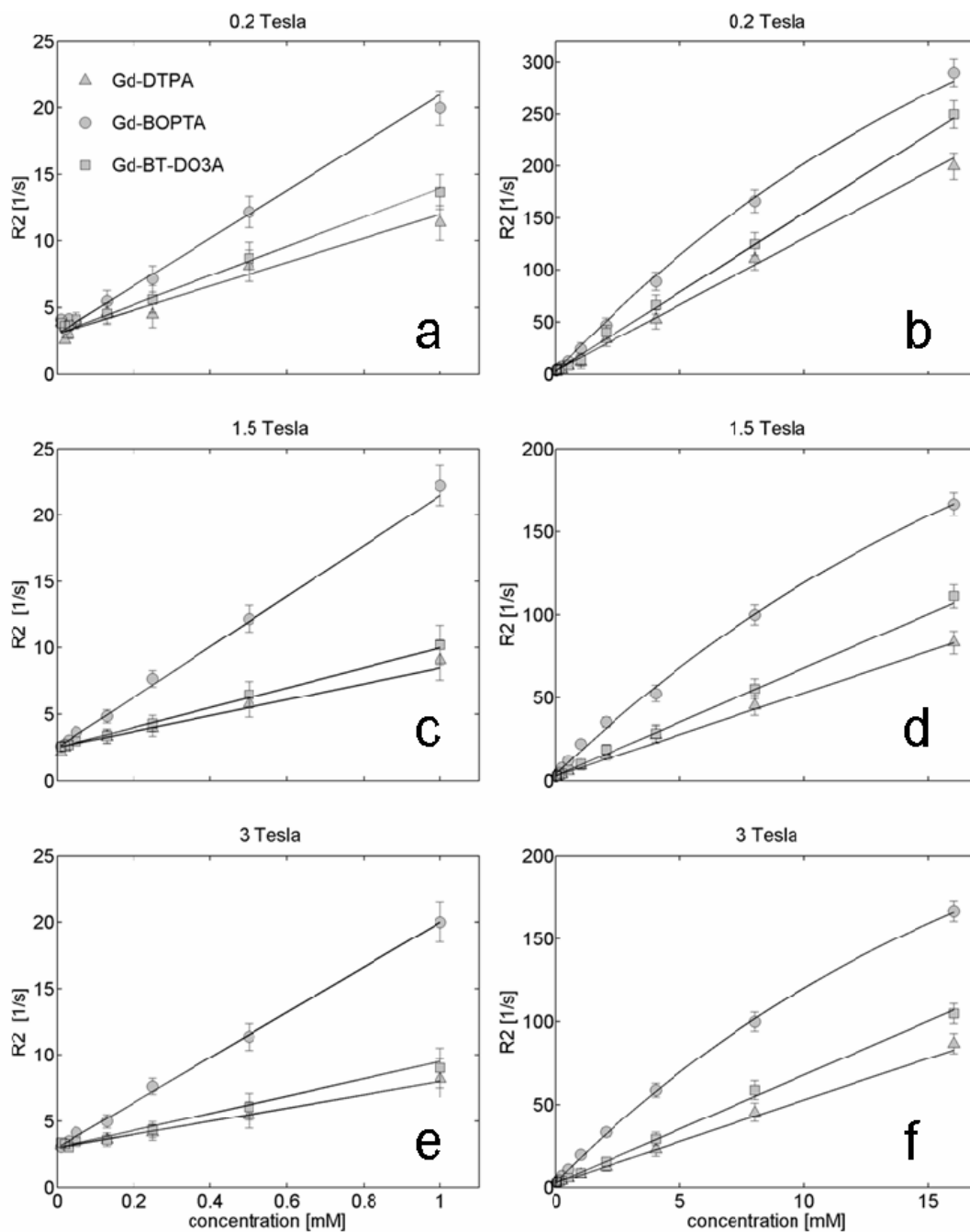


**Figure 3.10** Relationship of transverse relaxation rate  $R_2$  of human blood plasma (37 °C) to concentration of Gd-DTPA, Gd-BT-DO3A and Gd-BOPTA at 0.2 T, 1.5 T, and 3 T.

### Determination of relaxivities

The linearity of the plots for Gd-DTPA, Gd-BT-DO3A, and Gd-BOPTA up to and including the 1 mM concentration permitted determination of the  $r_1$  and  $r_2$  relaxivities over this range

of concentrations (table 3.3). With increasing Gd-BOPTA concentration, significant concentration-dependent reductions of both  $r_1$  and  $r_2$  relaxivity were noted (table 3.4).

### Dependence of the relaxation on magnetic field strength

For each contrast agent the highest values for  $R_1$  relaxation rate and  $r_1$  relaxivity were obtained at the lowest field strength of 0.2 Tesla. Progressively lower  $R_1$  relaxation rates and  $r_1$  relaxivities were noted with increasing magnetic fields of 1.5 and 3 Tesla.

**Table 3.3** The  $r_1$  and  $r_2$  relaxivities in human blood plasma (37 °C) for Gd-DTPA, Gd-BT-DO3A, and Gd-BOPTA at  $B_0 = 0.2$  T, 1.5 T, and 3 T. The relaxivities were calculated for concentrations up to and including 1 mM.

$B_0$ [T]	$r_1$ [ $L \times mmol^{-1} \times s^{-1}$ ]			$r_2$ [ $L \times mmol^{-1} \times s^{-1}$ ]		
	Gd-DTPA	Gd-BT-DO3A	Gd-BOPTA	Gd-DTPA	Gd-BT-DO3A	Gd-BOPTA
0.2	$5.7 \pm 0.3$	$6.6 \pm 0.3$	$10.9 \pm 0.4$	$9.2 \pm 0.3$	$10.7 \pm 0.3$	$18.9 \pm 0.6$
1.5	$3.9 \pm 0.2$	$4.7 \pm 0.2$	$7.9 \pm 0.4$	$5.3 \pm 0.2$	$7.5 \pm 0.2$	$18.9 \pm 0.5$
3	$3.9 \pm 0.2$	$4.5 \pm 0.2$	$5.9 \pm 0.4$	$5.2 \pm 0.3$	$6.3 \pm 0.3$	$17.5 \pm 0.5$

**Table 3.4** The  $r_1$  and  $r_2$  relaxivities in human blood plasma (37 °C) for Gd-BOPTA at  $B_0 = 0.2$  T, 1.5 T, and 3 T.

Relaxivity	$B_0$ [T]	Concentration Gd-BOPTA				
		$\leq 1$ mM	2 mM	4 mM	8 mM	16 mM
Longitudinal $r_1$ [ $L \times mmol^{-1} \times s^{-1}$ ]	0.2	$10.9 \pm 0.4$	$9.2 \pm 0.4$	$8.6 \pm 0.3$	$7.4 \pm 0.3$	$5.9 \pm 0.3$
	1.5	$7.9 \pm 0.4$	$7.2 \pm 0.3$	$6.6 \pm 0.3$	$6.4 \pm 0.3$	$5.4 \pm 0.3$
	3	$5.9 \pm 0.4$	$5.8 \pm 0.3$	$5.6 \pm 0.3$	$5.0 \pm 0.3$	$4.1 \pm 0.3$
Transverse $r_2$ [ $L \times mmol^{-1} \times s^{-1}$ ]	0.2	$18.9 \pm 0.6$	$18.9 \pm 0.6$	$20.1 \pm 0.6$	$20.4 \pm 0.6$	$17.5 \pm 0.6$
	1.5	$18.9 \pm 0.5$	$16.4 \pm 0.4$	$12.5 \pm 0.4$	$12.4 \pm 0.4$	$10.2 \pm 0.4$
	3	$17.5 \pm 0.5$	$15.2 \pm 0.4$	$14.0 \pm 0.4$	$12.7 \pm 0.4$	$9.8 \pm 0.4$

### 3.4.2 Relaxivity of iron oxide labeled human melanoma cells

For all samples examined, the MR signal intensity was homogeneous throughout the sample. Representative MR spin echo and gradient echo images, acquired at different TE, are given in Fig. 3.11. The signal decay could be fitted monoexponentially. A representative example for the spin echo and gradient echo signal decay at magnetic field strengths of 0.2 T, 1.5 T, and 3 T are depicted in Fig. 3.12 for a concentration of 40 SPIO labeled cells /  $\mu\text{l}_{\text{gel}}$ .

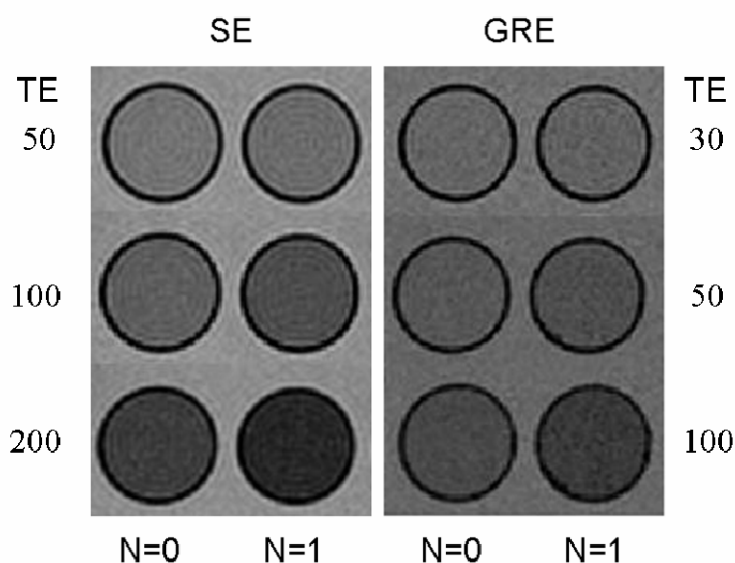


**Figure 3.11** MR images of samples containing no ( $N = 0$ ) and a single ( $N = 1$ ) SPIO labeled cell per microliter agar gel. The images were acquired at 1.5 Tesla using spin echo (SE) and gradient echo (GRE) sequences at echo times TE 50 ms, 100 ms, and 200 ms (SE; from top to bottom) and TE 30 ms, 50 ms, and 100 ms (GRE).

The arithmetic mean of the measured relaxation rate constants ( $R_2$ ,  $R_2^*$ ) as well as the cellular relaxation enhancements ( $\Delta R_2$ ,  $\Delta R_2^*$ ) are summarized in table 3.5. The transverse relaxation was significantly enhanced in samples containing labeled cells ( $N \geq 1$  cell /  $\mu\text{l}_{\text{gel}}$ ) as compared to samples without labeled cells ( $N = 0$  cells /  $\mu\text{l}_{\text{gel}}$ ). In particular, for a concentration of a single labeled cell per  $\mu\text{l}_{\text{gel}}$  increases in  $R_2$  and  $R_2^*$  of 12.2 % and 21.4 % at 0.2 T, and 22.9 % and 65.7 % at 1.5 T and 3 T, respectively, as compared to the unlabeled control samples were found.

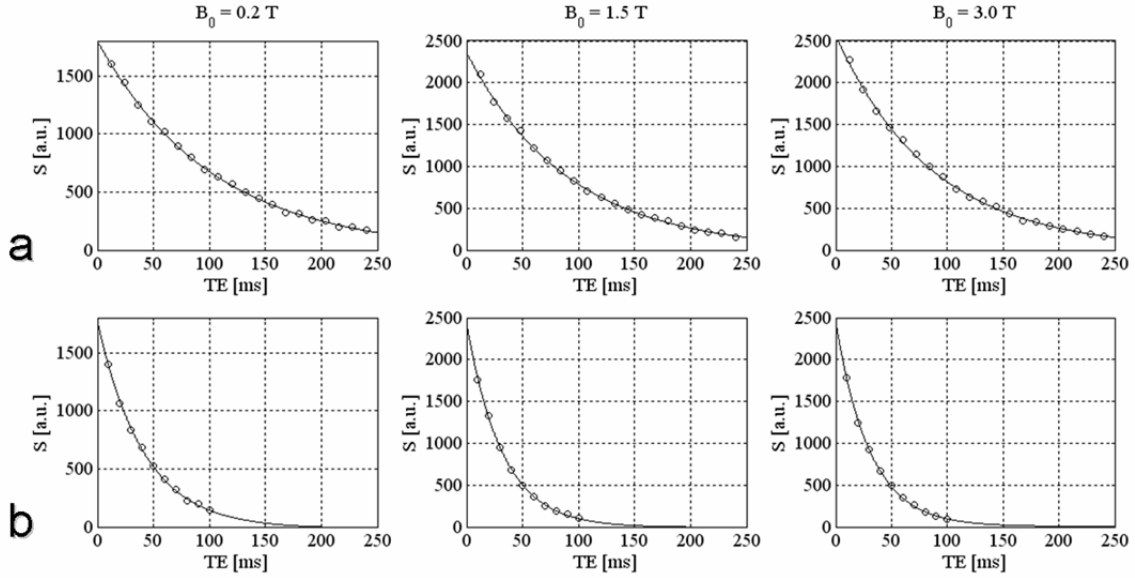


**Figure 3.12** Representative examples of the MR signal decay as measured in a sample containing 40 SPIO labeled cells /  $\mu\text{l}_{\text{gel}}$ . The measurements were performed at 0.2 T, 1.5 T, and 3 T using multi-echo spin echo (a) and multi-echo gradient echo (b) sequences.

**Table 3.5** Mean of the experimental transverse relaxation rates ( $R_2$ ,  $R_2^*$ ) and cellular transverse relaxation enhancements ( $\Delta R_2$ ,  $\Delta R_2^*$ ) for samples containing various concentrations ( $N \geq 1$  cells /  $\mu\text{l}_{\text{gel}}$ ) of SPIO labeled cells as compared to unlabeled control samples ( $N = 0$ ).

N [ $\mu\text{l}^{-1}$ ]	$R_2$ [ $\text{s}^{-1}$ ]			$R_2^*$ [ $\text{s}^{-1}$ ]			$\Delta R_2$ [ $\text{s}^{-1}$ ]			$\Delta R_2^*$ [ $\text{s}^{-1}$ ]		
	0.2 T	1.5 T	3.0 T	0.2 T	1.5 T	3.0 T	0.2 T	1.5 T	3.0 T	0.2 T	1.5 T	3.0 T
0	4.1	4.1	4.2	4.2	4.2	4.3	-	-	-	-	-	-
1	4.6	5.0	5.1	6.1	7.0	7.1	0.5	0.9	0.9	1.9	2.8	2.8
5	5.0	5.2	5.4	8.1	9.4	9.8	0.9	1.1	1.2	3.9	5.2	5.5
10	5.8	6.4	6.6	10.6	12.8	13.3	1.7	2.3	2.4	6.4	8.6	9.0
20	7.4	8.2	8.4	14.9	18.6	19.2	3.3	4.1	4.2	10.7	14.4	14.9
40	9.7	11.1	11.4	24.7	31.7	32.5	5.6	7.0	7.2	20.5	27.5	28.2
80	15.4	18.5	19.0	47.0	61.6	63.7	11.3	14.4	14.8	42.8	57.4	59.4

For all field strengths and all cell concentrations examined the values of  $\Delta R_2^*$  were higher than those of  $\Delta R_2$ . Fig. 3.13 displays a linear relationship between  $\Delta R_2$  respectively  $\Delta R_2^*$  and the cell concentration. This linearity was found for all field strengths examined. In the spin echo case the calculated cellular relaxivities (i.e.,  $d(\Delta R_2) / dN$ ) were  $0.12 \text{ s}^{-1}/(\text{cell}/\mu\text{l})$  at 0.2 T,  $0.16 \text{ s}^{-1}/(\text{cell}/\mu\text{l})$  at 1.5 T, and  $0.17 \text{ s}^{-1}/(\text{cell}/\mu\text{l})$  at 3 T. In the gradient echo case the

cellular relaxivities (i.e.,  $d(\Delta R_2^*) / dN$ ) were  $0.51 \text{ s}^{-1}/(\text{cell}/\mu\text{l})$  at 0.2 T,  $0.69 \text{ s}^{-1}/(\text{cell}/\mu\text{l})$  at 1.5 T, and  $0.71 \text{ s}^{-1}/(\text{cell}/\mu\text{l})$  at 3 T.

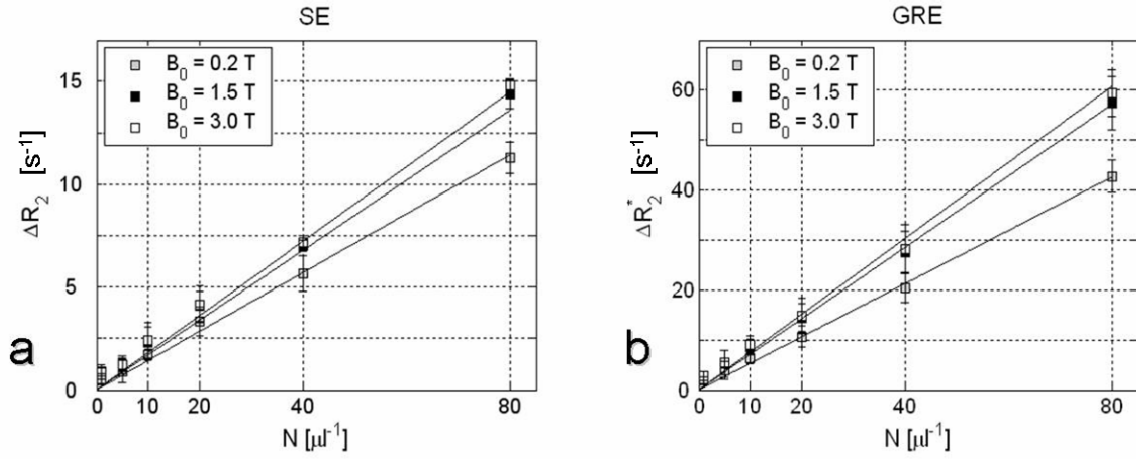


**Figure 3.13** Plots of the mean  $\pm$  standard deviation of cellular relaxation enhancements  $\Delta R_2$  and  $\Delta R_2^*$  for various cell concentrations, magnetic field strengths, and sequence types (a: spin echo, SE; b: gradient echo, GRE).

## 3.5 Interpretation of the results

### 3.5.1 Relaxivity of gadolinium contrast agents in human blood plasma

The present study revealed significant differences between Gd-BOPTA, Gd-DTPA and Gd-BT-DO3A in terms of their potential to enhance longitudinal and transverse relaxation in human blood plasma at 37 °C. The relaxivity of conventional gadolinium based MR contrast agents has been described previously as the slope of the linear regression relaxation rate constants  $R_1$  and  $R_2$  versus concentration. Hence, the relaxivities have been considered constant values [DeHa99]. The results of our study confirm that the relaxation behavior of Gd-DTPA, Gd-BT-DO3A, and Gd-BOPTA follow this concept within the range of concentrations up to and including 1 mM. The measured data are in reasonable agreement with findings from previous studies [DeHa99, Roh05]. Remaining differences of the data can be most likely attributed to inaccuracies of concentration determination and / or species-dependent influences of the blood plasma samples. Furthermore, the data are in consensus with data published previously by Laurent et al. [Lau06], who investigated temperature, concentration and field strength dependencies of the relaxivities of clinical low molecular weight Gd contrast agents.

In the case of Gd-BOPTA, the longitudinal and transverse relaxation and derived relaxivities are not linearly dependent on concentration because of weak, transient interactions of this chelate with serum proteins [Cav97, Van01]. Recently, a dependence of the relaxation rate of Gd-BOPTA on the concentration of human serum albumin has been demonstrated [Gie06]. In the present study any potential effects of varying albumin content in the samples was minimized by the use of a single pooled sample of blood plasma, drawn from just two individuals. Aliquots from this single bulk sample were used for all MR measurements.

It has been shown previously that the bound fraction of Gd-BOPTA has significantly stronger relaxation effects than the unbound fraction due to the larger size and resulting longer rotational correlation time of the molecule [Port05]. Although the precise mechanism has still to be elucidated, it is clear that the ratio of bound to unbound Gd-BOPTA at any



given moment is concentration dependent. Thus, as the number of protein molecules in blood plasma is limited, the protein – contrast agent interaction becomes saturated at very high concentrations of Gd-BOPTA.

Although previous reports have cited values for  $R_1$  and  $R_2$  relaxation rates for Gd-BOPTA [DeHa99], the manner in which these values have been determined has varied considerably and no attempts have been made to address possible issues of concentration dependency. In this study a linear relationship between relaxation rate and concentration of contrast agent was demonstrated at three magnetic field strengths for all three contrast agents for eight concentrations over the range between 0.01 and 1.0 mmol/L. Because the relaxation rates in our study were determined over the range of physiologically-relevant contrast agent concentrations for which a linear dependence of relaxation rate on concentration was demonstrated, the calculated values for relaxivity are realistic for these three contrast agents. Conversely, since the relationship between relaxation rate and concentration is non-linear for higher concentrations of protein-interacting contrast agents it is not possible to define a single relaxivity value that is valid for these higher concentrations. Similar results have been reported by Laurent et al. [Lau06]. Thus, the relevant parameter to define the magnitude of contrast enhancement is relaxation rate rather than relaxivity.

At 0.2 Tesla the  $R_2 / R_1$  ratios are approximately 2 for all contrast agents at concentrations below 1 mM. For Gd-DTPA and Gd-BT-DO3A this ratio was similar also at higher field strengths of 1.5 T and 3 T, because both the longitudinal and transverse relaxation rates decrease roughly simultaneously at higher field strengths. Conversely, whereas the longitudinal relaxation rate of Gd-BOPTA shows very strong dependence on the field strength, the transverse relaxation shows only minimal dependence. Therefore, the  $R_2 / R_1$  ratio increases for Gd-BOPTA at higher field strengths up to values near 3.5 at a concentration of 1 mM. This feature should therefore be considered in the choice of sequence for clinical applications: very short echo times should be selected in order to avoid undesired signal loss due to transverse relaxation in regions with high concentration of contrast agent. Although the other contrast agents examined are less demanding in this respect, modern MR scanners usually offer fast three-dimensional angiographic gradient echo sequences with very short echo times of less than 2-3 milliseconds.

### 3.5.2 Relaxivity of iron oxide labeled human melanoma cells

In order to optimize the sensitivity and specificity of MRI to detect SPIO labeled cells under in vivo conditions, the analysis of fundamental parameters that affect the observable MR signal in the presence of labeled cells is of crucial importance. In the current work the most relevant variables like cell concentration and magnetic field strength as well as MR sequence type and sequence parameters have been scrutinized. Various concentrations of homogeneously suspended SH U 555A labeled SK-Mel28 human melanoma cells have been studied in terms of cellular transverse relaxation enhancement in both spin echo and gradient echo sequences for different magnetic field strengths. Such a systematic study is helpful in order to understand the source of image contrast in tissues with an almost uniform distribution of labeled cells.

In contrast, concentration effects have usually been studied for huge cellular aggregations by measuring the SPIO induced signal voids so far. However, the strong magnetic field distortions caused by high local SPIO concentrations led to signal voids that are far larger than the size of the labeled area (see chapter 5). This prevents for a clear discrimination between the contributions of the cell concentration and the extension of the labeled area to the observable signal void in MR images. The area of signal void depends solely on the local total magnetic moment. Hence, identical image signal voids might be attributed to either high local cell concentration or the same amount of cells distributed over a larger area. Using a sample preparation technique as described in the current work, only concentration effects rather than the spatial distribution of labeled cells contributed to the observed signal decay. This allowed studying concentration effects in isolation.

A linear relationship between the cellular relaxation enhancements  $\Delta R_2$  and  $\Delta R_2^*$  and cell concentration was found. This can be related to the numerical results of Fisel et al. [Fis91] as well as Hardy and Henkelman [Har89], who investigated the changes in MR signal caused by increasing volume fractions of magnetic dipoles. It is anticipated that SPIO loaded cells behave as magnetic dipoles, since the magnetic field created by any SPIO loaded cell is sensitive to its shape and intracellular distribution of magnetic moments only in close proximity to the cell (see chapter 4). In the present experiments the total volume fraction of SPIO labeled cells (i.e.,  $\ll 1\%$  for  $N = 80$  cells /  $\mu\text{l}_{\text{gel}}$ ) was small as compared to the size of

the MRI voxel (i.e., 1  $\mu$ l). Thus, the majority of water molecules that contributed to the signal decay experienced only the magnetic dipole field outside the SPIO labeled cells.

For all field strengths examined the gradient echo transverse cellular relaxivities were higher as compared to the spin echo transverse cellular relaxivities. For a certain concentration of labeled cells, the enhancements in gradient echo  $R_2^*$  are superior to the enhancements in spin echo  $R_2$ , and gradient echo sequences are anticipated to be more sensitive to SPIO loaded cells than the spin echo sequences. The enhanced  $R_2^*$  relaxation with increasing SPIO concentration was primarily due to increasing magnetic field inhomogeneities. In contrast, enhancement of the  $R_2$  relaxation with increasing SPIO concentration is expected to be caused by diffusion of spins through these magnetic field inhomogeneities. Non-linear saturation effects of the cellular relaxation rate–concentration relationship were not found within the range of SPIO concentrations investigated. However, at higher concentrations and higher cell magnetizations, a saturation effect might be possible [Roch99].

In the current work the cellular transverse relaxation enhancement was measured for various concentrations of SPIO loaded cells. It should be noted that cellular relaxivity data cannot be adequately compared to the common relaxivity values obtained from measurements in liquid solutions. Furthermore, as reported by Simon et al. [Sim06], free extracellular ferumoxtran-10 ultrasmall superparamagnetic iron oxide (USPIO) particles have shown a higher  $R_2$  relaxivity as opposed to intracellular compartmentalized USPIO. These findings might be explained with regard to the numerical simulations described in chapter 4. These demonstrate faster static MR signal decay in case of uniformly distributed magnetic dipoles (e.g., SPIO in liquid solution) as compared to compartmentalized magnetic dipoles (e.g., SPIO ingested in cells).

The marginal increases in spin echo and gradient echo cellular transverse relaxivity observed at 3 T as compared to 1.5 T are thought to be due to saturation effects of the SPIO magnetization. The magnetization saturation for magnetic fields beyond 1.5 T implies that higher field strengths will not necessarily cause more intense magnetic field inhomogeneities and higher susceptibility contrast. For example, Falkenhausen et al. [Falk05] reported that SH U 555A enhanced MR liver imaging at 3 T in comparison to 1.5 T did not result in an increase in contrast between liver and liver lesions. Moreover, Simon et al. [Sim06] found the transverse relaxivity of USPIO to be only moderately higher at 3 T compared to 1.5 T.

In order to optimize the MR sensitivity to quantify effects of magnetically labeled cells, well suited tissue specific models can be derived on the basis of the proposed quantification. The magnetic field distributions and the relaxation rate constants on a microscopic scale under in vivo conditions are anticipated to be different from those of the homogeneous agar gel phantom. However, since the underlying physical principles are identical for both situations, the quantitative assessment of the spin echo as well as the gradient echo cellular transverse relaxivity in dependence on the concentration of SPIO loaded cells under in vivo conditions is possible. The results reported herein should be transferable to other cell types, as the physics describing cellular relaxation enhancement is indifferent to cell type. In conclusion, the proposed preparation technique is a simple and reliable approach to quantify effects of magnetically labeled cells.

## Chapter 4

# Microscopic intra- and extracellular magnetic field inhomogeneities

### 4.1 Physical and biological background

Cells loaded with superparamagnetic iron oxide (SPIO) cause relatively strong magnetic field distortions, implying that magnetic field superposition effects of neighboring SPIO loaded cells must be accounted for. Thus, magnetically labeled cells cause complex intravoxel magnetic field distributions. However, a coherent understanding of the various effects of labeled cells on the resonance frequency distribution and the MR signal decay has not been achieved so far.

In the current study, the magnetic field perturbations due to magnetically labeled cells were studied using a three-dimensional (3d) numerical model. The effects of the intracellular distribution of magnetic moments on the resulting extracellular magnetic field were scrutinized. Various geometries including the homogeneous intracellular SPIO distribution, the allocation of SPIO within magnetic subcompartments, and the attachment of SPIO to the cell's surface were considered. The magnetic field distortions, the intravoxel resonance frequency distribution, and the MR signal decay were computed in all of these cases.

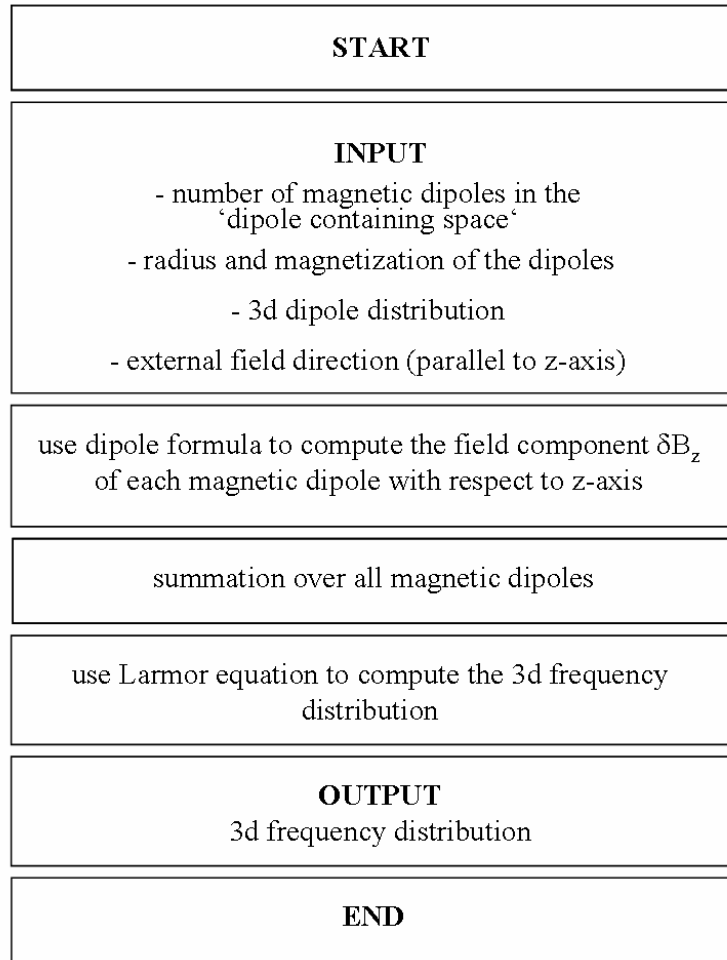


**Figure 4.1** Program flow chart used for the computation of the 3d magnetic field and frequency distribution in presence of magnetic dipoles. Computing the frequency at each location demanded summation over the contributions from all magnetic dipoles.

The question how the spatial distribution of SPIO labeled cells affects the magnetic field distribution is still an open one. This study was aimed at a deeper understanding of how the spatial distribution of SPIO loaded cells affects the resonance frequency distribution and hence the MR signal. Different spatial distributions of magnetically labeled cells might be attributed to well-defined physiologic and pathologic processes as well as to differences in the individual migration behavior of cells after transplantation or injection.

This fact is of critical importance for the in vivo quantification of SPIO loaded cells since in tissues with different spatial distributions of identical SPIO concentrations different signal decays might be observed. Magnetically labeled cells were treated as magnetic dipoles in a homogeneous external magnetic field and the effect of spatial distribution of magnetic dipoles

on the Larmor frequency distribution and the related MR signal decay was investigated. The simulations were performed under the conditions of the static dephasing regime.

In addition, microscopic field variations related to cell division have been addressed. The low toxicity of SPIO nanoparticles allows for cellular iron loads up to 100 pg Fe / cell without significant adverse side effects on the cell viability [DeVr05, Bow02, Metz04]. Furthermore, the effects of SPIO on cell proliferation and differentiation have been under investigation. Himes et al. [Him04] have shown that embryonic stem cells loaded with SPIO compared to unlabeled cells had similar viability and proliferation profiles for up to 14 days. Arbab et al. [Arb05] have demonstrated that labeling cells with ferumoxides [Jung95] did not inhibit the function nor differentiation capacity of hematopoietic or mesenchymal stem cells. It is anticipated that the spatial distribution of iron oxide loaded cells within the target tissue following the transplantation of ex vivo labeled cells is affected by cell division. It is reasonable to assume that the sharing of the parent cell's SPIO load among an increasing number of daughter cells, due to cell division, affect the local magnetic field distribution.

## 4.2 3d numerical model

The field distribution in the presence of magnetic dipoles as placed in a homogeneous external magnetic field was studied using a 3d numerical model. The program was written in C++ (Microsoft Visual C++). The model based on expertises derived from previous numerical simulations [Bha92, Mue04, Mue05] and was adapted to compute the field distribution in the presence of magnetically labeled cells [Pint06a]. All simulations were performed under static conditions and the position of each computational unit was fixed with respect to the 3d volume grid. Diffusion effects of water molecules were not considered in the model.

The program flow chart developed is shown in Fig. 4.1. Within the model, varying numbers of magnetic dipoles were assigned to a 3d volume grid, which was referred to as the 'dipole universe' (i.e., the dipole containing space). For the calculation of the magnetic field distribution in the region-of-interest (ROI) as the center part of the 'dipole universe', the local magnetic field distortions originating from adjacent and surrounding volume elements must be taken into account (Fig. 4.2).

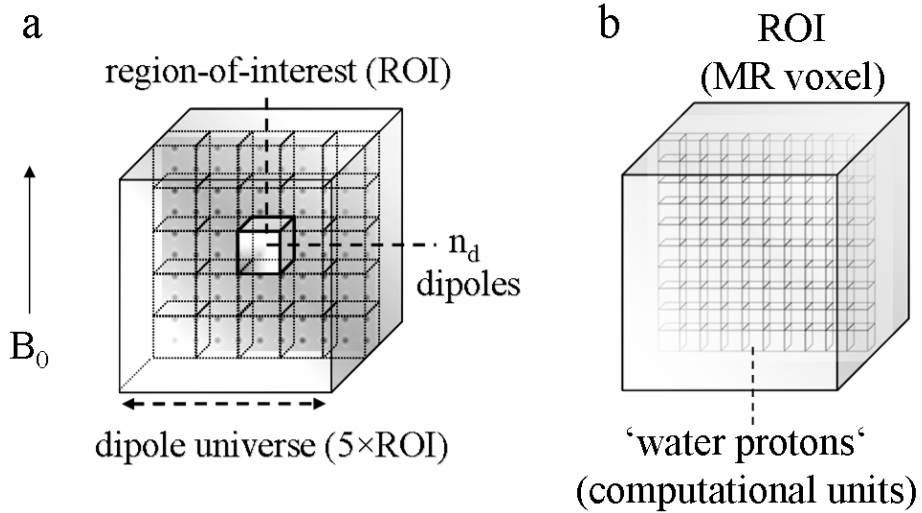


**Figure 4.2 (a)** Schematic representations of magnetic dipoles distributed in the ‘dipole universe’ (i.e., the dipole containing space). To avoid boundary effects in the computation of the 3d magnetic field distribution within the region-of-interest (ROI), the field contributions of all magnetic dipoles in adjacent and surrounding volume elements were taken into account.

**(b)** The ROI consisted of a grid of identical computational units (‘water protons’). For each of the computational units the magnetic field component was computed with respect to the external magnetic field.

To prevent for the influence of boundary effects, which may arise if the magnetic fields from adjacent voxels are not considered, the overall size of the dipole containing space was chosen to  $5 \times \text{ROI}$  in each dimension (Cartesian coordinates  $x, y, z$ ). The size of this ‘dipole universe’ was allowed to vary from  $3 \times \text{ROI}$  to  $9 \times \text{ROI}$  and subsequently no significant changes in the computed frequency distribution within the ROI were found by letting this region be larger than  $5 \times \text{ROI}$ . To compute the field distribution due to  $n_d$  magnetic dipoles within the ROI, for the present simulation parameters, a number of  $5^3 \times n_d$  dipoles had to be distributed throughout the ‘dipole universe’.

The field perturbation  $\delta B_z$  of a magnetic dipole with respect to the axis of the external magnetic field (i.e., the  $z$ -axis) is given by the dipole formula [Sch96].

$$\delta B_z(\mathbf{r}, \Phi) = \frac{P_m}{4 \cdot \pi \cdot r^3} \cdot (3 \cdot \cos^2 \Phi - 1) . \quad (4.1)$$



In this equation  $p_m$  is the magnetic moment,  $r$  is the distance from the dipole center, and  $\Phi$  is the angle with respect to the main magnetic field  $\vec{B}_0 = B_0 \cdot \vec{e}_z$ . This dipolar field is identical to the field inhomogeneity outside ( $r > a$ ) a spherical object, and  $\delta B_z$  is given by [Sch96]

$$\delta B_z(r, \varphi) = \frac{M}{3} \cdot \left(\frac{a}{r}\right)^3 \cdot (3 \cdot \cos^2 \varphi - 1) . \quad (4.2)$$

Here, ‘M’ is the difference in the bulk magnetization with respect to the surroundings and ‘a’ is the radius of the spherical object. A representative example of the magnetic dipole field is given in Fig. 4.3 and Fig. 4.4.

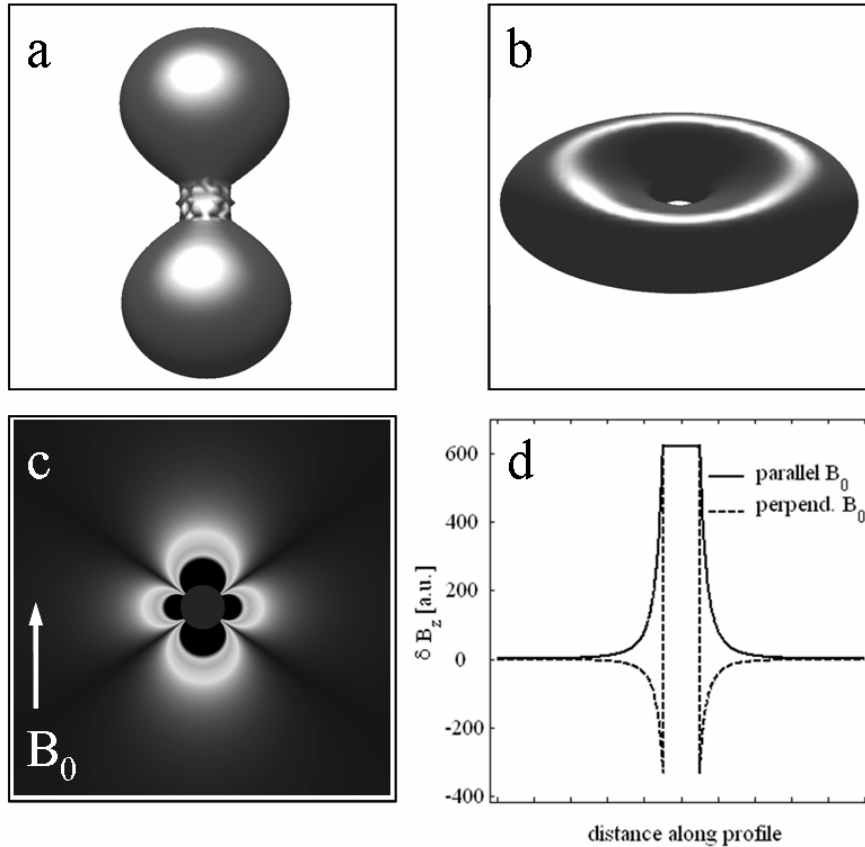


**Figure 4.3** Magnetic dipole field around a magnetic sphere computed with respect to the external homogeneous  $\vec{B}_0$ -field. (a, b) 3d plots of the magnitude of field distortion. The field is enhanced at the poles (a) and diminished at the equator (b). Note that in (a) the magnetic field is enhanced for a paramagnetic sphere. Minor simulation artefacts are visible in that region. (c) Cross section through the 3d field distribution. (d) Field distortion along profiles parallel and perpendicular to  $\vec{B}_0$ .

For computing the overall field distribution due to arbitrarily shaped magnetic material, the induced field must be added to the homogeneous external magnetic field. However, to assess the changes in the Larmor frequency distribution, only the magnitude of the additional field caused by the magnetic dipoles is to be computed in the 3d volume grid.

For each computational unit in the ROI volume grid, the corresponding shift in the resonance frequency  $\delta\nu$  was calculated according the Larmor equation

$$\delta\nu = \gamma \cdot \delta B_z \quad (4.3)$$

with  $\gamma$  the gyromagnetic ratio ( $\gamma = 42.58$  MHz / Tesla for  $^1\text{H}$ ). Frequency histograms as the sum over each voxel in the ROI were calculated and postprocessed in MatLab<sup>®</sup> (Version 6.5, The Mathworks, Natick, MA, USA). Lorentzian functions (variance  $\sigma_B^2$ ) according to

$$p(\delta\nu)_{\text{Lorentz}} = \frac{1}{\pi} \cdot \left[ \frac{\sigma_B}{\sigma_B^2 + \delta\nu^2} \right] \quad (4.4)$$

were fitted to the calculated frequency histograms using a least square algorithm.

For practical reasons the transverse relaxation resulting from the spin-spin interactions was not modelled. The aim of this numerical model was to investigate the signal dephasing due to the magnetic field inhomogeneities for various spatial distributions of magnetic dipoles respectively magnetic spheres.

In MRI each tissue is characterized by the distribution of dephasing frequencies  $p(\omega)$ . The signal obtained from within a voxel is

$$S(t) = \int_{-\infty}^{+\infty} p(\omega) \cdot [M_x(\omega) + i \cdot M_y(\omega)] \cdot e^{i\omega t} d\omega. \quad (4.5)$$

For a gradient echo sequence such as FLASH (Fast Low Angle SHot), the response profile  $M_x(\omega) + i \cdot M_y(\omega)$  is a constant [Zie05b] in absence of transverse relaxation and the free induction signal decay (FID) of the signal  $S(t)$  is the Fourier transform of the frequency distri-

bution (for appropriate long  $T_2$ ). To assess the FID, the frequency histograms were transformed using a discrete Fourier transformation with  $2^{12} = 4096$  equally spaced data points in the range of  $-425.8 \text{ Hz} \leq \delta\nu \leq +425.8 \text{ Hz}$ . Monoexponential functions were fitted to the calculated FID. This work focuses on the form of the distribution  $p(\omega)$  due to different types of spatial distribution of magnetically labeled cells.

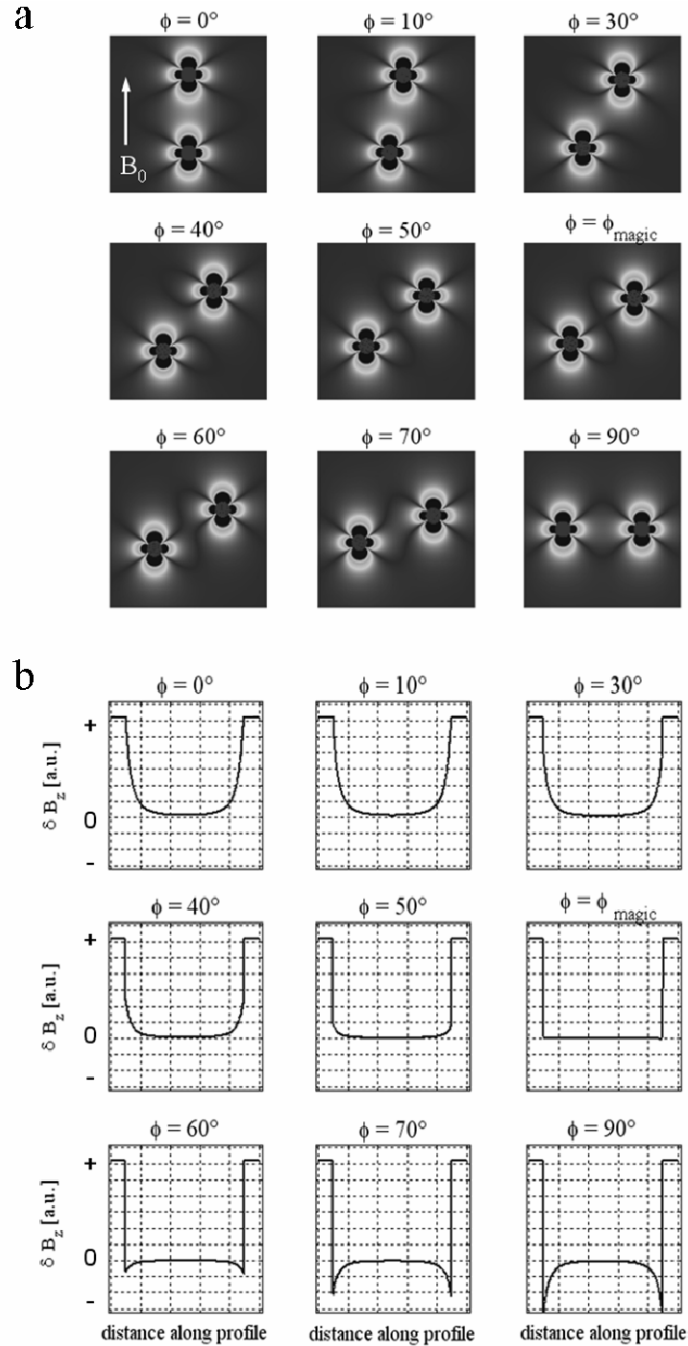


**Figure 4.4** (a) Orientation of two magnetic dipoles with respect to the external homogeneous  $B_0$ -field. (b) The magnetic field inhomogeneities along the interdipolar vector between the centers of the two magnetic dipoles are displayed. The ‘dipole-dipole coupling’ along the interdipolar vector vanishes for the ‘magic angle’ ( $\Phi = 54.7^\circ$ ).

## 4.3 Materials and methods

### 4.3.1 Magnetic field distortion around magnetically labeled cells

#### General considerations

The magnetic susceptibility is a measure for the magnetization  $M$  of an object in presence of a magnetic field. Cells labeled with SPIO induce intense magnetic field inhomogeneity effects. The ,effective magnetization'  $\tilde{M}$  of a labeled cell is given by the entirety of the magnetic moments of the SPIO particles used for labeling this cell. Assuming the SPIO particles to induce field distortions comparable to those of magnetic dipoles, the magnitude of the ,magnetic moment' of the dipole  $p_m$  is given by

$$p_m \propto M \cdot a^3. \quad (4.6)$$

Here , $M$ ' is the magnetization of the particle and , $a$ ' is its radius. For  $n$  magnetic particles the ,total magnetic moment'  $P_m$  is

$$P_m = n \cdot p_m \propto n \cdot M \cdot a^3. \quad (4.7)$$

Assuming a spherical cell containing a number of  $n$  magnetic dipoles (i.e.,  $P_m$  is assigned to that cell), the total magnetic moment of the cell is

$$P_m \propto \tilde{M} \cdot \tilde{a}^3. \quad (4.8)$$

Here  $\tilde{a}$  is the ,effective radius' of the cell and  $\tilde{M}$  is its ,effective magnetization'. The combination of equations (4.7) and (4.8) yields an expression for the effective magnetization of the magnetically labeled cell.

$$\tilde{M} = n \cdot M \cdot \left(\frac{a}{\tilde{a}}\right)^3. \quad (4.9)$$

The present approach allows studying the effect of the intracellular iron oxide particle distribution on the extracellular magnetic field. The ‘total magnetic moment’  $P_m$  of the labeled cell is regarded as a constant.

### Geometries of magnetic material inside cells

Various geometries including the homogeneous intracellular magnetic particle distribution, the allocation of magnetic particles in magnetic subcompartments, and the attachment of particles to the cell’s surface (e.g., due to receptor-mediated labeling) were modelled. The SPIO particles were treated as magnetic dipoles. These were confined to a sphere with radius  $\tilde{a}$  (i.e., the cell) and arranged according to well-defined geometries, which reflected the cell labelling characteristics. The geometrical considerations used to model these effects are summarized in Table 4.1 below.

**Table 4.1** *Magnetic dipole characteristics considered for the simulation of the extracellular magnetic field around cells labeled with magnetic nanoparticles. Radius and magnetization of the particles are given in units of an ‘effective radius  $\tilde{a}$ ’ and an ‘effective magnetization  $\tilde{M}$ ’. This are the radius and the magnetization, respectively, of a magnetic reference sphere with the same total magnetic moment. For all dipole geometries simulated, the total magnetic moment  $P_m$  was constant, to read  $P_m \propto n \cdot M \cdot a^3 = \tilde{M} \cdot \tilde{a}^3$ .*

cell label characteristics	model	number n	magnetic particles	
			radius a	magnetization M
a) intracellular particle distribution	regular distribution of magnetic particles	52	$1/8 \tilde{a}$	$9.85 \tilde{M}$
		12	$1/4 \tilde{a}$	$5.33 \tilde{M}$
b) magnetic particles aggregated to magnetic subcompartments	magnetic particle assigned to the sphere’s center	1	$1/4 \tilde{a}$	$64 \tilde{M}$
		1	$1/2 \tilde{a}$	$8 \tilde{M}$
c) particles at the cell’s surface	distribution of magnetic particles on the sphere’s surface	20	$1/8 \tilde{a}$	$25.6 \tilde{M}$
d)	magnetic reference sphere	1	$\tilde{a}$	$\tilde{M}$

The numerical model, as described above, was applied. The volume grid consisted of  $100 \times 100 \times 1$  computational units. The direction of the plane-of-view was parallel to  $\vec{B}_0$ . The simulation parameters radius and magnetization assigned to the magnetic particles are given in units of  $\tilde{a}$  and  $\tilde{M}$ , respectively, in Table 4.1. The total magnetic moment of the ‘labeled cell’ was treated as a fixed quantity: The total magnetic moment was constant for all dipole geometries simulated. Furthermore, the magnetic field around a magnetic sphere with the same magnetic moment was computed. This reference sphere had radius  $\tilde{a}$  and magnetization  $\tilde{M}$ .

### Relative field difference

The magnetic field distribution computed for specific particle geometries was compared to the magnetic field due to a magnetic reference sphere with the same total magnetic moment. The ‘relative field differences  $\Delta$ ’ in the respective field distributions were evaluated on a voxel-by-voxel basis.

$$\Delta = \frac{|\delta B_z^{\text{sphere}}| - |\delta B_z^{\text{particles}}|}{|\delta B_z^{\text{particles}}|} \quad (4.10)$$

Here  $\delta B_z^{\text{sphere}}$  and  $\delta B_z^{\text{particles}}$  are the magnetic field distortions around a magnetic sphere and around well-defined geometries of magnetic particles, respectively.

### 4.3.2 Spatial distribution of magnetic material

#### Random distribution of magnetic dipoles

The 3d frequency distribution was studied for various spatial distributions of magnetic dipoles. For all simulations the 3d volume grid in the ROI was chosen to  $100 \times 100 \times 100 = 10^6$  equally sized computational units. The ‘dipole universe’ consisted of  $5^3 \times 10^6$  computational units. For all simulations the volume fraction (total volume of magnetic dipoles / 3d volume) was kept constant at 0.01 %. The magnetization  $M$  specifies the volume density of magnetic moments and was 2 mT.

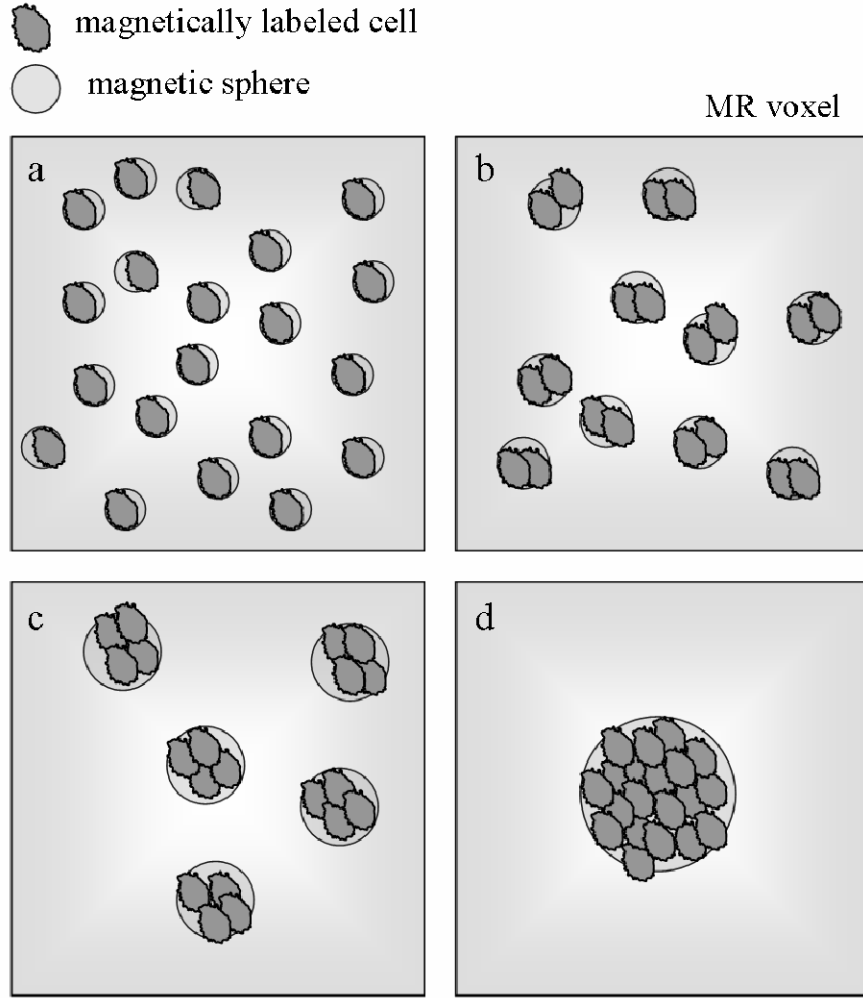


**Figure 4.5** The distribution of magnetically labeled cells within an imaging voxel. The cells may be uniformly distributed or may aggregate to cell clusters. The degree of cell aggregation increases from (a) to (d). Uniformly distributed cells are shown in (a), whereas all cells are aggregated within a cell cluster in (d). Variations in the intravoxel magnetic field distributions related to the formation of aggregations of magnetically labeled cells were studied. Aggregations of labeled cells were considered as magnetic spheres with varying number and volume, but constant magnetization.

The frequency distribution caused by a varying number, but a constant volume fraction of magnetic dipoles, was analyzed (Fig. 4.5). The number of magnetic dipoles in the ROI was varied from  $n_d = 1$  to  $n_d = 65,536$  in logarithmic steps. For a single magnetic dipole ( $n_d = 1$ ) the radius was  $a(n_d = 1) = 2.8$  computational units. Maintaining the constancy of volume fraction, for an increasing number of magnetic dipoles, the radius  $a(n_d)$  was given according to

$$a(n_d) = \frac{a(n_d = 1)}{\sqrt[3]{n_d}}. \quad (4.11)$$

The dipoles were distributed randomly throughout the 3d volume grid using a suitable subroutine created by Press et al. [Pre92] to generate random numbers with uniform distribution. The initialization of the random number generator was varied using different initial values, and no significant changes in the computed frequency distribution were found.

### Effects of cell division

Assume that cells (supposed to be a sphere) with a magnetic moment  $p_m$  were injected for therapy. The magnetic moment of each ‘parent cell’ is given according to eq. (4.6). If cell division occurs, in the first generation this leads to two identical daughter cells (radius  $a_d$ ) with half the SPIO load per cell. It is assumed that equal shares of SPIO are allocated to the daughter cells. Thus, due to cell division, a constant magnetic moment  $p_m$  of the parent cell is allocated to an increasing number of daughter cells.

The initial point is a single parent cell. For the  $N^{\text{th}}$  generation, the number of identical daughter cells is  $2^N$  and the magnetization  $M(N)$  of each daughter cell is  $M(N) = M_0 / 2^N$ , where  $M_0$  is the parent cell’s magnetization. This concept is illustrated in Fig. 4.6, along with experimental data demonstrating the proliferation of iron-oxide labeled cells in vitro.

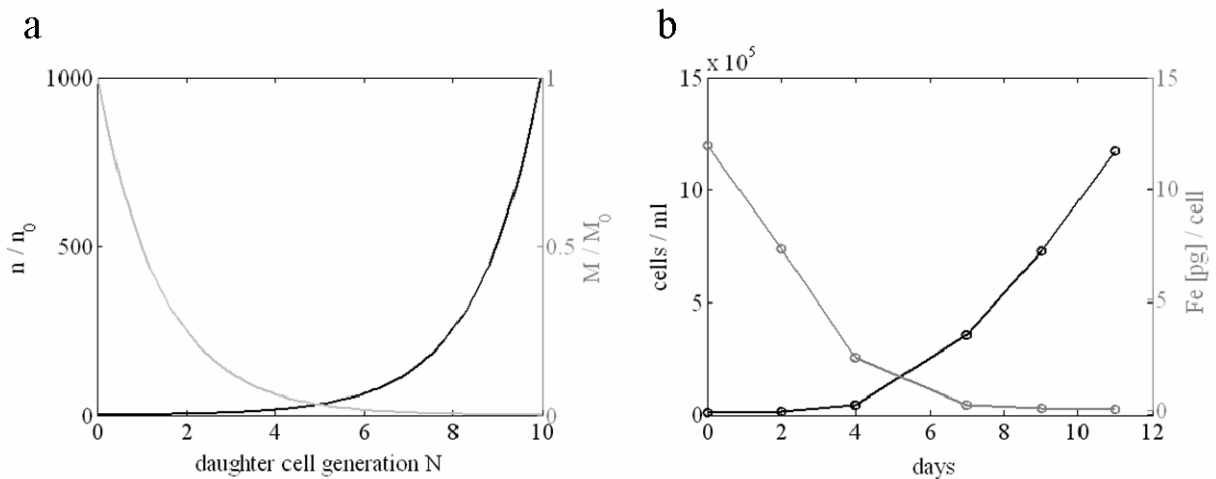


**Figure 4.6** (a) Theoretical increase in cell number  $n/n_0$  due to cell proliferation. For iron oxide loaded cells: the higher the generation of daughter cells, the less the iron load per cell and, as the result of this, the less the cell’s magnetization  $M/M_0$ . (b) Proliferation profile of KG-1a cells labeled with iron oxide nanoparticles (SHU 555A). The average iron label per cell was determined by means of photometry.



In order to model magnetic field inhomogeneity effects related to cell division the 3d magnetic field distribution was studied for various spatial distributions of magnetic dipoles, which were treated as iron oxide labeled parent cells and labeled daughter cells. The dipoles were distributed randomly throughout the 3d volume grid. For all simulations the 3d volume grid in the ROI was chosen to  $100 \times 100 \times 100 = 10^6$  equally sized computational units. The radius of each magnetic sphere (i.e., parent cell, daughter cells) was 3.0 computational units.

The magnetization  $M_0$  of the mother cell was  $M_0 = 3$  mT. The simulations were performed up to and including the 6<sup>th</sup> generation of ‘daughter cells’ and concentrations of  $n = 1, 2, 4, 8, 16, 32,$  and  $64$  magnetic dipoles per ROI were studied. The magnetic sphere’s magnetization was adapted accordingly for each generation of daughter cells under investigation.

## 4.4 Numerical simulations

### 4.4.1 Magnetic dipole field

The magnetic dipole field distribution is displayed in Fig. 4.3 and Fig. 4.4. In dependence on the orientation of the point of view with respect to  $\vec{B}_0$ , this dipolar field induces both areas in which the external homogeneous magnetic field is diminished (i.e., the equator) and areas in which it is enhanced (i.e., the poles).

### 4.4.2 Magnetic field distortion around magnetically labeled cells

The magnetic field distortions simulated for specific geometries of magnetic particles are depicted in Fig. 4.7. The magnetic field around a magnetic sphere with the same total magnetic moment is also shown. Within the spherical arrangement of particles considered ( $r < \tilde{a}$ ), differences in the magnetic field distortions were found. Outside the cell ( $r > \tilde{a}$ ), the field distortion was that of a single magnetic dipole.

The induced magnetic fields were compared to the magnetic field around a spherical particle with the same magnetic moment. The relative field difference  $\Delta$  was a function of the distance with respect to the dipole geometry with radius  $\tilde{a}$  and converged towards zero for increasing

distances. The values of  $\delta B_z$  as well as of  $\Delta$  were evaluated in the plane-of-view for directions parallel and perpendicular to the vector of the main magnetic field  $\vec{B}_0$ . Close to the particle geometries ( $r > \tilde{a}$ ) the field difference was  $\Delta < 0$ , and the magnitude of the magnetic field distortion  $|\delta B_z^{\text{particles}}|$  was higher than those of the magnetic reference sphere  $|\delta B_z^{\text{sphere}}|$  for the same distance.

The distances  $d$  from the cell surface for which the magnitude of the relative field difference was found to  $\Delta = 25\%$ ,  $\Delta = 10\%$ , and  $\Delta = 5\%$ , respectively, are given in Table 4.2 for orientations parallel and perpendicular to the vector  $\vec{B}_0$ . The distances are specified in units of cell radius  $\tilde{a}$ . At the same distance to the cell, the highest values of field difference  $\Delta$  were found for magnetic particles located at the cell's surface.

**Table 4.2** Distances  $d$  from the cell surface for which the magnitude of the relative field difference was found to  $\Delta = 25\%$ ,  $\Delta = 10\%$ , and  $\Delta = 5\%$ . The distances are specified in units of cell radius  $\tilde{a}$ .

model	parallel $B_0$			perpendicular $B_0$		
	$d(\Delta=25\%)$ [ $\tilde{a}$ ]	$d(\Delta=10\%)$ [ $\tilde{a}$ ]	$d(\Delta=5\%)$ [ $\tilde{a}$ ]	$d(\Delta=25\%)$ [ $\tilde{a}$ ]	$d(\Delta=10\%)$ [ $\tilde{a}$ ]	$d(\Delta=5\%)$ [ $\tilde{a}$ ]
$a_1$	0.7	1.7	2.8	0.7	1.7	2.8
$a_2$	0.7	1.7	2.8	0.7	1.7	2.8
$b_1$	0.3	$\Delta = 0$ for $d > 0.3$		$\Delta = 0$ for $d \geq 0$		
$b_2$	0.3	$\Delta = 0$ for $d > 0.3$		$\Delta = 0$ for $d \geq 0$		
$c$	1.1	2.3	3.9	0.7	2.1	3.8

The frequency distributions  $p(\nu)$  computed in the plane-of-view and the static signal decay curves are shown in Fig. 4.8. For all dipole geometries no significant differences in the computed frequency distributions were found for the chosen simulation conditions and modelling parameters. However, non-Lorentzian frequency distributions were revealed. Thus, the calculated signal decay curves showed non-monoexponential characteristics.

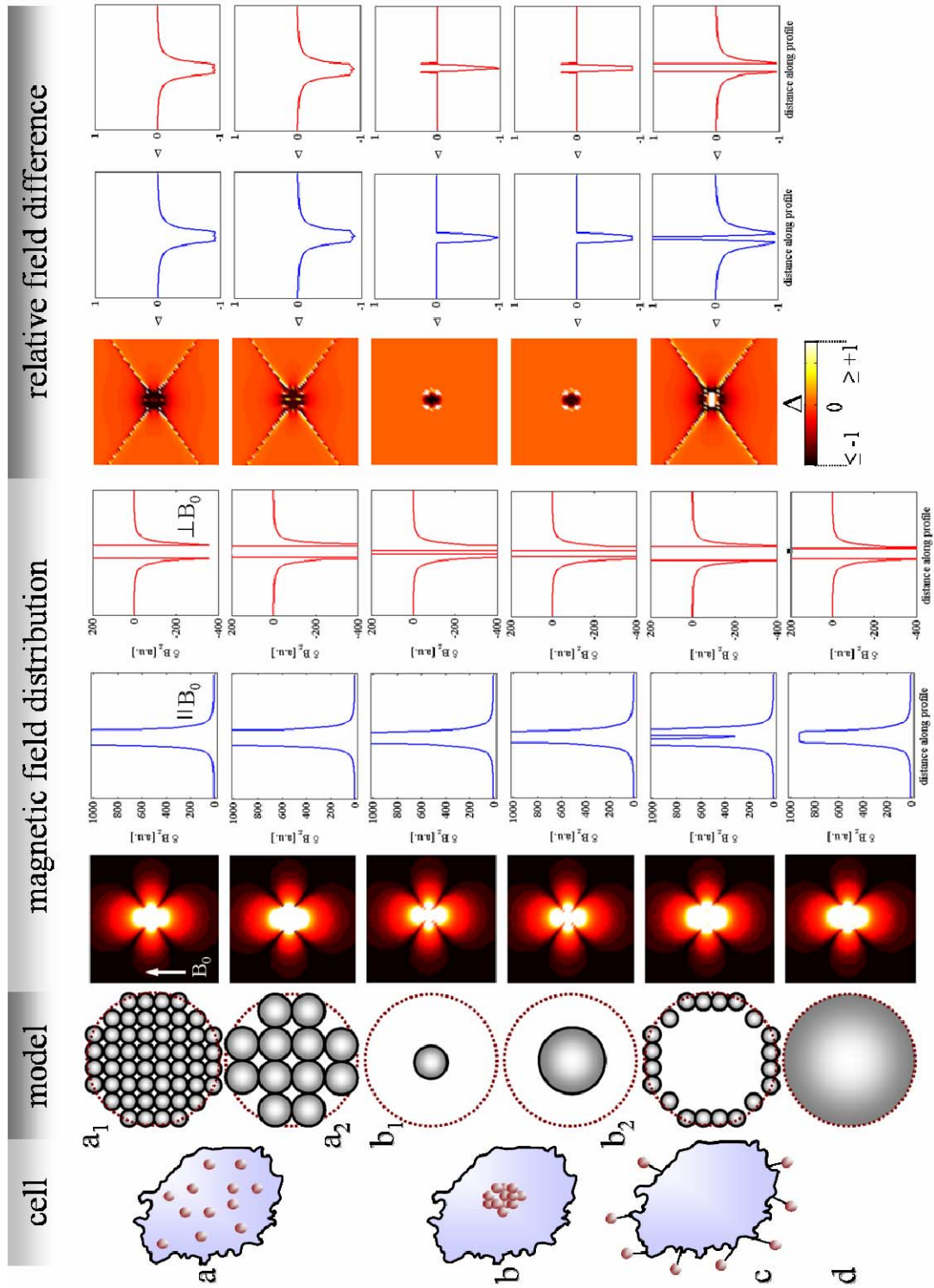


**Figure 4.7** Magnetic field distributions computed for various geometries of magnetic particles. The magnetic field is displayed color-encoded and is evaluated for directions parallel and perpendicular to the vector of the main magnetic field  $\vec{B}_0$ . The computed magnetic field was compared to the field induced by a magnetic reference sphere with the same magnetic moment. The ‘relative field differences’ were evaluated on a voxel-by-voxel basis.

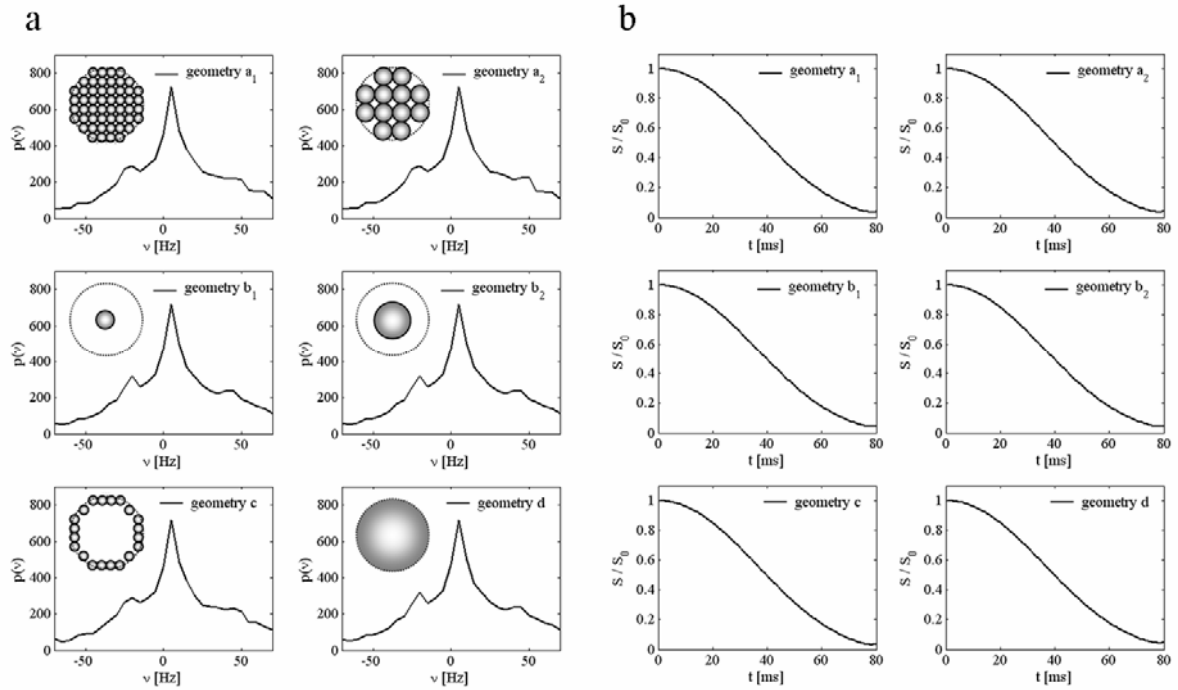


**Figure 4.8** (a) Frequency distributions  $p(\nu)$  of resonance frequencies  $\nu$  in the plane-of-view. (b) The respective static signal decay curves were obtained by Fourier transforming  $p(\nu)$ .

#### 4.4.3 Effect of spatial distribution of magnetic material

The frequency distributions computed for a constant volume fraction of magnetic material, but for an increasing number of randomly distributed magnetic dipoles are given in Fig. 4.9a. Note that representative examples of the computed frequency distribution and the calculated signal decay are shown. For a small number of cell clusters ( $n_d \leq 64$ ), the calculated frequency distribution was neither symmetrical with respect to  $\delta\nu = 0$  nor Lorentzian distributed. Furthermore, the maximum of frequency distribution was shifted towards positive frequencies.

The related signal decay curves are displayed in Fig. 4.9b. Fourier transforming these frequency distributions led to non-monoexponential signal decay curves for  $n_d \leq 64$ . In increasing the number of dipoles, two observations were made: Firstly, a spectral broadening and hence faster signal decay, and secondly, a more symmetrical frequency distribution, which was found to be Lorentzian distributed with respect to  $\delta\nu = 0$  Hz. In that case, monoexponential signal decay was found.

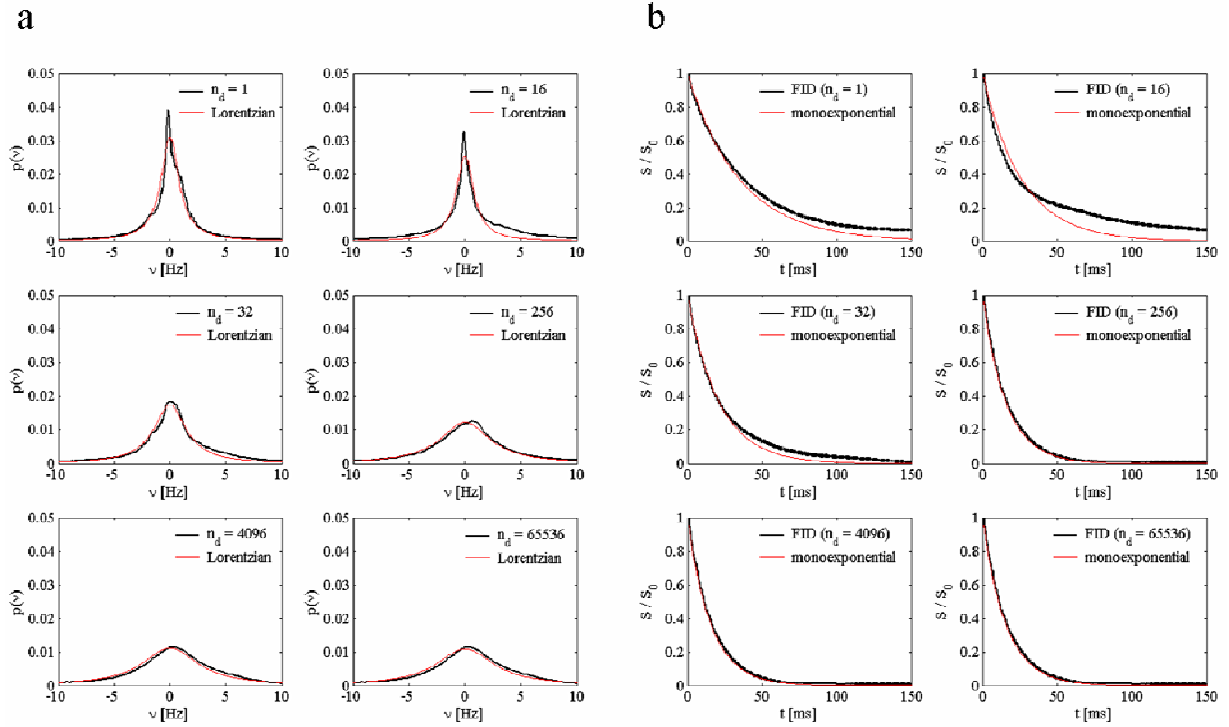


**Figure 4.9** (a) Spectral distribution of resonance frequencies, computed for a constant volume fraction (0.01 %) of magnetic material but a different number  $n_d$  of magnetic dipoles, which were distributed randomly throughout the ‘simulation universe’. (b) Related signal decay curves. Lorentzian functions were fitted to the computed frequency distributions, whereas monoexponential functions were fitted to the calculated signal decays. Highly clustered magnetic dipoles (magnetically labeled cells) caused non-Lorentzian frequency distributions. This resulted in non-monoexponential signal decay.

In addition, the division of magnetically labeled cells was simulated and the changes in the magnetic field distribution were pointed out. The 3d frequency distribution computed for increasing concentrations of daughter cells (i.e., less magnetized dipoles) is given in Fig. 4.10, together with the respective signal decay curves.

Representative examples (cell number  $n = 1, 4, 16,$  and  $64$ ) of the frequency distribution and the static signal decay are depicted. In increasing the number of magnetic dipoles and sharing a constant total magnetic moment among these dipoles, two main observations were made: Firstly, a spectral broadening and hence faster signal decay, and secondly, the tendency towards Lorentzian frequency distribution and monoexponential signal decay.

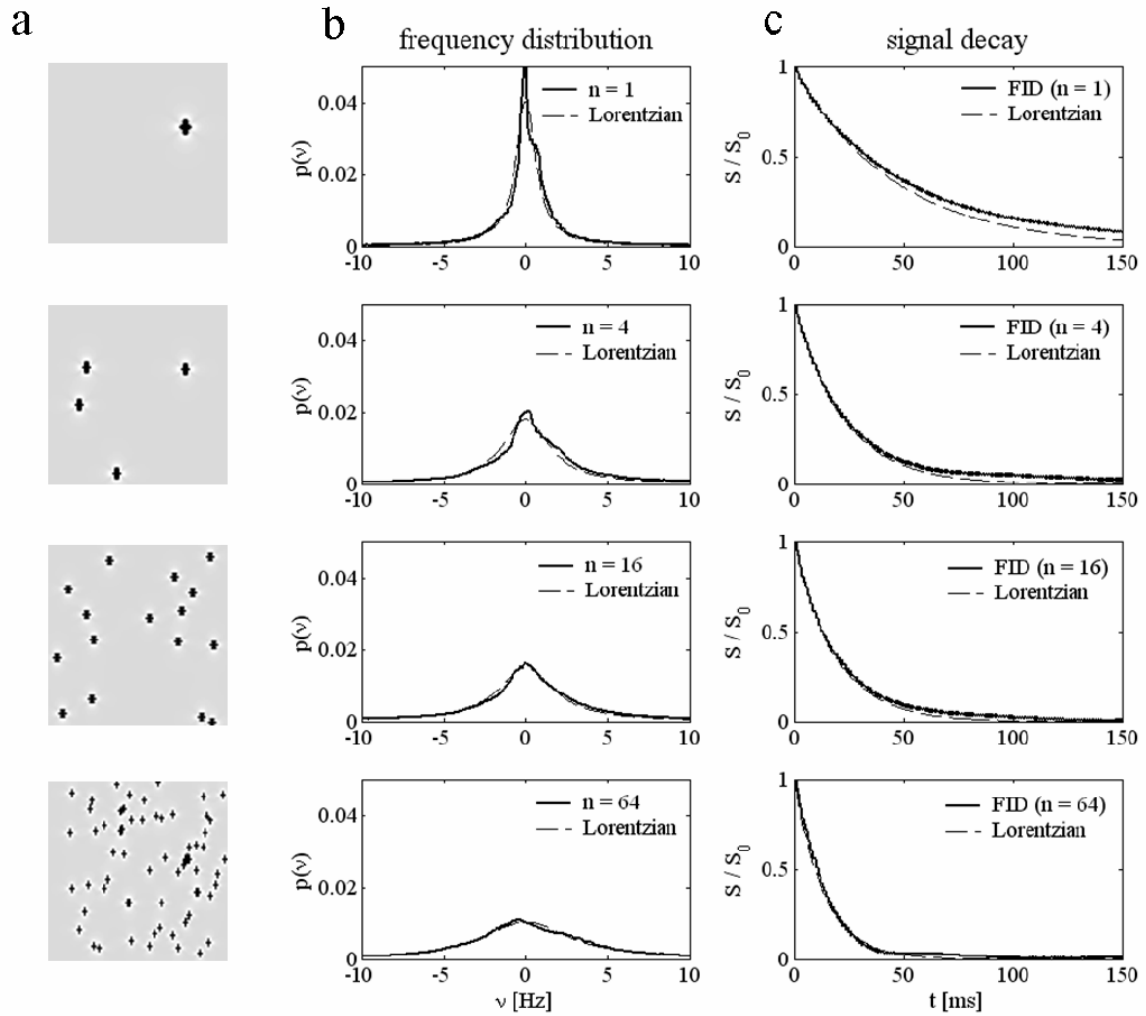


**Figure 4.10** Effects on frequency distribution and static signal decay corresponding to the division of magnetically labeled cells. Within the model, due to cell division, the magnetic moment  $p_m$  of the parent cell ( $n=1$ ) is allocated to an increasing number  $n$  of identical but less magnetized daughter cells. (a) cross section through the magnetic field distribution in the ROI, (b) resonance frequency distribution, (c) static signal decay.

## 4.5 Interpretation of the results

### 4.5.1 Magnetic field distortion around magnetically labeled cells

The key finding was that the magnetic field distortion created by any SPIO loaded cell is sensitive to its shape and intracellular distribution of magnetic moments only in close proximity to the cell. It was demonstrated that outside this region the magnetic field cannot be distinguished from the field inhomogeneities created by a spherical particle with the same total magnetic moment. This magnetic moment depends on the number of intracellular SPIO particles, whereas the cell's 'effective magnetization' accounts for the density of the particles per volume of cell. Saturation effects of the SPIO magnetization at clinically field strengths should be taken into consideration [Kal00].

Under the conditions of the static dephasing regime, the signal obtained from within an imaging voxel is affected by the intravoxel magnetic field distribution and the respective distribution  $p(\nu)$  of resonance frequencies. Several approaches to calculate transverse relaxation for certain  $p(\nu)$  characteristics have been developed [Bow02, Yab94, Zie05a, Zie05b, Bau99, Kis99]. Ziener et al. [Zie05a] investigated transverse relaxation of a cell labeled with magnetic nanoparticles by taking into account the magnetic dipole field around the labeled cell, which was treated as a magnetic sphere. In the present study, several geometries of intracellular distribution of magnetic moments were studied and their effects on the extracellular magnetic field inhomogeneities were scrutinized. As based on the findings of this study, it is anticipated that the field distortions caused by magnetic spheres characterize the magnetic field around iron oxide loaded cells precisely, providing the volume fraction of labeled cells per imaging voxel is sufficiently small.

No significant differences in the frequency distribution  $p(\nu)$  computed in the plane-of-view were found. For all dipole geometries, non-Lorentzian probability distributions  $p(\nu)$  were revealed. Furthermore, the simulation of  $p(\nu)$  was in good agreement with the results of Cheng et al. [Che01] and Seppenwoolde et al. [Sep05], who reported the spectral characteristics due to various spatial distributions of magnetic susceptibility including spherical magnetic objects. As a result of the non-Lorentzian frequency distribution, the calculated static signal decay was non-monoexponential.

In practice, cells are labeled with a very large number of SPIO particles (up to  $10^5$  in each cell). For moderate iron loads, no adverse side effects to the labeled cell population have been reported so far. In the current study, such high numbers of particles were not taken into account. This was no major limitation since it was revealed that far from the labeled cell, where the magnetic field inhomogeneity effects are most effective, the magnetic field distribution is determined by the cell's 'effective magnetic moment' rather than the number of particles that carry this moment.

It was demonstrated further that in case of small volume fractions of labeled cells per imaging voxel the majority of tissue molecules will experience only the magnetic dipole field outside the SPIO labeled cell. This assumption is anticipated to be valid for iron loaded liver Kupffer cells, which comprise only about 2-4 % of the mass of the liver [Har89]. For higher volume fractions of labeled cells this assumption is less certain, and the magnetic field distribution and the respective MR signal formation are likely a function of the intracellular SPIO distribution. For example, assuming an isotropic imaging voxel of 0.1 mm side length, a single labeled cell (diameter 50  $\mu\text{m}$ ) occupies 6.5 % of the volume of this voxel. It is reasonable to assume, that for higher volume fractions of labeled cells, the intravoxel field and frequency distributions are more complex as compared to a magnetic sphere and strongly depend on the intracellular SPIO distribution.

#### 4.5.2 Effect of spatial distribution of magnetic material

Under static dephasing conditions, the gradient echo signal decay reflects the local frequency distribution. In the present work, the effect of the spatial distribution of magnetic material on the Larmor frequency distribution was studied. The field superposition effects of neighboring dipoles were taken into account. The key finding of the study was that the spatial distribution of magnetic material such as magnetically labeled cells is an important factor that determines the resonance frequency distribution and the static MR signal decay.

As discussed above, the magnetic dipole field has shown to be an appropriate model for the field distortion around SPIO loaded cells. While the actual field close to the cell will certainly be very different from that of a magnetic dipole, far from the cell where the field inhomogeneity effects are most effective, the field distribution will closely resemble that of a magnetic dipole.



Diffusion effects were neglected and only the static frequency distribution was computed. This was supposed to be a reasonable approach as the large magnetic moment of SPIO loaded cells produces a strong enough dipolar field around the cell such that spin diffusion has a minimal effect on the MR signal decay. In fact, Bowen et al. [Bow02] have found SPIO loaded cells to satisfy the predictions of the static dephasing regime developed by Yablonskiy and Haacke [Yab94]. However, even for SPIO loaded cells, spin diffusion cannot always be neglected [Gil02]. If  $R$  is the cell radius (supposed to be a sphere) diffusion is negligible only if the diffusion time, i.e.  $R^2/D$ , is larger than  $0.81 / (\gamma \cdot M)$  in Gaussian units, with  $\gamma$  the proton gyromagnetic ratio and  $M$  the cells magnetization. It is reasonable to assume, that this inequality could be satisfied for highly magnetized cells [Bow02], but could also be dissatisfied for extremely weakly magnetized cells.

The strong dependence of the frequency distribution on the spatial distribution of magnetic dipoles is likely to be of critical importance in optimizing and interpreting the results of iron-oxide contrast agents targeted to cells such as liver Kupffer cells [Wang01]. In fact, deviation from monoexponential signal decay in liver tissue has been observed following the intravenous injection of iron oxide nanoparticles, which turned into faster and monoexponential signal decay post injection. Briley-Saebo et al. [Bri04] have shown that iron oxide nanoparticles were taken up in liver Kupffer cells following injection, whereas liver hepatocytes did not take up the injected iron oxide particles. In the same study, light-microscopic studies did, however, indicate an increased iron load, presumably as ferritin/hemosiderin (i.e., liver iron storage proteins) within the hepatocytes 24 h post injection. Moreover, non-monoexponential signal decay has been observed in patients with liver iron overload; with the excess iron primarily accumulated in liver Kupffer cells [Jen02].

According to the histological findings and the results of the present work, one can suppose that the non-monoexponential signal decay observed in liver tissue following SPIO injection and iron overload, respectively, is likely to be associated with iron clustering in the liver Kupffer cells. However, using tissue compartment models, as predicted by Bulte et al. [Bul97] and investigated in vitro by Tanimoto et al. [Tan01], these observations cannot be explained satisfactorily. Thomsen et al. [Thom92] found that the relative amplitudes of the two terms of a bi-exponential fit varied significantly with the iron concentration, implying that the terms cannot be clearly associated with specific tissue structures. This is a major ar-

gument against the explanation of non-monoexponential signal decay in the iron loaded liver using tissue compartment models.

In the present work it was demonstrated numerically that this non-monoexponential signal decay is likely to be a direct consequence of the magnetic dipole clusters in presence of the SPIO accumulation within liver Kupffer cells and the associated strong magnetic field inhomogeneities.

Stem cells have shown to maintain their proliferation capacity and differentiation outcome even after labeling with iron oxide nanoparticles (10 – 30 pg Fe / cell) [Arb05]. Assume that labeled cells with a specific iron load were injected for therapy. If we want to track these cells and cell division occurs, in the first generation, we would have twice the cells (daughter cells) with half the SPIO load per cell (mother cell). In the current study the changes in the Larmor frequency distribution and signal decay characteristics due to division of iron loaded cells were scrutinized using a numerical model. Cell division was modelled by sharing a constant magnetic moment (mother cell) among an increasing number of less magnetized magnetic dipoles (daughter cells). As based on the numerical results, the possible outcomes of cell division are likely a local alteration in the magnetic field distribution and the corresponding transition from non-monoexponential to monoexponential signal decay, while the signal decay is accelerated.

## Chapter 5

# Macroscopic extracellular magnetic field inhomogeneities

### 5.1 Physical and biological background

Cellular imaging by means of Magnetic Resonance Imaging (MRI) has become very attractive since it provides anatomical, functional, and biochemical information as well as excellent image quality. Due to its limited spatial resolution, MRI is in fact not capable of visualizing single cells. However, cells labeled with superparamagnetic iron oxide (SPIO) particles cause intense magnetic field distortions over fairly large distances. Thus, SPIO labeled cells become detectable due to their significant effects on MRI signal dephasing induced in water molecules near the cells [Yab94, Zie05a].

The ability of MRI to visualize aggregations of thousands to millions SPIO labeled cells has attracted much attention in the past few years [Dal03, Him04, Hoe02, Jen03]. Aggregations of cells labeled with SPIO are reflected either as low-intensity signal spots or signal voids, particularly in  $T_2^*$ -weighted gradient echo MRI. It is important to know that localized MR signal loss can be also attributed to tissue-specific magnetic field inhomogeneities, mimicking the appearance of labeled cells under in vivo conditions. In order to separate both effects, it is of critical importance to understand the physical basis as well as the effects of sequence parameters on the signal voids in MRI induced by aggregations of magnetically labeled cells.

The aim of the current work was to achieve a profound understanding of signal voids in static dephasing MRI caused by spherical aggregations of SPIO loaded cells by means of numerical simulations and MR measurements. A preparation technique for the ex vivo examination of SPIO containing solutions and SPIO labeled cells was developed. The effects of fundamental variables on the signal dephasing close to cell cluster were investigated systematically: Firstly, variables attributed to the aggregation of SPIO labeled cells including their spatial distribution and the concentration of labeled cells as well as the iron label per cell were studied. Secondly, geometry and extension of the image signal voids were examined in dependence on elementary sequence parameters including echo time, voxel size, and orientation of the plane of view (i.e., the image orientation) with respect to the main field  $\vec{B}_0$ . The first parameters are relevant for the SPIO induced magnetic field inhomogeneities, whereas the latter parameters define how these field inhomogeneities affect the MR image.

## 5.2 Materials and methods

### 5.2.1 Numerical simulations

#### General considerations

MRI signal voids may be attributed to both, signal dephasing in voxels containing labeled cells (i.e., microscopic effects) and signal dephasing near cell aggregations (i.e., macroscopic effects). Studying geometry and extension of signal voids with respect to magnetization and sequence parameters demanded for modelling of the macroscopic magnetic field inhomogeneities around cell cluster.

In the current study, a cluster of labeled cells was considered as a homogeneous magnetic sphere, and the field distortion was assumed to be equivalent to that caused by a magnetic dipole with the same total magnetic moment. The size of the cell aggregation was presumed to extend over several imaging voxels. Recent studies have shown that labeled cells can aggregate in spherical cluster [Dal03, Jen03, Pint05a] and, hence, the present restriction to spherical geometries is anticipated to be no major limitation. A homogeneous distribution of labeled cells throughout the spherical volume was assumed.

Effects of cell concentration and iron load per cell were studied in terms of magnetization (i.e., the volume density of magnetic moments). To account for the huge spread in cell concentration (up to  $10^5$  cells/ $\mu\text{l}$ ) as well as in cell iron label (1-100 pg Fe/cell; [Bul04, Heyn06]), the signal voids due to aggregations of labeled cells were studied in an appropriate wide range of magnetization.

For each imaging voxel within the volume around a cell cluster, the respective phase gradient  $\delta\phi$  depends linearly on both the intravoxel magnetic field gradient  $\delta B_z$  and the echo time TE according to  $\delta\phi \propto \text{TE} \cdot \delta B_z$ . The considerations were limited to linear field gradients and linear phase gradients across the imaging voxel. This was no major restriction since for aggregations of labeled cells the voxel size is small compared to the extension of the magnetic field perturbation.

Intravoxel signal dephasing is affected by the geometry and the size of the imaging voxel. For the sake of simplicity, isotropic volume elements were assumed. Although the magnetic dipole field is symmetric with respect to rotation about the z-axis (i.e., the axis of the main magnetic field  $\vec{B}_0$ ), the magnetic field distribution in the plane of view depends on the angle of this plane relative to  $\vec{B}_0$ . This implies that the plane of view orientation also affects the observable signal void.

## Magnetic dipole field

The magnetic field distortions around spherical cell aggregations were treated as those of a magnetic dipole (Fig. 5.1). Note that a more detailed discussion of the respective magnetic field distortions is given in chapter 4. In order to model different concentrations of labeled cells as well as different iron loads per cell, the magnetic moment  $p_m$  was varied and the respective dipole field was computed.

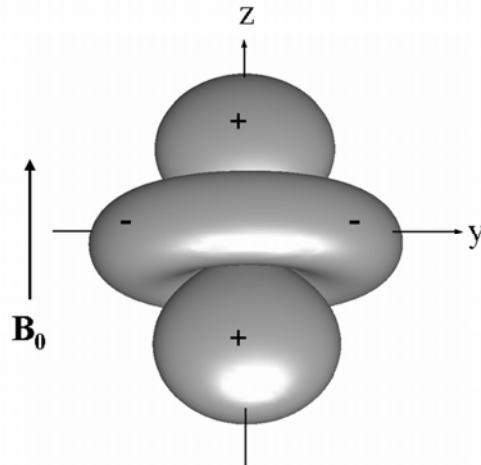


**Figure 5.1** Geometry of the field perturbation induced by a magnetic dipole in a homogeneous external magnetic field  $\vec{B}_0 = B_0 \cdot \vec{e}_z$ . Iso-surfaces of the 3d magnetic field distribution are shown. The external magnetic field is enhanced (+) or weakened (-) in a direction parallel ( $\vec{e}_z$ ) or perpendicular ( $\vec{e}_x, \vec{e}_y$ ) to  $\vec{B}_0$ .

## Numerical model

By means of a 3d numerical model, geometry and extension of the MRI signal void were studied in dependence on magnetization, echo time, voxel size, and orientation of the plane of view with respect to the main field  $\vec{B}_0$ . Briefly, the field distortion of a magnetic dipole in a homogeneous main magnetic field  $\vec{B}_0$  was computed. The magnetic dipole was placed in the center of the ‘simulation universe’, which was discretized to identical computational units. To reproduce isotropic voxel side lengths commonly selected for cellular MRI the side length of the computational units was varied from 0.1  $\mu\text{m}$  to 0.4  $\mu\text{m}$ . The magnetic moment of the dipole was varied. The field perturbation  $\delta B_z$  induced by the magnetic dipole was computed for each computational unit within the ‘simulation universe’.

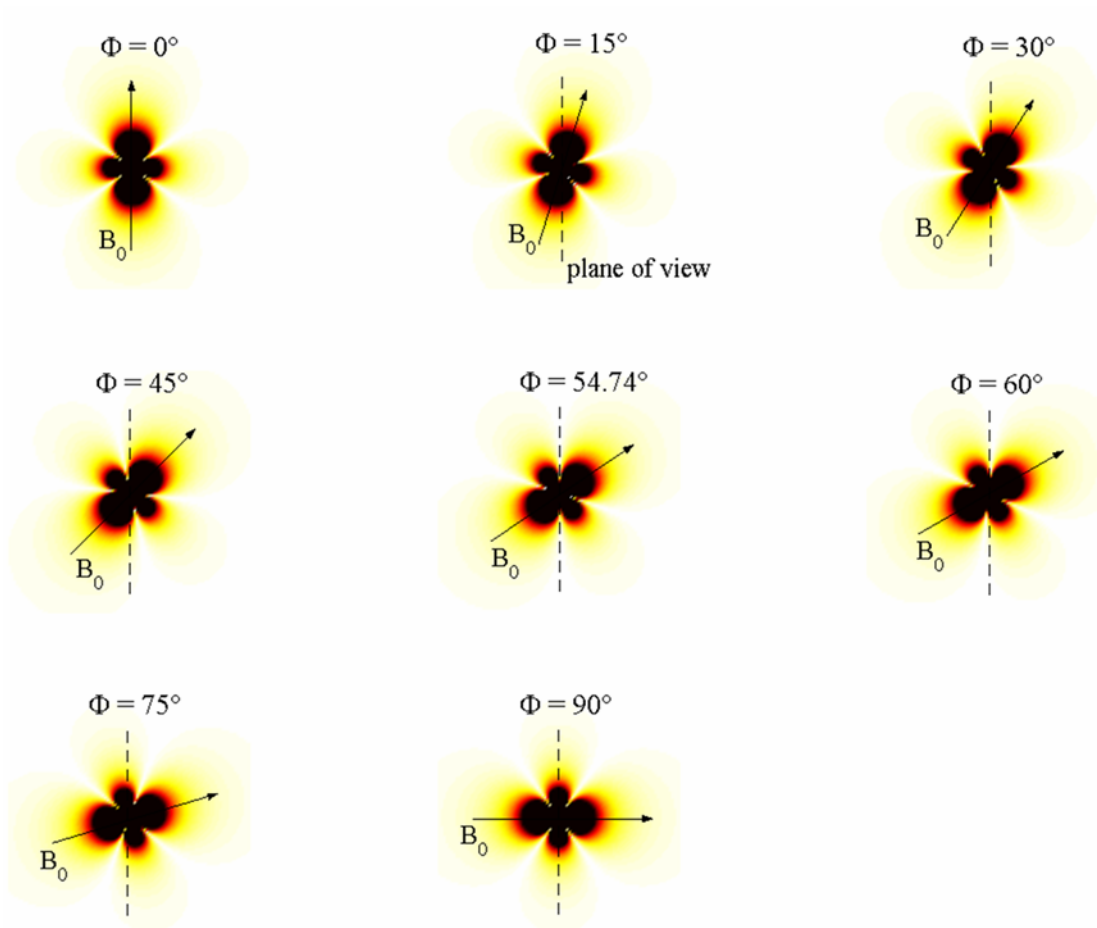


**Figure 5.2** By rotating the plane of view (dashed line) with respect to the external  $\vec{B}_0$  field, the geometry and the extension of the signal voids in this plane of view were studied. The normal vector of the plane of view points parallel to the image plane. The angle  $\Phi$  describes the orientation of the plane of view with respect to the external magnetic field vector.

Signal dephasing due to magnetically labeled cells is attributed to the intensity of the magnetic field inhomogeneities and the strength of diffusion of water molecules through these field inhomogeneities. As pointed out in chapter 2, diffusion effects become negligible in case of intense magnetic field distortions and large magnetic perturbers (i.e., diffusion correlation frequency  $\ll$  frequency dispersion due to magnetic field inhomogeneities). As confirmed by Bowen et al. [Bow02] these static dephasing conditions are well satisfied for aggregations of magnetically labelled cells, thus enabling to find a relationship between field distortions and static signal dephasing in gradient echo MRI.

The simulations were performed under static dephasing conditions for which the position of each computational unit was fixed with respect to the 3d volume grid. The program code

permitted choosing the plane of view (as a cross section through the 3d volume grid) arbitrarily. The orientation of the plane of view was varied with respect to the xz-plane. As displayed in Fig. 5.2, the plane of view was rotated around the x-axis with well-defined settings of the angle  $\Phi$ .

### Computation of signal void

The computed 3d magnetic field distributions were postprocessed by a home-built code written in MatLab<sup>®</sup> (Version 6.5, The Mathworks, Natick MA, USA). The computational units were treated as imaging voxels in this regard. At a given intensity of the magnetic field gradient per imaging voxel, the respective phase gradient is

$$\delta\phi = \gamma \cdot TE \cdot \delta B_z, \quad (5.1)$$

with  $\gamma$  proton gyromagnetic ratio and TE the echo time.

Kingsley [King95] recognized that a complete intravoxel signal dephasing requires at least a linear phase gradient  $\delta\phi \geq 2\pi$  parallel to one side of an isotropic imaging voxel. In the present model, the area of signal void in the plane of view was presumed to comprise all computational units for which the dephasing condition  $\delta\phi - 2\pi \geq 0$  was satisfied.

The plane of view was rotated stepwise about the x-axis within an angular range of  $0^\circ \leq \Phi \leq 90^\circ$ . For each orientation, the phase gradient was calculated on a voxel-by-voxel basis and was evaluated for orthogonal directions denoted  $a_{yz}$  and  $a_x$  as specified in the plane of view. The dashed vertical line in Fig. 5.2, labeled as the plane of view, corresponds to the y-z axis denoted  $a_{yz}$  in Fig. 5.6. The direction  $a_{yz}$  accounts for the extension of the computed signal void in the yz-plane, whereas the  $a_x$ -direction specifies the extension of the signal void along the x-axis.

### Dependence of signal void on magnetization

The extension of the signal void was determined in dependence on the magnetization M of a spherical particle respectively the magnetic moment  $p_m$  of the dipole, which is by definition the product between the sphere's magnetization and the volume to read



$$p_m = M \cdot (4/3) \cdot \pi \cdot a_d^3. \quad (5.2)$$

All simulations considered spherical cell aggregations with constant radius  $a_d = 500 \mu\text{m}$  and diameter  $D_0 = 1.0 \text{ mm}$ . This physical extension reflected experimental conditions adequately [Hoe02, Him04, Pint05a].

To account for the spread in both the local cell concentration and the average iron label per cell, the value of  $M$  was varied logarithmically in a domain ranging from  $5 \mu\text{T}$  to  $20,480 \mu\text{T}$ . The extension of the signal void was evaluated for an isotropic voxel size of  $100 \mu\text{m}$ , an echo time  $TE = 20 \text{ ms}$ , and plane of view orientations within the angular range of  $0^\circ \leq \Phi \leq 90^\circ$ .

### Dependence of signal void on plane of view orientation

The magnetic field in the plane of view depends on the angle  $\Phi$  of this particular plane relative to the main field  $\vec{B}_0$ . Thus, the respective signal voids were anticipated to depend on this orientation. The magnetic field distribution was computed for various plane of view orientations (i.e.,  $\Phi = 0, 15, 30, 45, 54.74, 60, 75, \text{ and } 90^\circ$ ) as illustrated in Fig. 5.2. Due to the symmetry of the dipole field with respect to rotation about the  $z$ -axis as well as mirroring with respect to the  $xy$ -plane, the investigation of these orientation effects were confined to  $0^\circ \leq \Phi \leq 90^\circ$ . For these simulations, an isotropic voxel size of  $100 \mu\text{m}$  and  $TE = 20 \text{ ms}$  were selected. The magnetization was varied between  $5 \mu\text{T}$  and  $20,480 \mu\text{T}$ .

### Dependence of signal void on echo time

The intravoxel phase distribution within the spin ensemble is determined by the fundamental sequence parameter echo time  $TE$ . The value of  $TE$  was varied from  $5 \text{ ms}$  up to and including  $80 \text{ ms}$  in steps of  $5 \text{ ms}$ , and the geometry as well as the extension of the respective signal voids were scrutinized. Within the numerical simulations performed, isotropic voxel side lengths of  $100 \mu\text{m}$ , magnetizations  $M = 160 \mu\text{T}$ ,  $640 \mu\text{T}$ , and  $2,560 \mu\text{T}$ , as well as plane of view orientations parallel ( $\Phi = 0^\circ$ ) and perpendicular ( $\Phi = 90^\circ$ ) to the  $\vec{B}_0$  field were considered. In order to assess the relative changes in the diameter  $D$  of signal voids for echo times  $TE > 5 \text{ ms}$ , the ratio between  $D(TE)$  and  $D(TE = 5 \text{ ms})$  was calculated for each  $TE$  data point.

## Dependence of signal void on voxel size

The signal void characteristics were assessed in dependence on voxel size. Utilizing dedicated small-animal MRI scanners operating at high magnetic field strength facilitates high-resolution MR cellular imaging with 3d isotropic spatial resolutions up to 100  $\mu\text{m}$  [Heyn06, Sha06]. For numerical simulations, isotropic voxel sizes with side lengths  $R = 100 \mu\text{m}$ , 200  $\mu\text{m}$ , and 400  $\mu\text{m}$  were evaluated. The simulation parameters included magnetization values of  $M = 160 \mu\text{T}$ , 640  $\mu\text{T}$ , and 2,560  $\mu\text{T}$ , an echo time of  $TE = 20 \text{ ms}$ , and plane of view orientations  $\Phi = 0^\circ$  and  $\Phi = 90^\circ$  with respect to  $\vec{B}_0$ .

### 5.2.2 MR measurements

#### Preparation of the agar gel phantoms

Various concentrations of SPIO containing solutions and SPIO labeled cells were accommodated within an agar gel matrix. This was considered to provide the suitable homogeneous environment necessary for the measurement of the magnetic field inhomogeneity effects induced by aggregations of SPIO. An agar gel solution (1 %) was boiled and subsequently cooled down slowly in a water bath. This procedure minimized air bubble inclusions in the agar matrix, which lead to intense susceptibility gradients and magnetic field distortions, and mimic the appearance of SPIO in the MR image due to additional image artefacts. Before becoming stable the agar gel solution (200 ml) was embedded in non-ferromagnetic boxes. A series of identical cone shaped cavities was created in the agar matrix by means of a specially designed stamp (Fig. 5.3). Precise and careful handling of the stamp while impressing and removing was essential for the proper creation of cavities with well-defined geometry and size, and without damage to the surrounding homogeneous gel matrix.

Different concentrations of SPIO containing solutions and suspensions of magnetically labeled cells were investigated (Table 5.1). SK-Mel28 human melanoma cells were used as the cell model. The cells were labeled by means of incubation with SH U 555A (Schering AG, Berlin, Germany). The standard cell labeling protocol as described in chapter 3 was used. The iron concentration in the medium was 400  $\mu\text{g Fe / ml}$  and the incubation time was 48 h. The average iron concentration per cell was determined to 50  $\text{pg Fe / cell}$  by means of photometry.

Both, the SPIO solutions and the labeled cells, respectively, were mixed (1:1) with gelatine (concentration 8 %). A volume of 10  $\mu\text{l}$  of the final suspension was implanted into the cone shaped cavities within the agar matrix. After solidification of the gelatine, the hollows were closed with agar (1 %). The samples with the well defined spatial distribution of SPIO within the homogenous agar matrix were used for MR measurements.



**Figure 5.3** A series of cone shaped cavities was created in an agar gel matrix by means of a specially designed stamp. SPIO containing solutions and labeled cells were implanted into these cavities. This preparation strategy with a well-defined spatial distribution of magnetic material in an agar gel phantom produced reliable results of signal voids in MR examinations and appears clearly superior compared to set-ups with randomly distributed material in glass tubes. For MR measurement the boxes were placed in the dedicated transmit/receive wrist coil.

## MR measurements

The MR measurements were conducted on a clinical whole-body MR scanner operating at 3 Tesla (Magnetom Trio<sup>®</sup>, Siemens Medical Solutions, Erlangen, Germany). The dedicated wrist coil was used for radiofrequency excitation and signal acquisition. For MR imaging a gradient echo sequence with low flip angles was implemented (fast low angle shot, FLASH [Haa86]). The constant sequence parameters were: repetition time TR 35 ms, flip angle 20°, field of view 128×128 mm<sup>2</sup>, read out bandwidth 260 Hz / pixel. The isotropic in-plane resolution was varied between 0.25 mm and 0.6 mm (side length of voxel). Furthermore, the echo time TE was varied between 5 ms and 25 ms.

**Table 5.1** Concentrations of SPIO containing solutions and SPIO labeled cells in the agar gel matrix as used for MR measurements.

SPIO containing solutions			SPIO labeled cells	
iron concentration in solution		iron in matrix	cells in matrix	iron in matrix
[ $\mu\text{mol Fe/ml}$ ]	[mg Fe/ml]	[ $\mu\text{g Fe in } 10 \mu\text{l}$ ]	[ $\times 10^3$ in $10 \mu\text{l}$ ]	[ $\mu\text{g Fe in } 10 \mu\text{l}$ ]
26.79	1.5	15.0	1,000	50.0
17.86	1.0	10.0	800	40.0
13.39	0.75	7.5	600	30.0
8.93	0.5	5.0	500	25.0
5.36	0.3	3.0	400	20.0
3.57	0.2	2.0	300	15.0
2.68	0.15	1.5	200	10.0
2.23	0.125	1.25	150	7.5
1.79	0.1	1.0	100	5.0
1.34	0.075	0.75	75	3.75
			50	2.5
			25	1.25

### Extension of signal void

The diameter of image signal void along the  $\vec{B}_0$  field was assessed in dependence on the local iron concentration, the echo time and the in-plane spatial resolution. For this purpose, the signal intensities of each MR image were determined on a pixel-by-pixel basis using a home-built code written in MatLab<sup>®</sup> (Version 6.5, The Mathworks, Natick MA, USA). The diameter of signal void  $D$  was defined as full width half maximum (FWHM) (Fig. 5.4). Appropriate threshold values were selected in order to correct for image encoding artefacts in read out direction (parallel to  $B_0$ ). The dependence of the diameter  $D$  on the local iron concentration was assessed empirically using various types of mathematical functions including polynomial and logarithmic functions.

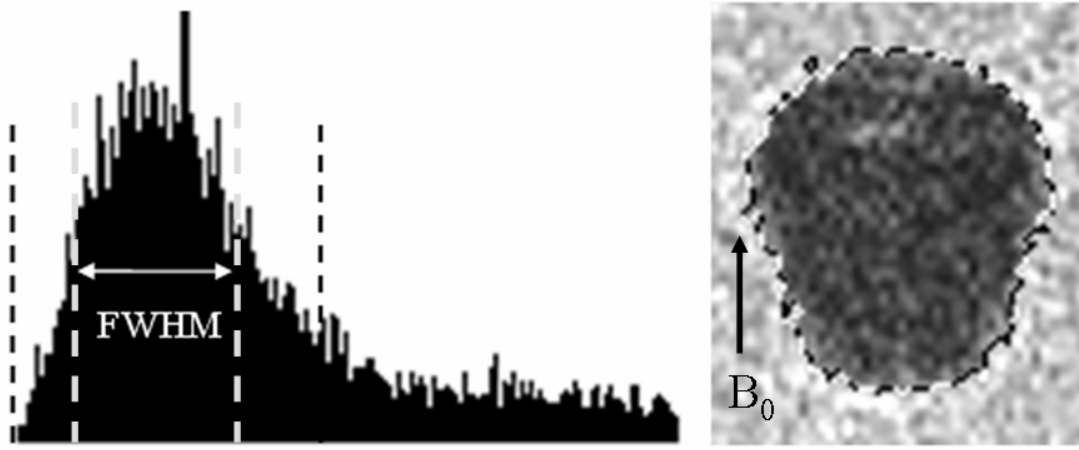


**Figure 5.4** The diameter of the MR image signal void in  $\vec{B}_0$  direction induced by aggregation of iron oxide loaded cells was defined as full width half maximum (FWHM). Appropriate threshold values were selected in order to correct for image encoding artefacts in read out direction (parallel to  $\vec{B}_0$ ).

## 5.3 Numerical and experimental results

### 5.3.1 Simulations on geometry and extension of signal voids in MR images

#### Dependence of signal void on magnetization

The dependence of the diameter of signal void  $D(M)$  on the magnetization  $M$  is displayed in Fig. 5.5. For both directions evaluated ( $a_{yz}$ ,  $a_x$ ; Fig. 5.6) the diameter of signal void rose with increasing magnetization. Relative enhancements in  $D(M)$  up to a factor of 9 as compared to the physical diameter  $D_0$  of the spherical aggregation were found. A non-linear dependency of  $D(M)$  on  $M$  was revealed: the higher the magnetization, the smaller the slope  $d(D(M)) / dM$ .

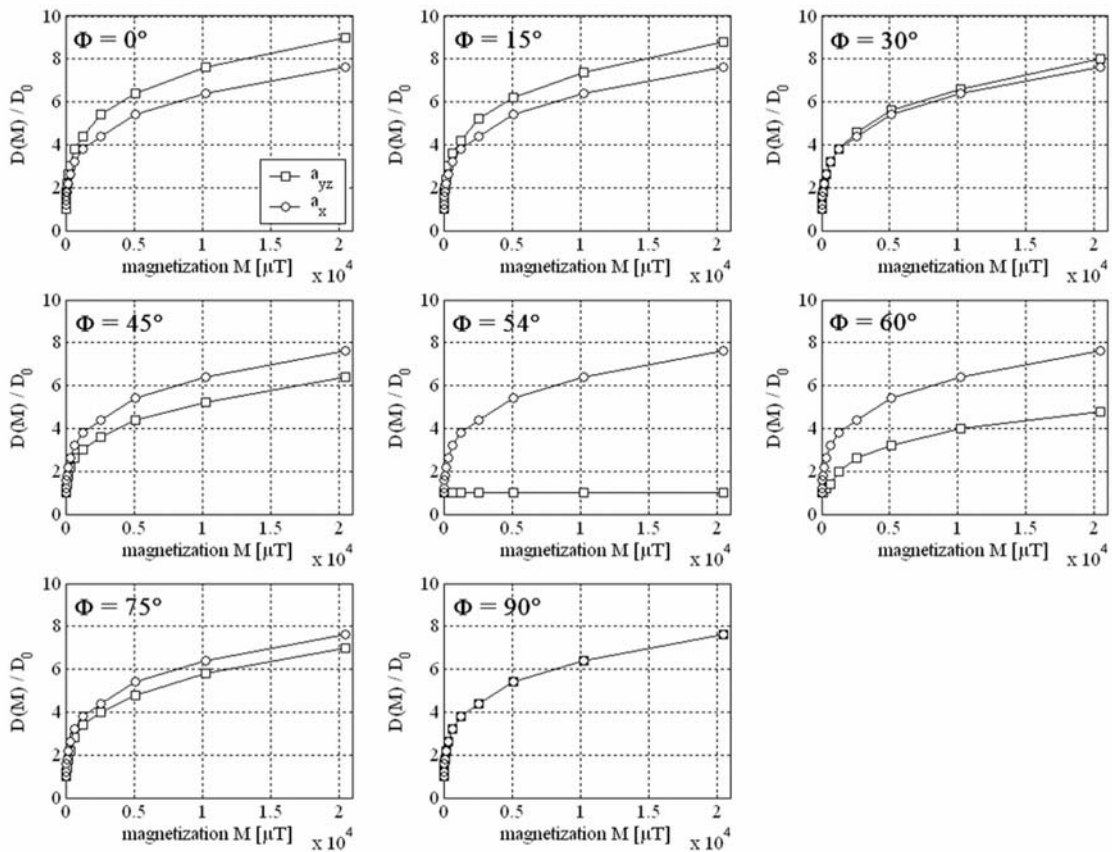


**Figure 5.5** Effects of cell concentration on the signal void in the plane of view were studied in terms of magnetization. For both directions evaluated ( $a_x$ ,  $a_{yz}$ ) the diameter of the image signal void  $D(M)$ , as compared to the physical diameter  $D_0$  of the spherical aggregation, increased with magnetization  $M$ . A non-linear dependency  $D(M)$  on  $M$  was demonstrated.

### Dependence of signal void on plane of view orientation

The orientation of the plane of view was varied with respect to  $\vec{B}_0$ , and the effects on geometry and extension of the signal void were studied. Representative geometries of the plane of view-dependent magnetic field distributions as well as respective signal voids are shown in Fig. 5.6. The signal void geometries as well as extensions exhibited a significant dependence on the orientation of the plane of view. Since the plane of view was rotated around the x axis, the diameter of the signal void along  $a_x$  direction was independent of their orientation. In contrast, the diameter of the signal void along the  $a_{yz}$  direction was a function of the orientation of the plane of view with respect to the external  $B_0$  field. For the “magic angle” of  $\Phi = 54.74^\circ$  the signal void in the  $a_{yz}$  direction was found to be  $D_0 = 1.0$  mm.

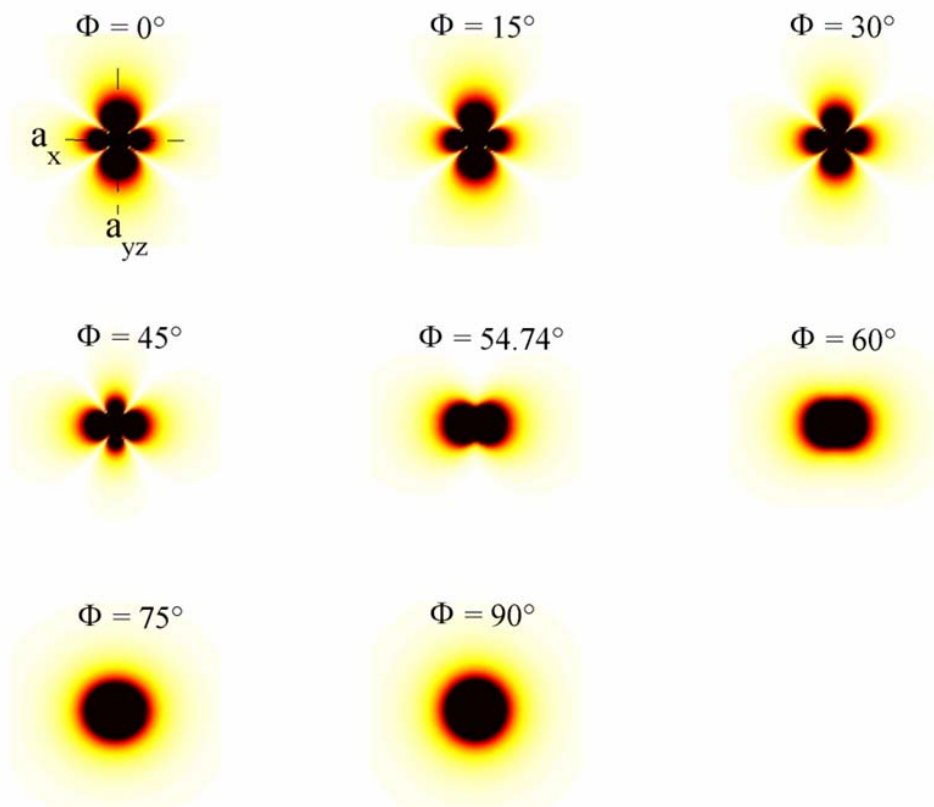


**Figure 5.6** The magnetic field distribution and the signal void geometries in the plane of view depend on the angle  $\Phi$  of the plane of view with respect to the main field  $\vec{B}_0$ . Cross sections through the computed 3d magnetic dipole field (color-encoded) and the respective signal voids (black) in the plane of view are depicted.

### Dependence of signal void on echo time

The diameter  $D(TE)$  of the signal void in the  $a_{yz}$  direction was evaluated for echo times in the interval  $5 \text{ ms} \leq TE \leq 80 \text{ ms}$ . As depicted in Fig. 5.7 the extension of signal void increased significantly with longer TE. Furthermore, a non-linear dependency of  $D(TE)$  on TE was demonstrated. The slope of the simulated data (i.e.,  $d(D(TE)) / dTE$ ) decreased for higher TE. The ratio  $D(TE) / D(TE = 5 \text{ ms})$  increased with TE. This ratio was found to be independent of magnetization.

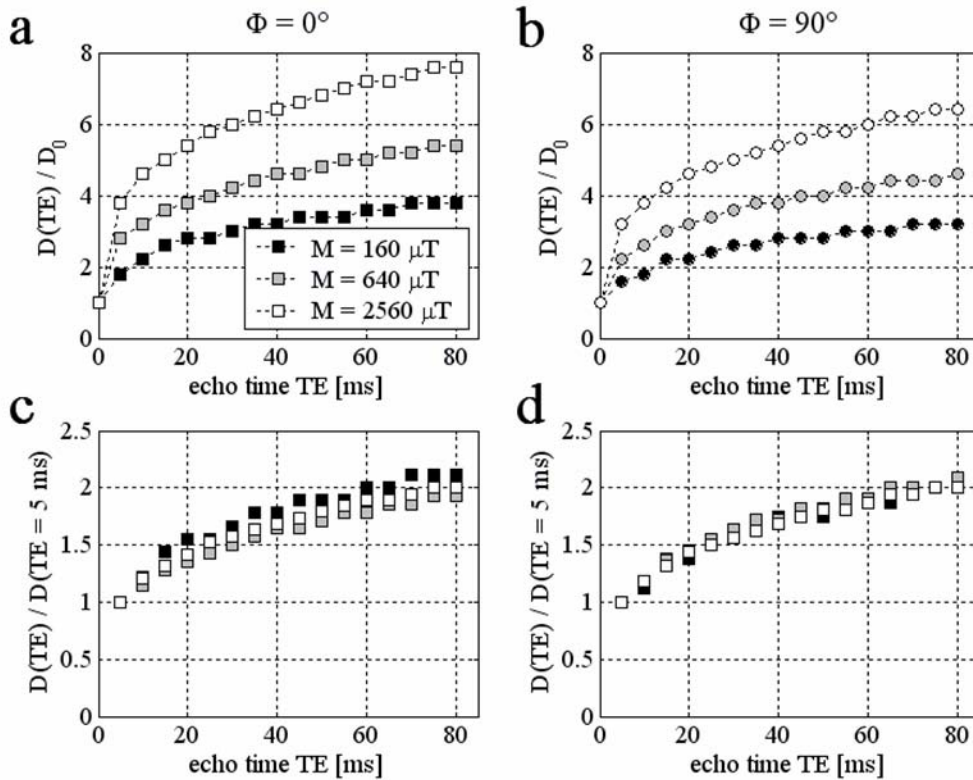


**Figure 5.7** (a, b) The diameter of the signal void in dependence on the echo time TE. (c, d) The ratio between  $D(TE)$  and  $D(TE = 5 \text{ ms})$  was calculated for each TE data point. This ratio was found to be independent of local magnetization.

### Dependence of signal void on voxel size

Finally, geometry and extension of signal void were computed for isotropic computational units scaled to  $R = 100 \mu\text{m}$ ,  $200 \mu\text{m}$ , and  $400 \mu\text{m}$ , respectively, in order to account for effects due to voxel size. The calculated values of  $D(R)$  in the  $a_{yz}$  direction are plotted against R in Fig. 5.8. For each sphere magnetization examined, the bigger the voxel size the larger the ex-



tension of the signal void. In general,  $D(R)$  was found to be several times larger than the physical diameter  $D_0$  of the magnetic sphere. In case of the plane of view orientation  $\Phi = 90^\circ$  with respect to  $\vec{B}_0$  these enhancement effects were less pronounced as compared to an orientation of  $\Phi = 0^\circ$ .

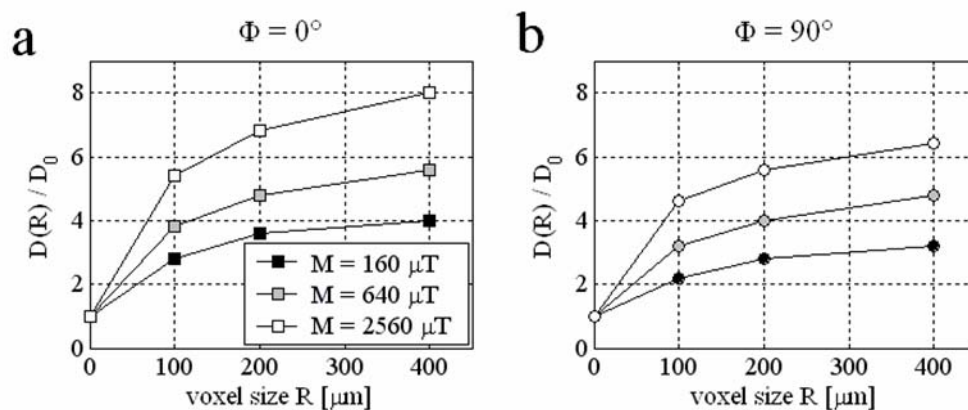


**Figure 5.8** The diameter  $D(R)$  of signal void in the plane of view in dependence on the voxel size  $R$ .

### 5.3.2 Quantitative investigation of SPIO containing solutions and SPIO labeled cells

#### Dependence of signal void on echo time and voxel size

Homogeneous agar gel samples with embedded SPIO containing solutions and SPIO labeled cells were used for MR measurements. Characteristic signal voids in the MR gradient echo images were observed for all samples examined. Representative image signal voids in dependence on echo time  $TE$  and voxel size are shown in Fig. 5.9.

The extension of signal void varied with echo time and in-plane spatial resolution (Fig. 5.10). For the present experimental conditions, the sensitivity to detect the magnetic label was maximized using  $TE = 25$  ms. In contrast, the area of signal void was minimized using  $TE = 5$  ms and an isotropic spatial resolution of 0.25 mm. In the latter case the image signal void indicated the area of magnetic material most precisely.

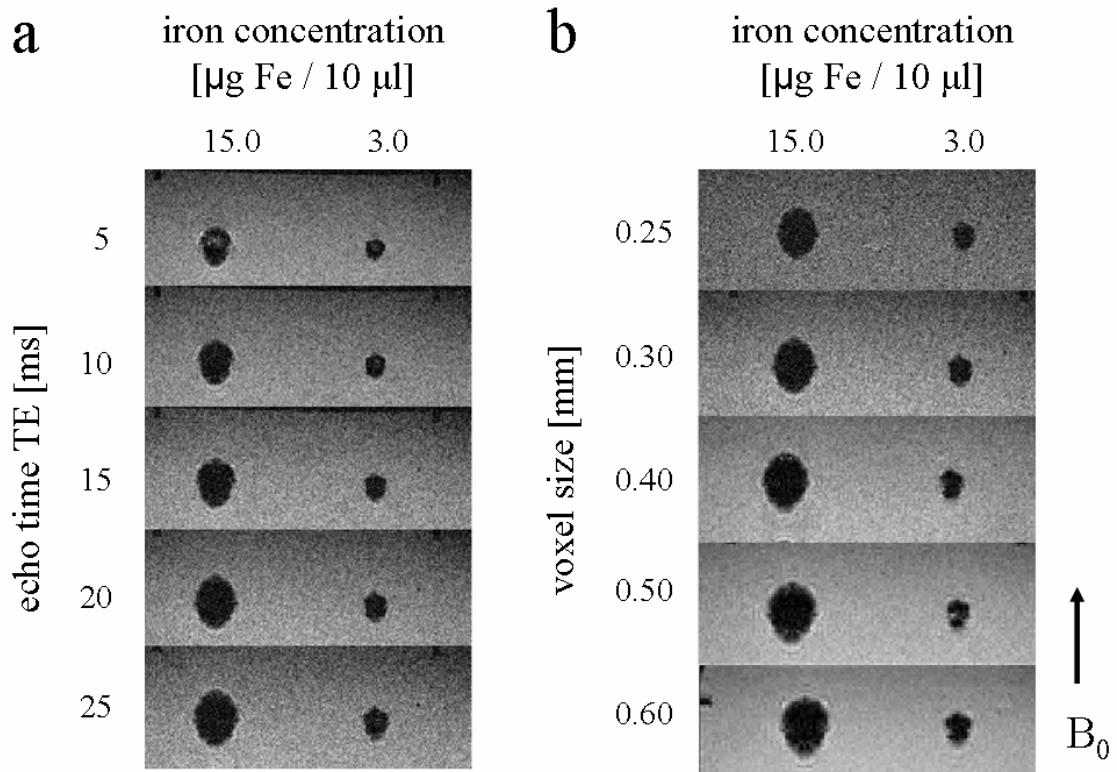


**Figure 5.9** Signal void in gradient echo MRI induced by local aggregations of iron oxide nanoparticles. The dependence of the image signal void on echo time (a; voxel size 0.3 mm) and voxel size (b; TE 20 ms) is shown.

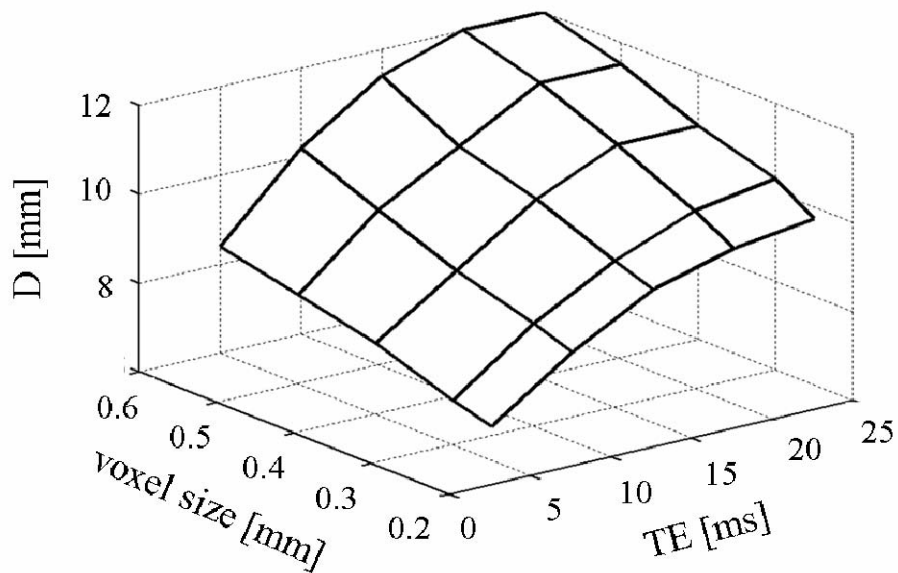


**Figure 5.10** The diameter of image signal void in  $\vec{B}_0$  direction in dependence on the in-plane spatial resolution and the echo time TE. Iron concentration  $15 \mu\text{g Fe} / 10 \mu\text{l}$ ,  $B_0 = 3$  Tesla.

## Dependence of signal void on iron concentration

The relationship between the diameter of signal void  $D$  and the iron concentration (mass  $m$  of iron per 10  $\mu\text{l}$ ) in solution was properly described according to

$$D(m) = D_{10} \cdot \log_{10} \left( \frac{m}{m_0} \right). \quad (5.3)$$

In case of SPIO labeled cells the functional relationship between the diameter of signal void and the number of cells  $n$  / 10  $\mu\text{l}$  had a similar form:

$$D(n) = D_{10} \cdot \log_{10} \left( \frac{n}{n_0} \right). \quad (5.4)$$

The values of  $m_0$ ,  $n_0$ , and  $D_{10}$  were obtained by fitting Eq. (5.3) and Eq. (5.4), respectively, to the measured data (Fig. 5.11).

For all TE and voxel sizes considered, the diameter of signal void increased beyond a concentration threshold. This threshold characterized the lower limit of iron concentration that produced a measurable image signal void. According to the present experimental set-up, the detection of concentrations as low as 75  $\mu\text{g Fe} / \text{ml}$  in SPIO containing solution or 125  $\mu\text{g Fe} / \text{ml}$  in suspensions of SPIO labeled cells was certainly possible. A non-linear dependency of  $D(m)$  on  $m$  was revealed: the higher the iron concentration, the smaller the slope  $d(D(m)) / dm$ .

The regression parameter (i.e.,  $m_0$ ,  $n_0$ , and  $D_{10}$ ) were affected by the choice of the echo time as well as the in-plane spatial resolution. The increase in  $D(m)$  and  $D(n)$  with TE affected  $D_{10}$  as well as  $m_0$  and  $n_0$ . By increasing TE, reductions in  $m_0$  and  $n_0$  were found. In contrast,  $D_{10}$  increased with TE in that case.

SPIO containing solutions and SPIO labeled cells produced different signal voids in case of identical local iron concentrations. For iron concentrations  $> 5 \mu\text{g Fe} / 10 \mu\text{l}$ , SH U 555A labeled SK-Mel28 human melanoma cells produced larger signal voids as compared to the same iron concentration of SPIO in solution.

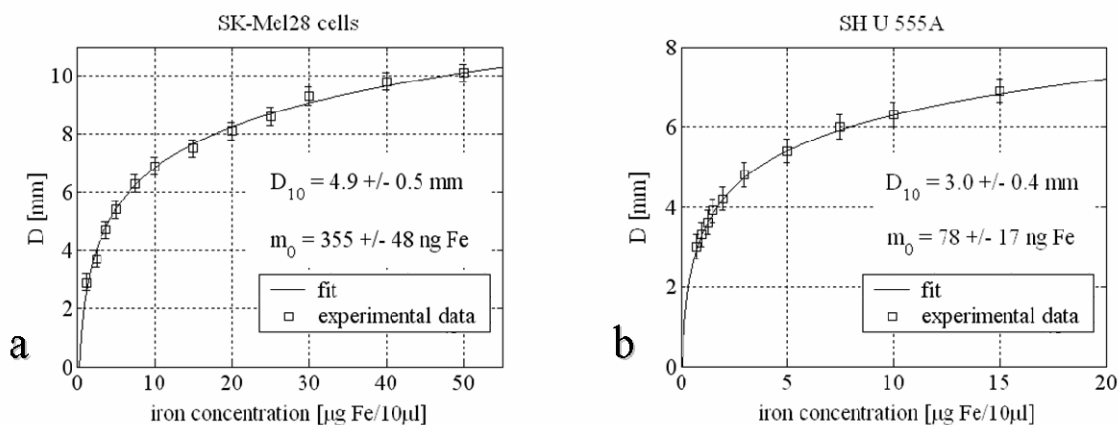


**Figure 5.11** Diameter of signal void induced by various concentrations of SPIO labeled SK-Mel28 human melanoma cells and various concentrations of SPIO (SH U 555A) in solution. A non-linear relationship of the diameter  $D$  of signal void and iron concentration was revealed:  $D(m) = D_{10} \cdot \log_{10}(m/m_0)$ . 3d FLASH sequence:  $TE = 20 \text{ ms}$ ,  $0.3 \text{ mm}$  isotropic spatial resolution (voxel side length),  $B_0 = 3 \text{ Tesla}$ .

## 5.4 Interpretation of the numerical and the experimental results

### 5.4.1 Spatial accuracy in MRI of magnetically labeled cells

MR imaging of certain biological processes including stem cell homing and cancer cell migration requires tracking aggregations of magnetically labeled cells with high spatial accuracy in the recorded MR image: a proper spatial correlation between the signal void recorded and the cell cluster. As demonstrated, this spatial accuracy is of inferior quality the longer the echo time and the larger the size of the imaging voxel, respectively.

In the present study, MRI signal voids were anticipated to comprise the aggregation of labeled cells as well as the signal dephasing region around those aggregations. The effects of sequence parameters including echo time, voxel size, and plane of view orientation to the geometry and the extension of this dephasing region were studied using numerical simulations and MR measurements. The results imply that in static signal dephasing MRI at  $TE \sim 20 \text{ ms}$  a particular cell aggregation may be visible in the MR image as an image signal void enlarged

by a factor of approximately 1.5 compared to the real size of the cell cluster. It is anticipated that longer TE might prevent a clear localization of labeled cells in the MR image and may cause a significant overestimation of the volume of labeled cells under in vivo conditions.

In order to benefit from high spatial accuracy to detect aggregations of labeled cells, the echo times should be as short as possible and high spatial resolution (i.e., small voxel size) is preferable. Very short TE can be achieved using advanced MR scanners, which usually offer fast 3d gradient echo sequences with TE of less than 2-3 milliseconds [Sch05]. Limitations in minimizing the voxel size definitely arise from the corresponding reduction in the signal-to-noise ratio (SNR). However, gradient coil inserts [Heyn06], inductively coupled radiofrequency coils [Graf03] or dedicated animal scanners that are operated at high magnetic field strengths [Stroh05] allow for spatial resolutions of less than 100  $\mu\text{m}$  combined with excellent SNR.

A plane of view with an angle around  $54^\circ$  (the “magic angle”) to the external  $B_0$  field has no additional magnetic field inhomogeneity and signal dephasing effects along one direction. This property is anticipated to be advantageous for the detection of cell cluster with high spatial accuracy, since the image signal void directly reflects the size of the cellular aggregation in that case. For this purpose, proper orientation of the MR image is recommended. The physical diameter of the cell cluster was denoted  $D_0$  in the present paper.

#### 5.4.2 Sensitivity in MRI of magnetically labeled cells

The increase in the image signal void with echo time and voxel size may allow the detection of even lower concentrations of labeled cells. Under experimental conditions, an increase in the regression parameters  $D_{10}$ ,  $m_0$ , and  $n_0$  with TE as well as voxel size were revealed. It is anticipated that this corresponds to an increase in the sensitivity to monitor labeled cells.

In order to benefit from high MR sensitivity in the detection of aggregations of labeled cells, appropriate  $T_2^*$ -weighted pulse sequences with sufficiently long TE should be applied. Gradient echo sequences provide superior sensitivity to the SPIO induced magnetic field perturbations as compared to spin echo approaches [Yab94, Bow02, Pint06b]. The results of the present numerical simulations demonstrate that the diameter of the signal void approximately doubles if TE increases from 5 ms to 60 ms. Notably, the relative enhancement of the signal

void with TE is independent of magnetization. It was revealed that this effect is even independent of the cell concentration under experimental conditions.

Furthermore, extension and geometry of the image signal void were found to depend on the orientation of the plane of view with respect to  $\vec{B}_0$ . Applying slice orientations containing the axis of the  $\vec{B}_0$  field, the observable signal void should resemble the characteristic magnetic dipole field pattern. It is anticipated that for transverse slices perpendicular to  $\vec{B}_0$  the induced signal void will show circular geometries.

### 5.4.3 Relevance for cell quantification

The area of signal void increases with local magnetization, which was considered the physical quantity of choice to study concentration effects of magnetically labeled cells. In both numerical simulations and MR measurements the dependency between the diameter of signal void and the iron concentration respectively the magnetization of the spherical particle was non-linear and was found to obey an empirical logarithmic function.

The proposed preparation strategy with a well-defined spatial distribution of magnetic material in an agar gel phantom produced reliable results. Standardized measurement conditions, as a critical prerequisite to obtain reproducible results, could be achieved. This allowed for the systematic investigation of the relationship between signal extinction and local iron concentration for various concentrations of SPIO labeled cells as well as SPIO containing solutions.

The proposed preparation strategy appears clearly superior compared to set-ups with randomly distributed magnetic material in glass and plastic tubes. The latter have caused an almost undefined spatial distribution of magnetic material and have induced signal voids biased by phantom-related susceptibility artefacts [Him04, Dal03, Dal05], as based on the inaccurate choice of phantom material and geometry.

The effectiveness of stem cell migration may be assessed by quantifying labeled cells. The demonstrated concentration dependency of the diameter of signal void represent a potential calibration standard for the quantitative assessment of labelled cells and possibly the iron load per cell in vitro and even in vivo. In order to optimize pulse sequences as well as sequence

parameters appropriate tissue models might be derived, on the basis of the proposed quantification.

It is anticipated that a certain concentration of labeled cells cause comparable signal voids under both in vitro as well as in vivo conditions, since the physical principles describing signal dephasing are identical. Thus, investigating the dependency of the signal void on cell concentration in vitro may allow quantifying aggregations of labeled cells in vivo. It is important to know that those calibrations must be separately performed for each sequence and each set of sequence parameters that is being used for the measurement of the SPIO induced signal void.

#### 5.4.4 Limitations of the numerical model

It is worthwhile reviewing the limitations resulting from the assumptions and approximations upon which the numerical model is based. Firstly, signal dephasing in the vicinity of spherical aggregations of SPIO labelled cells was studied. For the calculation of the magnetic field inhomogeneities the magnetic dipole approach was used. For spherical aggregations of magnetically labelled cells this assumption should be valid. For arbitrarily shaped cell aggregations, however, the validity of this assumption is less certain because the actual magnetic field distribution close to the cell cluster depends on their shape and the distribution of SPIO loaded cells.

In addition to spherical aggregations of labeled cells, cells can aggregate arbitrarily. Several studies have shown that cells loaded with SPIO compared to unlabeled cells had similar viability and proliferation profiles and also maintained their differentiation capacity [Him04]. One may suppose, that the in vivo distribution of labeled cells is determined by the tissue structure, in which cells have been transplanted or to which cells have migrated. In contrast to spherical cell aggregations, no analytical description of the magnetic field perturbation is available in case of arbitrarily shaped cell cluster. Studying those geometries was beyond the scope of the present work.

Secondly, aggregations of labeled cells induce intense magnetic field gradients over fairly large distances. A linear field gradient over the imaging voxel was assumed since the voxel

size is usually small compared to the extension of the field distortion. Thirdly, the MR imaging voxels were approximated to be isotropic.

Fourthly, a phase dispersion criterion  $\delta\phi \geq 2\pi$  parallel to one side of an isotropic imaging voxel was used as the criterion to compute the image signal void. Under experimental conditions, however, considerable signal loss may occur prior to this numerical criterion is accomplished. This introduces measurement uncertainties in the experimental determination of the extension and in the delineation of the signal voids, and thus represents another limitation in the comparison of numerical results and MR measurements.

Finally, water diffusion effects were neglected in the numerical model. Given the size of the aggregation and the intense magnetic field inhomogeneities caused by thousands to millions of labelled cells, solvent spins move so slowly that they appear to be stationary, meaning that diffusion has practically no effect on signal dephasing. Thus, considering this static dephasing regime, a relationship between field distortion and MRI signal dephasing could be found.



## Chapter 6

# Positive contrast in MRI of magnetically labeled cells

### 6.1 Introduction

Contrast agents incorporating superparamagnetic iron oxide (SPIO) nanoparticles have shown much promise as a means to visualize small volumes corresponding to labeled cells using MRI. Cells labeled with SPIO cause magnetic field inhomogeneities within picture elements as well as on the macroscopic scale. The magnetic field distortions induce significant signal dephasing and an enhanced signal decay regarding water molecules near the cell. In practise, labeled cells are reflected either as low-intensity signal spots or signal voids, particularly in  $T_2^*$ -weighted gradient echo MRI [Pint05a].

With the signal void as the principle for detection, SPIO particles behave as ‘negative contrast’ agents. This is opposed to ‘positive contrast’ agents such as gadolinium chelates that increase the MR signal intensity by shortening the longitudinal relaxation time constant  $T_1$  of the surrounding tissue so that the tissue appears bright in  $T_1$ -weighted MRI. In contrast to longitudinal relaxation, the signal dephasing effects benefit from the use of higher magnetic fields, because of stronger susceptibility induced magnetic field gradients. However, the saturation of the SPIO magnetization must be taken into account [Kal00].

Positive tissue contrast with SPIO using appropriate  $T_1$  weighted MR sequences is achievable employing ultrasmall superparamagnetic iron oxide (USPIO) particles with hydrodynamic diameters of less than 20 nm. Since USPIOs are not immediately recognized by the hepatic and splenic mononuclear phagocytotic system, the blood half lives of USPIOs are relatively long as compared to those of larger SPIO particles. Proper blood half lives and the inherent property to shorten  $T_1$  have allowed USPIOs to be used as MR angiography contrast agents. However, for larger particles [Tau03] as well as magnetically labeled cells [Sim06], the ratio of longitudinal to transversal relaxivity ( $r_1/r_2$ ) decreases. Under those circumstances the generation of positive tissue contrast (i.e., bright visualization) by exploiting the  $T_1$  effects of iron oxide nanoparticles is usually inefficient because of competing  $T_1$  and  $T_2/T_2^*$  relaxation effects (Table 6.1).

**Table 6.1** Physical properties and relaxivities of superparamagnetic iron oxide nanoparticles. The values were taken from the literature and were obtained at  $B_0 = 0.47$  Tesla. PEG: polyethylenglycol,  $r_1$ : longitudinal relaxivity,  $r_2$ : transverse relaxivity.

substance	hydrodynamic particle size [nm]	coating material	$r_1$ [L mmol <sup>-1</sup> s <sup>-1</sup> ]	$r_2$ [L mmol <sup>-1</sup> s <sup>-1</sup> ]	$r_1 / r_2$
SH U 555A [Law97]	50 - 100	carboxydextran	25	164	0.15
AMI-25 [Jung95]	80 - 150	dextran	30	100	0.3
AMI-227 [Tan98]	20 - 40	dextran	31	78	0.39
NC100150 [Sae98]	20	amylum / PEG	20	35	0.57
SH U 555C [Kno98]	20	carboxydextran	18	41	0.44
VSOP-C184 [Wag02]	8	citrate	19	29	0.66

A fundamental drawback of negative contrast agents is that the agent cannot be distinguished from signal voids in the image reflecting areas of low proton density. Furthermore, various other sources of hypointensities can be present or the magnetic field background can be inhomogeneous in MR images. Due to the negative contrast, it is often difficult to accurately

determine the presence of magnetically labeled entities under in vivo conditions, and the differentiation of iron labeled cells and an inherent tissue structure is often problematic. Thus locating labeled cells by means of signal loss is challenging in areas with low proton density and significant  $T_2^*$  relaxation effects.

In addition, negative contrast agents suffer from partial volume effects. These arise when the imaging voxel contains tissue fractions with a range of relaxation rate values and only the weighted mean value is assigned to the imaging voxel. Furthermore, as demonstrated in previous chapters, the characteristic of the signal void induced by aggregations of magnetically labeled cells depends critically on the spatial resolution (i.e., the voxel size) of the image.

Selective imaging with positive contrast techniques is a highly promising solution [Sep03, Bak06, Cun05, Mani06, Pint05b, Zur06]. For better localization of SPIO labeled cells, it would be preferable to achieve positive contrast that will provide increased signal-to-noise (SNR) and contrast-to-noise ratios (CNR). This may allow for greater certainty in identifying labeled cells and determining their spatial distribution.

The purpose of this work was to develop a MRI method which allows for ‘positive contrast MR imaging’ of magnetically labeled cells. The Larmor frequency shift near labeled cells as well as near aggregations of labeled cells was exploited to obtain bright visualization applying spectral selective saturation pulses. This radiofrequency preparation was used to suppress the on-resonance water signal. The off-resonance water signal surrounding the labeled cells contributed to the MR image, so that only the fluid immediately adjacent to the labeled cells was visible in the MR image. Positive contrast imaging was achieved for volume elements containing labeled cells as well as for volume elements close to cell cluster. The results of these investigations were published previously [Pint05b].

## 6.2 Materials and methods

### 6.2.1 Frequency selectivity of a radiofrequency pulse

In the NMR experiment, an oscillating magnetic field  $\vec{B}_{rf}(t)$  is superposed perpendicularly to the static magnetic field  $\vec{B}_0$ . The term ‘radiofrequency (rf) pulse’ is generally used as a syno-

onym for the  $\vec{B}_{rf}(t)$  field, because the field is turned on relatively short (few microseconds to milliseconds) and it oscillates in the radio frequency range (e.g., 42.6 MHz for protons at 1 Tesla). Often the  $\vec{B}_{rf}(t)$  field is ‘linearly polarized’. Modern MRI whole-body systems allow for ‘circularly polarized’ fields directly, with the advantage of reduced rf power deposition in the tissue.

The main parameters characterizing the rf pulse include the pulse envelope function  $B_{rf}(t)$ , the excitation carrier frequency  $\omega_{rf}$ , and the initial phase angle. As pointed out in chapter 2, the excitation frequency is determined by the resonance condition (Larmor equation). The envelope function  $B_{rf}(t)$  specifies the duration of an rf pulse, and thus its spectral excitation profile.

Proper design of frequency selective rf pulses allows for the spatial localization of the MRI signal during the slice selective excitation procedure. Due to the temporary application of a controlled magnetic field gradient during the imaging process, the spin resonance frequency is made position-dependent, and thus the frequency selective rf pulse becomes spatially selective. Furthermore, frequency selective rf pulses are applied for the suppression / excitation of resonances such as water and lipids in MR spectroscopy and chemical-shift selective MRI.

The generation of rf pulses with an appropriate frequency selectivity is an important subject of MRI. The central issue are the characteristics of the pulse envelope function  $B_{rf}(t)$ . The ‘Fourier approach’ is a convenient approach for selective rf pulse design (note that this approach is only valid for small flip angles, as discussed below). The primary assumption is that the pulse envelope function  $B_{rf}(t)$  is related to the respective spectral excitation profile  $p(\nu)$  by the Fourier transform.

The application of rectangular-shaped (i.e., ‘boxcar’ functions) excitation profiles

$$p(\nu) = \Pi\left(\frac{\nu - \nu_0}{\Delta\nu}\right) \quad (6.1)$$

would be most convenient for both slice selection as well as frequency selective suppression / excitation. Making use of the Fourier transform relationship

$$\text{sinc}(\pi \cdot a \cdot t) \leftrightarrow \frac{1}{a} \cdot \Pi\left(\frac{\nu}{a}\right) \quad (6.2)$$

the pulse envelope function is found to

$$B_{\text{rf}}(t) = A \cdot \text{sinc}(\pi \cdot a \cdot t) = A \cdot \frac{\sin(\pi \cdot a \cdot t)}{\pi \cdot a \cdot t}. \quad (6.3)$$

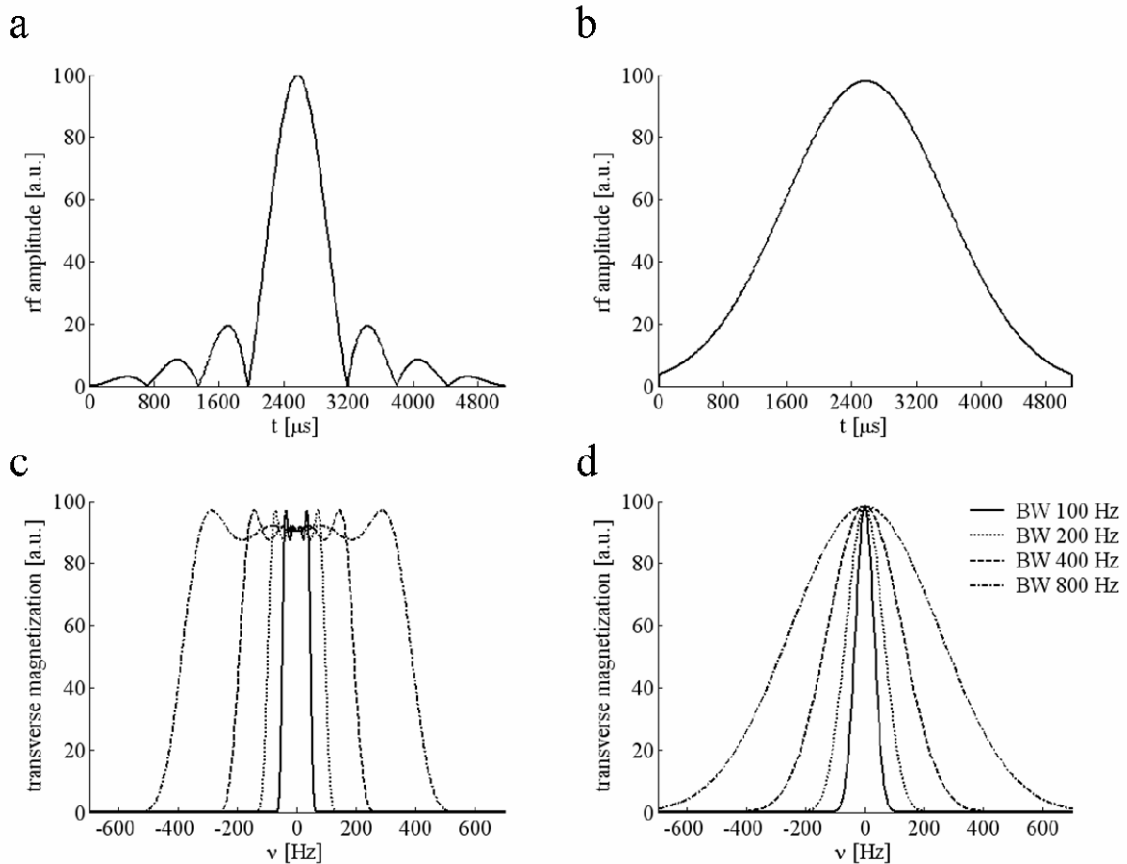


**Figure 6.1** Sinc (a) and Gaussian pulses (b) are shown. The pulse's time domain profiles were taken from the MRI system software IDEA (Siemens Medical Solutions). In the basic setting, the pulse consists of 512 data points with a time interval of 10  $\mu\text{s}$  (i.e., the dwell time) between two following data points. This corresponds to a pulse bandwidth (BW) of 1,666 Hz for the sinc pulse and 375 Hz for the Gaussian pulse. Maintaining the number of data points and varying the dwell time allows specifying the pulse bandwidth. Representative spectral excitation profiles of sinc (c) and Gaussian (d) pulses, as calculated by the Fourier approach, are displayed.

Although the Fourier approach is rather simple to design rf pulses, the resulting pulse envelope function is not entirely accurate, because the nuclear spin system behaves non-linearly

during the excitation process and relaxation effects must be accounted for. The most precise approach is to solve the Bloch equations numerically. Nevertheless, under the small flip angle assumption, the Fourier approach predicts the spectral excitation profile properly. However, the validity of the Fourier approach breaks down for large flip angle excitations.

Eq. (6.3) implies that a rectangular excitation profile requires an infinitely long ‘sinc pulse’. However, such a pulse is not physically realizable. Firstly, a practical pulse will necessarily start at  $t = 0$ . Secondly, it lasts only a finite period of time: the pulse duration  $\tau_p$ . Due to the finite length of the pulse, the excitation profile is more complicated and deviates from the rectangular excitation profile (Fig. 6.1). In case of a sinc pulse, this ‘pulse truncation effect’ can be minimized by integrating as many sidelobes into the pulse as possible.

Sinc and Gaussian pulses of finite length were exported from the Siemens MRI scanner software IDEA and are displayed in Fig. 6.1. To assess the spectral excitation profile, the time domain pulses were Fourier transformed. Generally, the shorter the pulse the broader the spectral excitation profile. On the other hand, longer pulses ( $> 10$  ms) will produce excitation of a narrower frequency bandwidth. In the current work the frequency selective rf pulses illustrated in Fig. 6.1 were implemented in a two-dimensional (2d) spin echo sequence and were used for the spectrally selective saturation of the on-resonance water signal.

## 6.2.2 Principle of spectrally selective saturation

Because of the difference in the bulk magnetic susceptibility with respect to the background tissue, cells labeled with SPIO cause magnetic field inhomogeneities on the microscopic scale within the MR voxel. Furthermore, aggregations of labeled cells induce macroscopic magnetic field distortions and magnetic field gradients over distances that are larger than the imaging voxel. According to the Larmor equation, these field variations cause spins within voxels to precess at different frequencies, leading to intravoxel spectral broadening of the resonance frequency distribution. Fig. 6.2 displays intravoxel frequency distributions computed for various concentrations of magnetically labeled cells.

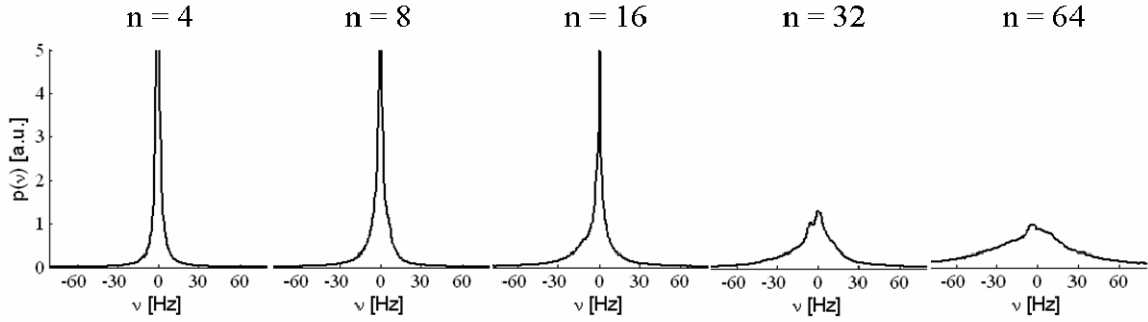


**Figure 6.2** Frequency distributions computed for increasing concentrations of magnetically labeled cells. The numerical model described in previous chapters was applied for computation purposes. The number of cells (identical magnetic spheres) was varied from  $n = 4$  to  $n = 64$ . Simulation parameters: magnetization  $M = 150 \mu\text{T}$ , radius of sphere = 4.0 computational units, region-of-interest (voxel)  $100 \times 100 \times 100 = 10^6$  computational units. Note that for  $n = 4$  and  $n = 8$  the magnitude  $p(\nu)$  is truncated.

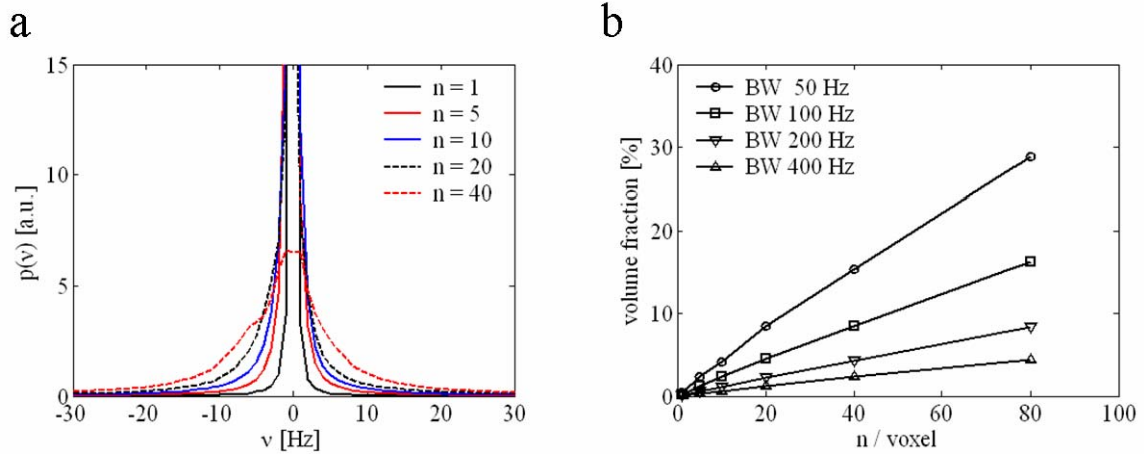


**Figure 6.3**

(a) Frequency distributions for increasing concentrations of magnetically labeled cells, computed with the numerical model described in previous chapters. Simulation parameters: number of cells (magnetic spheres)  $n = 1, 5, 10, 20, 40$ ; magnetization  $M = 50 \mu\text{T}$ , radius of sphere = 5.0 computational units, region-of-interest (voxel)  $100 \times 100 \times 100 = 10^6$  computational units. Note that the magnitude  $p(\nu)$  is truncated.

(b) While applying a saturation pulse with bandwidth (BW) on frequency  $\nu = 0$  only a certain volume fraction of spins may contribute to the MR signal. This volume fraction depends on both the concentration of cells within the voxel and the bandwidth of the pulse applied. Saturation pulses with a rectangular excitation profile (i.e., a boxcar function) were assumed.

The Larmor frequency shift near labeled cells was exploited to obtain bright visualization applying spectrally selective saturation pulses. The principle of spectrally selective saturation was to suppress the overall signal from all proton spins precessing at the spectrometer reference frequency  $\nu_0$  (i.e., the on-resonance water signal) by means of a frequency selective pulse prior to each sequence repetition. In contrast to the on-resonance spins the off-resonance spins, which have a resonance frequency shift with respect to  $\nu_0$ , were not affected by the preparation pulse. Since the proton spins surrounding the labeled cells are anticipated to have a shifted Larmor frequency, only the fluid immediately adjacent to the labeled cells should be visible in the MR image after spectrally selective saturation. Figure 6.3 displays data from numerical simulations demonstrating the contributions to the MR signal from off-resonance spins after on-resonance saturation.

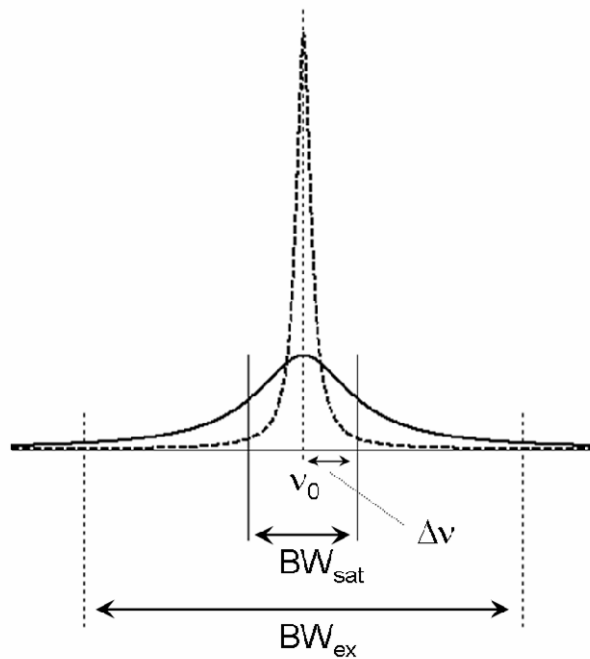


**Figure 6.4** Spectral broadening of the resonance frequency distribution due to magnetically labeled cells. The principle of spectrally selective saturation was to suppress the signal originating from all proton spins precessing near the spectrometer reference frequency  $\nu_0$  by means of a frequency selective saturation pulse. Spins with a shifted Larmor frequency, due to magnetic field inhomogeneities, are not affected by the saturation pulse and thus contribute to the MR image.  $\nu_0$ : spectrometer reference frequency,  $\Delta\nu$ : frequency shift,  $BW_{sat}$ : bandwidth of saturation pulse,  $BW_{ex}$ : bandwidth of slice-selective excitation pulse



Spectrally selective saturation with different bandwidth  $BW_{\text{sat}}$  was employed (Fig. 6.4). Spin ensembles with resonance frequency shifts  $\pm\Delta\nu$  with respect to  $\nu_0$  were allowed to contribute to the spin echo signal formation as long as the saturation pulse bandwidth  $BW_{\text{sat}}$  was smaller than  $2\cdot\Delta\nu$  and the bandwidth  $BW_{\text{ex}}$  of the slice-selective excitation pulse was sufficiently high to excite off-resonance spins.

### 6.2.3 Pulse sequence timing

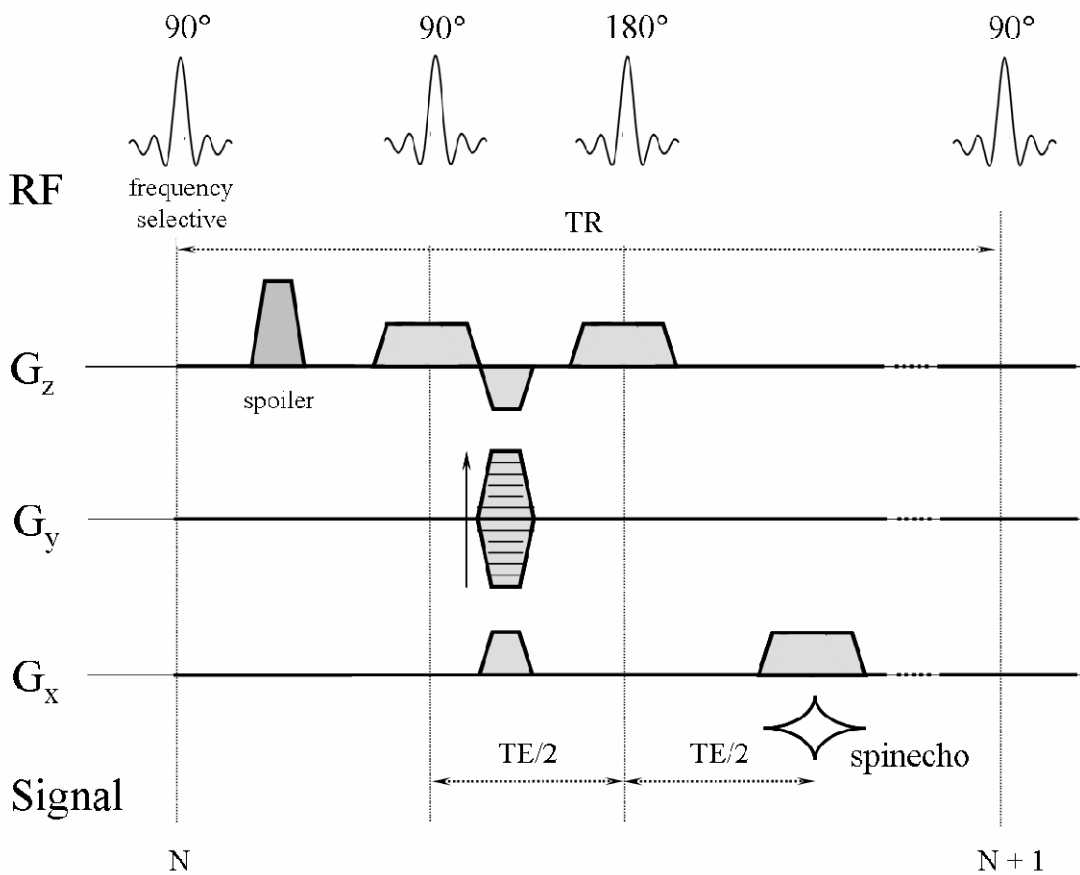


**Figure 6.5** Pulse diagram of the 2d spin echo sequence with integrated frequency selective saturation pulse. This preparation was implemented prior to each sequence repetition.

Sinc or Gaussian frequency selective saturation pulses with varying bandwidths  $BW_{\text{sat}}$  were implemented in a two-dimensional (2d) spin echo sequence. A pulse diagram is displayed in Fig. 6.5. In order to dephase the transverse magnetization that was excited with  $BW_{\text{sat}}$ , a subsequent spoiler gradient was applied in the interval between the frequency selective saturation pulse and the slice-selective excitation pulse of the 2d spin echo sequence.

The automatized scanner adjustment was employed for shimming and to determine  $\nu_0$ . Concerning the examination of low cell concentrations, microscopic effects near magnetic dipoles have to be regarded. In this case, a shift of the center frequency in the labeled volumes can be neglected. For high local cell concentrations the volume labeled with SPIO amounted to less than 0.1 % of the overall sample volume. Thus, frequency adjustment was practically determined by voxels far away from the most intense field distortions induced by aggregations of labeled cells and a shift of the center frequency can be also neglected in that case.

## 6.2.4 Preparation of cell samples

SK-Mel28 human melanoma cells were labeled by means of incubation with SH U 555A. The labeling protocol employed has already been described in chapter 3. Various concentrations of 5, 20, 30, 50, and 75 labeled cells per  $\mu\text{l}_{\text{gel}}$  were homogeneously suspended in agar gel (1%). An unlabeled agar gel sample was used as a reference. An agar gel provided a 3d matrix for direct injection of cell clusters, as shown in chapter 5. Aggregations of  $1 \cdot 10^3$ ,  $3 \cdot 10^3$ ,  $6 \cdot 10^3$ , and  $10 \cdot 10^3$  labeled cells per  $\mu\text{l}_{\text{gel}}$  were prepared and investigated by means of MR measurements.

## 6.2.5 MR measurements

All measurements were performed on a 3 Tesla MR whole-body scanner (Magnetom Trio<sup>®</sup>, Siemens Medical Solutions, Erlangen, Germany). The dedicated wrist coil was used for rf excitation and signal acquisition. As shown in Fig. 6.1, sinc and Gaussian pulses, respectively, were implemented in a 2d spin echo sequence for the purpose of frequency selective saturation. The saturation pulse bandwidth  $BW_{\text{sat}}$  was varied to 100, 200, 400, and 800 Hz. The bandwidth of the slice-selective excitation pulse was  $BW_{\text{ex}} = 1$  kHz. The other sequence parameters of the spin echo sequence amounted to: field of view  $128 \times 128$  mm<sup>2</sup>, matrix size  $128 \times 128$ , slice thickness 1.0 mm, voxel size  $1.0 \times 1.0 \times 1.0$  mm<sup>3</sup>, repetition time TR 4000 ms, echo time TE 10 ms.

For low concentrations of homogeneously suspended magnetically labeled cells the relative MR contrast between the labeled (signal intensity  $S_1$ ) and unlabeled (signal intensity  $S_2$ ) specimen was evaluated.

$$C_{\text{rel}} = \frac{S_1 - S_2}{S_1 + S_2} \quad (6.4)$$

The 2d spin echo sequence with implemented spectrally selective saturation pulses was tested and optimized by means of phantom measurements. A fat-water phantom with known chemical shift  $\approx 400$  Hz between the fat and the water resonance at 3 Tesla was used.

## 6.3 Results

### 6.3.1 Fat-water phantom

The frequency shift of the fat resonance with respect to the water resonance due to chemical shift was exploited for the optimization of the 2d spin echo sequence with implemented frequency selective saturation pulse. MR images were acquired without and with spectrally selective saturation. The differences between spin echo sequences with implemented sinc and Gaussian saturation pulses, respectively, are illustrated in Fig. 6.6.

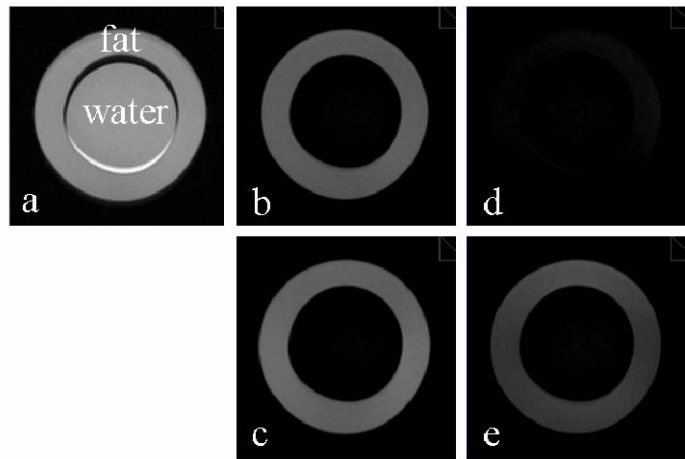


**Figure 6.6** MR images of the fat-water phantom. Image (a) was acquired with a 2d spin echo sequence without, and images (b-e) were acquired with implemented frequency selective saturation pulses. (b) sinc pulse ( $BW_{sat} = 200$  Hz), (c) Gaussian pulse ( $BW_{sat} = 200$  Hz), (d) sinc pulse ( $BW_{sat} = 800$  Hz), (e) Gaussian pulse ( $BW_{sat} = 800$  Hz). Sinc pulses demonstrate higher frequency selectivity as compared to Gaussian pulses.

### 6.3.2 Low concentrations of magnetically labeled cells

MR images of samples containing suspensions of SPIO labeled cells, acquired without spectrally selective preparation, are given in Fig. 6.7a. The relative contrast between the labeled and the unlabeled volume increased linearly with cell concentration (Fig. 6.7b).

Under the present experimental conditions, applying spectral selective saturation led to hyperintensity of the labeled volume for all concentrations  $\geq 20$  labeled cells /  $\mu\text{l}$  investigated. Note that a sinc pulse was used in that case. Significant increases in the relative contrast  $C_{\text{rel}}$  compared to the unlabeled agar gel sample were revealed. The method led to a calculated contrast that increased with cell concentration. With increasing cell concentration  $C_{\text{rel}}$  raised to maximum that was given by 52 % ( $\text{BW}_{\text{sat}} = 100$  Hz) and 28 % ( $\text{BW}_{\text{sat}} = 200$  Hz), found for the highest concentration of 75 labeled cells /  $\mu\text{l}_{\text{gel}}$ . For all cell concentrations the entire sample was free of signal for  $\text{BW}_{\text{sat}} \geq 400$  Hz.

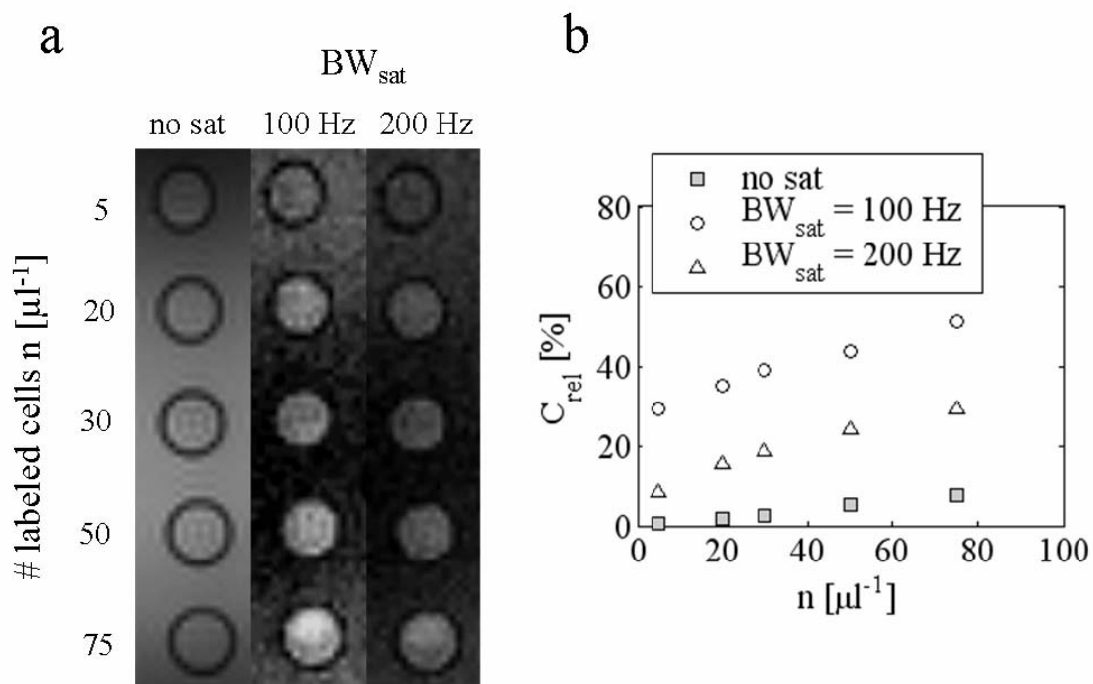


**Figure 6.7** (a) MR images of samples with various concentrations of suspended magnetically labeled cells. The images were acquired without and with spectrally selective saturation with sinc pulse bandwidth  $\text{BW}_{\text{sat}} = 100$  Hz and  $\text{BW}_{\text{sat}} = 200$  Hz, respectively. (b) Relative contrast  $C_{\text{rel}}$  of samples containing labeled cells as compared to the unlabeled control sample.

### 6.3.3 Aggregations of magnetically labeled cells

Aggregations of magnetically labeled cells were reflected as signal voids in the MR images. The size of the induced signal void increased with local iron oxide concentration (Fig. 6.8). The signal voids were surrounded by bright image structures, which corresponded to image artefacts in read-out direction, typical for spin echo sequences. These were visible although

spectrally selective saturation was applied. However, these were superimposed by positive contrast in that case. Signal could be detected near cell aggregations despite saturation. The magnetic dipole field around aggregations of labeled cells was revealed with positive contrast. Difference in positive contrast images between sequences with sinc and Gaussian pulses are displayed in Fig. 6.9.

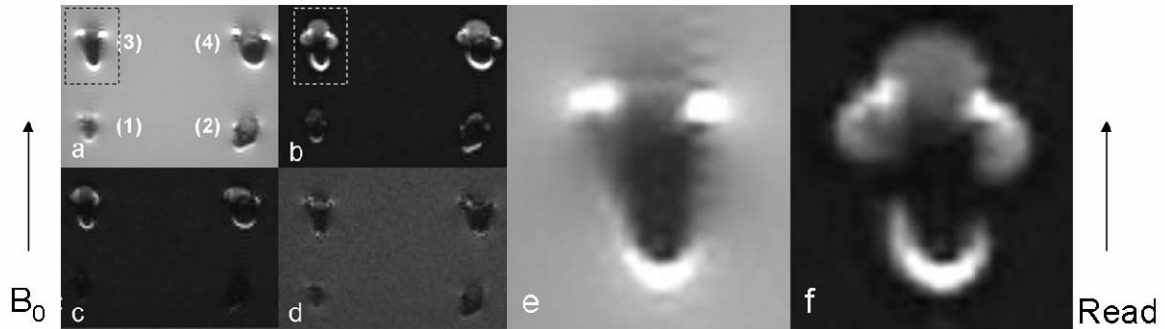


**Figure 6.8** MR images of an agar gel matrix with embedded cluster of magnetically labeled cells. The images were acquired at  $TE = 10$  ms without (a) and with (b-d) spectral selective saturation applying frequency selective pulses with bandwidth  $BW_{sat} = 100$  Hz (b),  $BW_{sat} = 200$  Hz (c), and  $BW_{sat} = 400$  Hz (d). Magnified areas of (a) and (b) are shown in (e) and (f). (1)  $1 \cdot 10^3$  cells, (2)  $3 \cdot 10^3$  cells, (3)  $6 \cdot 10^3$  cells, and (4)  $10 \cdot 10^3$  cells /  $\mu\text{l}_{gel}$ .

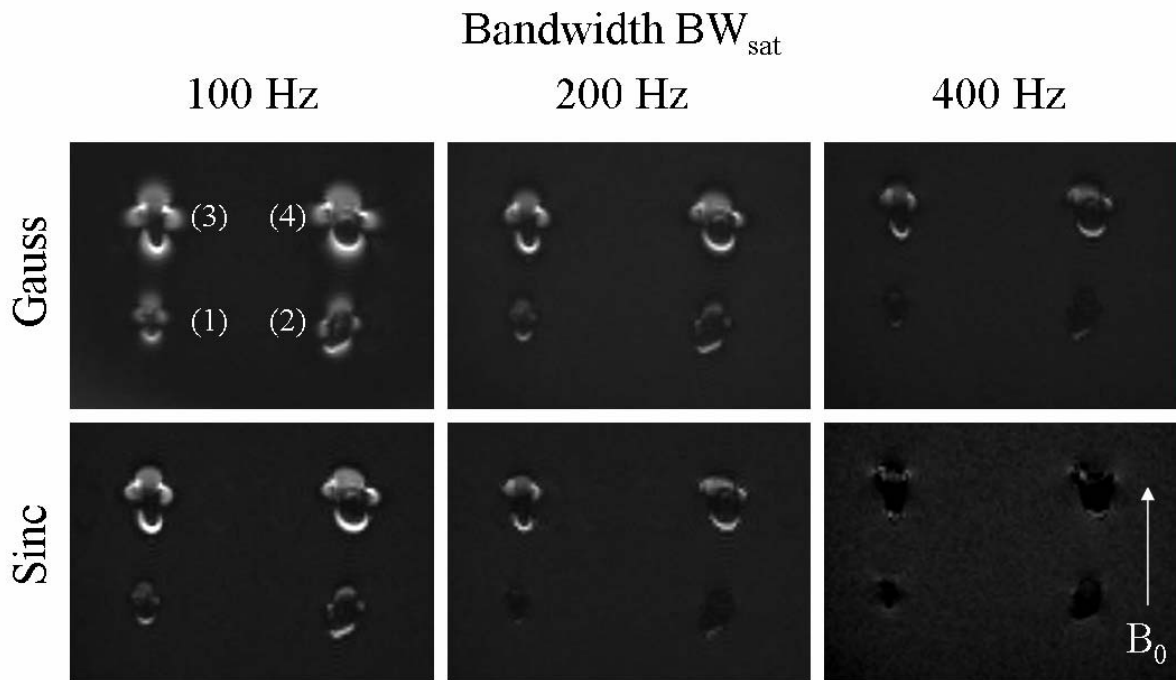


**Figure 6.9** Positive contrast images for aggregations of magnetically labeled cells. Gaussian and sinc pulses with increasing bandwidth were used. (1)  $1 \cdot 10^3$  cells, (2)  $3 \cdot 10^3$  cells, (3)  $6 \cdot 10^3$  cells, and (4)  $10 \cdot 10^3$  cells /  $\mu\text{l}_{gel}$ .

## 6.4 Interpretation of the results

The main concept of this study was the selective depiction of cells labeled with superparamagnetic iron oxide particles by using spectrally selective saturation of the background signal. The on-resonance water signal was suppressed, whereas the off-resonance water signal near labeled cells was detected, so that only the volume immediately adjacent to magnetically labeled cells was visible in the acquired MR image.

The resultant ‘positive contrast’ is the opposite of the ‘negative contrast’, which results from signal dephasing in MRI due to magnetic field inhomogeneity effects. In the present work, positive contrast imaging was achieved for both volume elements containing labeled cells as well as for volume elements close to cell cluster. It was demonstrated that this contrast inversion and selective visualization of SPIO loaded cells requires only a manageable modification of conventional MR imaging sequences. In this work, a frequency selective saturation pulse was integrated in a standard 2d spin echo sequence. In order to minimize signal dephasing effects the spin echo approach was selected in the present study. Positive contrast by means of spectrally selective saturation of the background signal can be also achieved using gradient echo based sequences (data not shown). However, signal dephasing is anticipated to dominate under these circumstances, reducing the gain in the image contrast due to the achievement of the positive contrast.

For cell trafficking, using the signal loss as the means for cell localization may be challenging in tissues with inherent magnetic field inhomogeneities, because these areas produce significant signal dephasing. For better localization of cells, it would be preferable to achieve positive contrast, rather than negative contrast. As demonstrated, this will provide increased signal-to-noise (SNR) and contrast-to-noise ratios (CNR). It is anticipated, that this may allow for greater certainty in identifying labeled cells.

Positive contrast was observed in voxels containing labeled cells as well as in voxels near aggregations of labeled cells. The positive contrast was a function on the local concentration of labeled cells, the echo time TE, the frequency selectivity of the saturation pulse, the bandwidth of the saturation pulse  $BW_{\text{sat}}$  as well as of the slice-selective excitation pulse  $BW_{\text{ex}}$ .

Under the experimental conditions realized herein, bright visualization of voxels with concentrations  $\geq 20$  labeled cells /  $\mu\text{l}$  was achieved with  $BW_{\text{sat}} = 100$  Hz and  $BW_{\text{sat}} = 200$  Hz, respectively. Since the signal dephasing, which is competing with positive contrast generation, increases with echo time TE, short echo times are preferable in positive contrast techniques employing spectral selective pre-saturation. It is anticipated that an optimum in positive contrast CNR results from the conserved magnetization after spectral selective saturation due to spectral broadening, and the respective signal loss due to the dephasing of the magnetization.

As shown for in vitro preparations of magnetically labeled cells, the implementation of spectral selective saturation in a 2d spin echo sequence led to improvements in imaging contrast. The positive contrast mechanism was exploited for bright visualization of the surroundings close to spherical aggregations of labeled cells. It is anticipated that this concept can be generalized to various types of magnetic field distortions, as long as inhomogeneous spectral broadening or shifts in the water Larmor frequencies exist.

As the ‘proof of principle’, Fig. 6.10 demonstrates that it is also possible to selectively depict paramagnetic biopsy needles using the described positive contrast technique. A cylindrical object such as a biopsy needle will show a dipolar field if it is not oriented parallel to  $\vec{B}_0$ . However, at the needle tip, which geometry often deviates from a perfect cylindrical object, the magnetic field is perturbed although the needle is oriented parallel to  $\vec{B}_0$ .

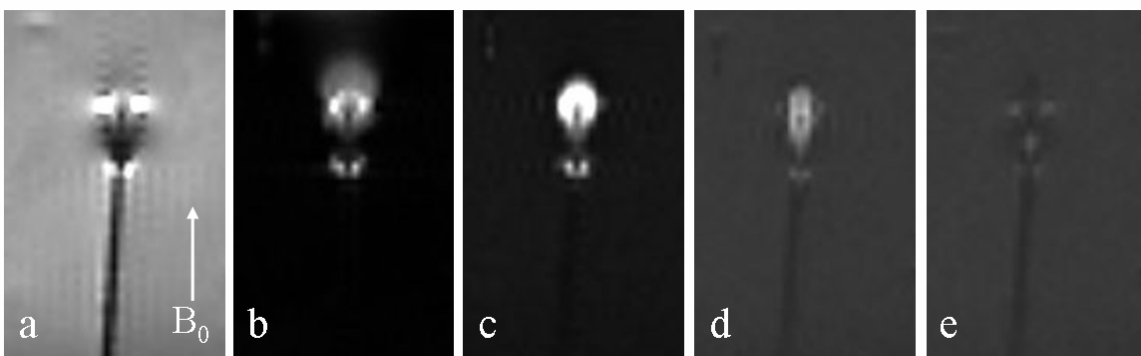


**Figure 6.10** (a) Selective depiction of a paramagnetic biopsy needle using a 2d spin echo MRI sequence. In (b-e) spectral selective saturation sinc pulses were implemented prior to each sequence repetition. The bandwidth  $BW_{\text{sat}}$  of the saturation pulse was varied: (b)  $BW_{\text{sat}} = 100$  Hz, (c)  $BW_{\text{sat}} = 200$  Hz, (d)  $BW_{\text{sat}} = 400$  Hz, (e)  $BW_{\text{sat}} = 800$  Hz.



Currently, ‘positive contrast imaging’ of magnetically labeled cells as an alternative contrast mechanism is a field of extensive research. Besides the application of spectral selective saturation, other positive contrast techniques have been reported, which are described below.

In the experiments by Seppenwoolde et al. [Sep03] and Bakker et al. [Bak06], the positive contrast resulted from dephasing the background signal with a slice gradient, while near magnetic markers the signal was conserved because the dipole field induced by the marker compensated the dephasing gradient. This technique is referred to as ‘dephased MRI’ [Bak06] and was treated as a mechanism for manipulating contrast in otherwise conventional MR images in order to track interventional devices and to trace magnetically labeled cells. The positive contrast generated has shown to be dependent on the intensity of the field distortion, the strength of the compensation gradient, the slice thickness, and the echo time [Sep03]. The efficacy of this technique was verified by Mani et al. [Mani06] by implementing a gradient echo sequence with a variable dephasing gradient. The principle of local gradient compensation is well known in the literature [Fra88, Rei97] and has been used in functional MRI to recover signal loss in brain regions that suffer from field inhomogeneities due to air cavities [Sep03].

Cunningham et al. [Cun05] used spectrally selective radiofrequency pulses to excite and refocus the off-resonance water surrounding magnetically labeled cells, while suppressing the on-resonance signal. This allowed for positive contrast imaging in regions affected by labeled cells. The field gradient induced by labeled cells and the respective spectral broadening was used to selectively excite and refocus a narrow band of resonance frequencies. This is similar in concept to slice-selective excitation, where a frequency selective rf pulse is applied in presence of a linear field gradient in order to select a particular slice. The concept has also similarities to the idea of spectrally selective saturation as described in the present work.

Zurkiya and Hu [Zur06] reported off-resonance saturation as a means of generating contrast with superparamagnetic nanoparticles. They demonstrated an alternative approach, termed ‘off-resonance’ saturation, for generating contrast that is sensitive to superparamagnetic particles. In this method, bulk water protons were imaged with and without off-resonance saturation, and the differences in MR images obtained were used as a measure to characterize the field inhomogeneity effect introduced by the SPIO. They demonstrated a calculated contrast

that increased with concentration of particles and, thus, reconfirmed the results obtained in the present work.

All these methods are based on the same physical mechanism: the magnetic field inhomogeneities and the respective Larmor frequency shifts near magnetically labeled cells. Under in vitro conditions, the positive contrast techniques described produced similar results and no major differences could be discerned. The application of 'positive contrast techniques' is an alternative approach to generate contrast in MRI and deserves further attention for use in localization of magnetically labeled cells.

It is anticipated that the application of the described approaches may allow for an improved MR imaging contrast under in vivo conditions, since the underlying physical principles are identical. However, in vivo conditions are more complex and usually deviate from those present in vitro. Since the reported techniques are sensitive to any local magnetic field gradient, other sources of field variation and magnetic susceptibility will give some residual signal. Furthermore, the partial dephasing in voxels at water-lipid boundaries as caused by the different resonance frequencies of the fat with respect to the water signal may also mimic magnetically labeled cells under in vivo conditions.

## Chapter 7

# Discussion and conclusions

This work contributed to the understanding of the magnetic field inhomogeneity effects induced by cells labeled with magnetic particles such as superparamagnetic iron oxide nanoparticles. The field distortions were studied systematically for distances smaller than the MRI voxel size (i.e., the microscopic scale) as well as for distances larger than the typical side length of an imaging voxel (i.e., the macroscopic scale). Studying field inhomogeneity effects related to labeled cells is of major importance for MRI because the respective field gradients cause proton spins to precess at different Larmor frequencies. It was demonstrated, that signal dephasing effects and Larmor frequency shifts can be exploited to generate image contrast as the mean to detect magnetically labeled cells.

Furthermore, the relaxation effects of intra- and extracellular contrast agents were studied systematically for various concentrations of contrast agents and at different magnetic field strengths. In order to improve the image contrast or to optimize the sensitivity and the specificity of MRI to detect magnetically labeled entities, such a systematic study is crucial to establish optimal parameters for MR pulse sequences at each magnetic field strength. Specifically, the described sample preparation technique allowed for non-aggregated magnetically labeled cells in suspension. This enabled studying concentration dependent relaxation and magnetic field inhomogeneity effects in isolation. The proposed preparation technique is a simple and reliable approach to quantify relaxation and signal dephasing effects introduced by magnetically labeled cells.

## *DISCUSSION AND CONCLUSIONS*

It was pointed out that gradient echo sequences are more sensitive to magnetically labeled cells and the respective field distortions than spin echo sequences. Since for a given magnetic field strength the observed gradient echo cellular transverse relaxivities are significantly higher than the spin echo cellular relaxivities, it is anticipated that the physical system is in the static dephasing regime, in which signal dephasing is dominated by the magnetic field inhomogeneity effects and diffusion averaging can be neglected. In that case, the largest susceptibility induced effect is due to static line broadening in the gradient echo experiment. This static dephasing regime was considered for the subsequent numerical simulations.

In addition, the marginal increases in spin echo and gradient echo transverse relaxation enhancement observed at 3 Tesla as compared to 1.5 Tesla are thought to be due to saturation effects of the SPIO magnetization. Under *in vivo* conditions, however, tissue specific magnetic field gradients will generally increase with field strength. This implies that inherent field inhomogeneities compete with SPIO field distortions at higher field strengths. These may even mimic the appearance of labeled cells under *in vivo* conditions in tissues with complex magnetic field distributions, for example due to substructures with variations in magnetic susceptibility.

It was demonstrated, that the magnetic field created by a SPIO loaded cell is sensitive to its shape and intracellular distribution of magnetic moments only in close proximity to the cell. The magnetic field around a cell labeled with iron oxide nanoparticles is in good agreement with the magnetic dipole field. The intensity of the magnetic field distortion is determined by the effective magnetization of the cell, which is given by the density of magnetic nanoparticles per volume of cell. Far from the cell, the induced magnetic field cannot be distinguished from the magnetic field created by a spherical particle with the same total magnetic moment. However, close to the cell the magnetic field depends on the actual intracellular distribution of magnetic particles. As based on the findings of this work, it is anticipated that the field distortions caused by magnetic spheres characterize the magnetic field around iron oxide loaded cells precisely, providing the volume fraction of labeled cells per imaging voxel is sufficiently small. This seems reasonable for the most *in vitro* as well as *in vivo* applications.

Utilizing the SPIO induced signal reduction as the mean for detection one may assume that the sensitivity to detect labeled cells is higher in case of intense magnetic field

inhomogeneities. As shown by numerical simulations, cells with the magnetic label at the cell's surface were found to induce more intense magnetic field distortions as compared to cells with SPIO compartmentalized within the intracellular space. Thus, receptor mediated labeling of cells with magnetic nanoparticles may induce sufficiently high local magnetic field inhomogeneities and, hence, may be a promising approach from the magnetic field point of view.

A numerical model was applied under static dephasing conditions. It was demonstrated that the MR signal decay is significantly affected by the spatial distribution of magnetic dipoles within the MR volume element. It is anticipated that this fact is of critical importance for the reliable *in vivo* quantification of magnetically labeled cells, implying that in tissues with different spatial distributions of identical iron oxide or cell concentrations, different resonance frequency distributions and significant variations in the MR signal decay characteristics may be observed. In addition, the results provide reasonable explanations for non-monoexponential signal decay observed in liver tissue with iron overload (e.g., due to hemochromatosis) and following administration of superparamagnetic intracellular contrast media such as iron oxide nanoparticles.

It was revealed that non-monoexponential signal decay can result directly from magnetic field inhomogeneities and particle clustering in subcompartments. The geometrical arrangement of the subcompartments is expected to be important. It was figured out that smaller magnetic dipoles are likely to be more effective in terms of static relaxation enhancement as compared to larger magnetic dipoles for an identical volume fraction of magnetic material, due to the more intense magnetic field inhomogeneity effects.

The present study contributes to the understanding of the geometry as well as the extension of signal voids in static dephasing MRI induced by aggregations of magnetically labeled cells. In order to study the physical characteristics of these signal voids basic sequence parameters like echo time, voxel size, and plane of view orientation have been varied over a wide range in numerical simulations and *in vitro* MR measurements. The results are considered to be of paramount importance in optimizing MR sequence parameters with regard to spatial accuracy and sensitivity to detect cluster of labelled cells *in vitro* or even *in vivo*.

## *DISCUSSION AND CONCLUSIONS*

The spatial accuracy to detect cluster of magnetically labeled cells is of inferior quality the longer the echo time and the larger the size of the imaging voxel, respectively. The choice of long echo times and large voxel sizes prevents for a precise localization of labeled cells in the MR image and may cause significant overestimation of the volume of labeled cells under in vivo conditions. In contrast, the increase in the image signal void with echo time and voxel size may allow the detection of even lower concentrations of labeled cells. It is of crucial importance that the relative enhancement of the signal void with echo time was found to be independent of magnetization, and should also be independent of cell concentration under in vivo conditions.

In vivo conditions with respect to the microscopic magnetic field distribution as well as relaxation rate constants are likely to be different from that of the homogenous agar gel phantom. The quantitative assessment of the signal void in dependence on the SPIO concentration as well as the measurement parameters under in vivo conditions seems nevertheless possible, because the underlying physical principles are identical. Knowing the effect of the local magnetization on the extension of signal voids will be crucial in assessing numbers of labeled cells experimentally. On the basis of the proposed empirical quantification well-suited tissue models can be developed in order to test the sensitivity of MRI to verify labeled cells in tissue.

Finally, the Larmor frequency shift near magnetically labeled cells was exploited to achieve positive contrast. It was demonstrated, that selective imaging with positive contrast techniques is a highly promising solution to detect magnetically labeled cells. The resultant 'positive contrast' is the opposite of the 'negative contrast', which results from signal dephasing due to magnetic field inhomogeneity effects. In the present work, positive contrast imaging was achieved for volume elements containing labeled cells as well as for volume elements close to aggregations of labeled cells. The significant increase in the contrast-to-noise ratio using positive contrast techniques may be preferable for the precise localization of cells and determining their spatial distribution by means of an alternative contrast mechanism.

It was demonstrated that this contrast inversion and selective visualization of iron loaded cells requires only a small modification of conventional MR imaging techniques, allowing the technique to be integrated in various imaging protocols. In the current work, a frequency selective saturation pulse was implemented in a 2d spin echo sequence. It is anticipated, that

## *DISCUSSION AND CONCLUSIONS*

this concept can be generalized to various types of magnetic field distortions, as long as spectral broadening due to magnetic field inhomogeneities exists. As the ‘proof-of-principle’ it was demonstrated that paramagnetic biopsy needles can be selectively depicted using the described positive contrast technique.

The application of positive contrast techniques is an alternative approach to generate tissue contrast in MRI and deserves further attention for use in localization of magnetically labeled cells. However, because the techniques are sensitive to any local magnetic field gradient, other sources of field variation and magnetic susceptibility differences affect the imaging process under in vivo conditions.

The findings of this work, both experimental data and data obtained from numerical simulations, are anticipated to be transferable to each type of cell, since the physics describing magnetic field inhomogeneity and signal dephasing effects is indifferent to cell type. Furthermore, the theoretical and the in vitro results are anticipated to apply under in vivo conditions, since the underlying physical principles are comparable.

# References

- [Alex96] Alexander AL, McCreery TT, Barerre TR, Gmitro AF, Unger EC 1996 Microbubbles as novel pressure-sensitive MR contrast agents *Magn Reson Med* **35** 801-806
- [And53] Anderson PW, Weiss PR 1953 Exchange narrowing in paramagnetic resonance *Rev Mod Phys* **25** 269-276
- [Arb05] Arbab AS, Yocum GT, Rad AM, Khakoo AY, Fellowes V, Read EJ, Frank JA 2005 Labeling of cells with ferumoxides-protamine sulphate complexes did not inhibit function or differentiation capacity of hematopoietic or mesenchymal stem cells *NMR Biomed* **18** 533-559
- [Bak06] Bakker CJG, Seppenwoolde JH, Vincken KL 2006 Dephased MRI *Magn Reson Med* **55** 92-97
- [Ban97] Banci L, Bertini I, Luchinat C. Nuclear and electron relaxation. Weinheim, Germany: VHC Verlagsgesellschaft mbH; 1991:138.
- [Bau99] Bauer WR, Nadler W, Bock M, Schad LR, Wacker C, Hartlep A, Ertl G 1999 Theory of the BOLD effect in the capillary region: an analytical approach for the determination of T2 in the capillary network of myocardium *Magn Reson Med* **41** 51-62
- [Bel91] Belliveau JW, Kennedy DN, McKinstry RC, Buchbinder BR, Weisskoff RM, Cohen MS, Vevea JM, Brady TJ, Rosen BR 1991 Functional mapping of the human visual cortex by magnetic resonance imaging *Science* **254** 716-719
- [Bha92] Bhagwandien R, van Ee R, Beersma R, Bakker CJG, Moerland MA, Lagendijk JJW 1992 Numerical analysis of the magnetic field for arbitrary magnetic susceptibility distributions in 2d *Magn Reson Imaging* **10** 299-313
- [Blo46] Bloch F, Hansen W, Packard M 1946 Nuclear induction *Phys Rev* **70** 460-485



## REFERENCES

- [Bow02] Bowen CV, Zhang X, Saab G, Gareau PJ, Rutt BK 2002 Application of the Static Dephasing Regime Theory to Superparamagnetic Iron-Oxide Loaded Cells *Magn Reson Med* **48** 52-61
- [Bri04] Briley-Saebo K, Bjornerud A, Grant D, Ahlstrom H, Berg T, Kindberg GM 2004 Hepatic cellular distribution and degradation of iron oxide nanoparticles following single intravenous injection in rats: implications for magnetic resonance imaging *Cell Tiss Res* **316** 315-323
- [Bro61] Brown RJS 1961 Distribution of fields from randomly placed dipoles: free precession signal decay as a result from magnetic grains *Phys Rev* **121** 1379-1382
- [Buck04] Buckel W, Kleiner R 2004 *Supraleitung Wiley VHC* 6<sup>th</sup> edition
- [Bul97] Bulte JWM, Miller GF, Vymazal J, Brooks RA, Frank JA 1997 Hepatic hemosiderosis in non-human primates: quantification of liver iron using different field strengths *Magn Reson Med* **37** 530-536
- [Bul99] Bulte JWM, Brooks RA, Moskowitz BM, Bryant Jr LH, Frank JA 1999 Relaxometry and magnetometry of the MR contrast agent MION-46L *Magn Reson Med* **42** 379-384
- [Bul04] Bulte JWM, Kraitchman DL 2004 Iron oxide MR contrast agents for molecular and cellular imaging *NMR Biomed* **17** 484-499
- [Case87] Case TA, Durney CH, Ailion DC, Gutillo AG, Morris AH 1987 A mathematical model of diamagnetic line broadening in lung tissue and similar heterogeneous systems: calculations and measurements *J Magn Reson* **73** 304-314
- [Cav97] Cavagna FM, Maggioni F, Castelli PM 1997 Gadolinium chelates with weak binding to serum proteins: A new class of high-efficiency, general purpose contrast agents for magnetic resonance imaging *Invest Radiol* **32** 780-796
- [Che01] Cheng YC, Haacke EM, Yu YJ 2001 An exact form for the magnetic field density of states for a dipole *Magn Reson Imaging* **19** 1017-1023
- [Cun05] Cunningham CH, Arai T, Yang PC, McConnell MV, Pauly JM, McConolly SM 2005 Positive contrast magnetic resonance imaging of cells labeled with magnetic nanoparticles *Magn Reson Med* **53** 999-1005
- [Dal03] Daldrup-Link HE, Rudelius M, Oostendorp RAJ, Settles M, Piontek G, Metz S, Rosenbrock H, Keller U, Heinzmann U, Rummeny EJ, Schlegel J, Link TM 2003 Targeting of Hematopoietic Progenitor Cells with MR Contrast Agents *Radiology* **228** 760-767

## REFERENCES

- [Dal05] Daldrup-Link HE, Rudelius M, Piontek G, Metz S, Bräuer R, Debus G, Corot C, Schlegel J, Link TM, Peschel C, Rummeny EJ, Oostendorp RAJ 2005 Migration of iron-oxide labeled human hematopoietic progenitor cells in a mouse model: in vivo monitoring with 1.5-T MR imaging equipment *Radiology* **234** 197-205
- [Dam71] Damadian R 1971 Tumor detection by Nuclear Magnetic Resonance *Science* **171** 1151-1153
- [DeHa99] De Haen C, Cabrini M, Akhnana L, Ratti D, Calabi L, Gozzini L 1999 Gadobenate Dimeglumine 0.5 mM Solution for injection (MultiHance): Pharmaceutical formulation and physico-chemical properties of a new magnetic resonance imaging contrast medium *J Comput Assisted Tomogr* **23** 161-168
- [DeVr05] De Vries IJM, Lesterhuis WJ, Barentz JO, Verdijk P, Van Krieken JH, Boerman OC, Oyen WJG, Bonenkamp JJ, Boezeman JB, Adema GJ, Bulte JWM, Scheenen TWJ, Punt CJA, Heerschaap A, Fidgor CG 2005 Magnetic resonance tracking of dendritic cells in melanoma patients for monitoring of cellular therapy *Nat Biotechnol* **23** 1407-1413
- [Enn06] Ennis DB, Kindlmann G 2006 Othogonal tensor invariants and the analysis of diffusion tensor magnetic resonance images *Magn Reson Med* **55** 136-146
- [Falk05] Falkenhausen M, Meyer C, Lutterbey G, Morakkabati-Spitz N, Gieseke J, Reichel C, Blömer R, Kuhl CK, Schild HH 2005 Contrast enhanced MRI of the liver with SPIO at 3 T. Does higher field strength translate into higher contrast? *Roefo* **177** 582
- [Fra88] Frahm J, Merboldt KD, Hanicke W 1988 Direct FLASH MR imaging of magnetic field inhomogeneities by gradient compensation *Magn Reson Med* **6** 474-480
- [Fram87] Fram EK, Herfkens RJ, Johnson GA, Glover GH, Karis JP, Shimakawa A, Perkins TG, Pelc NJ 1987 Rapid calculation of T1 using variable flip angle gradient refocused imaging *Magn Reson Imaging* **5** 201-208
- [Fis91] Fisel CR, Ackerman JL, Buxton RB, Garrido L, Belliveau JW, Rosen BR, Brady TJ 1991 MR Contrast Due to Microscopically Heterogeneous Magnetic Susceptibility: Numerical Simulations and Applications to Cerebral Physiology *Magn Reson Med* **17** 336-347
- [Ford93] Ford JC, Wehrli FW, Chung HW 1993 Magnetic field distribution in models of trabecular bone *Magn Reson Med* **31** 9-21
- [Gie06] Giesel FL, von Tengg-Kobligk H, Wilkinson ID 2006 Influence of human serum albumin on longitudinal and transverse relaxation rates of MR contrast agents *Invest Radiol* **41** 222-228

## REFERENCES

- [Gill87] Gillis P, Koenig SH 1987 Transverse relaxation of solvent protons induced by magnetized spheres: application to ferritin, erythrocytes, and magnetite *Magn Reson Med* **5** 323-345
- [Gill02] Gillis P, Moyny F, Brooks RA 2002 On T2-shortening by strongly magnetized spheres: a partial refocusing model *Magn Reson Med* **47** 257-263
- [Graf03] Graf H, Martirosian P, Schick F, Grieser M, Bellemann ME 2003 Inductively coupled rf coils for examinations of small animals and objects in standard whole-body MR scanners *Med Phys* **30** 1241-1245
- [Haa86] Haase A, Frahm J, Merboldt KD 1986 FLASH Imaging. Rapid NMR imaging using low flip-angle pulses *J Magn Reson* **67** 258-266
- [Har89] Hardy PA, Henkelman RM 1989 Transverse Relaxation Rate Enhancement Caused by Magnetic Particulates *Magn Reson Imaging* **7** 265-275
- [Heyn06] Heyn C, Ronald JA, Mackenzie LT, MacDonald I, Chambers AF, Rutt BK, Foster PJ 2006 In Vivo Magnetic Resonance Imaging of Single Cells in Mouse Brain with Optical Validation *Magn Reson Med* **55** 23-29
- [Him04] Himes N, Min JY, Lee R, Brown C, Shea J, Huang X, Xiao YF, Morgan JP, Burstein D, Oettgen P 2004 In vivo MRI of embryonic stem cells in a mouse model of myocardial infarction *Magn Reson Med* **52** 1214-1219
- [Hoe02] Hoehn M, Küstermann E, Blunk J, Wiedermann D, Trapp T, Wecker S, Föcking M, Arnold H, Hescheler J, Fleischmann BK, Schwandt W, Bührle C 2002 Monitoring of implanted stem cell migration in vivo: A highly resolved in vivo magnetic resonance imaging investigation of experimental stroke in rat *Proc Natl Acad Sci USA* **99** 16267-16272
- [Hup04] Huppertz A, Rohrer M 2004 Gadobutrol, a highly concentrated MR-imaging contrast agent: its physicochemical characteristics and the basis for its use in contrast-enhanced MR angiography and perfusion imaging *Eur Radiol* **14** [Suppl 5] M12-M18
- [Jen02] Jensen JH, Chandra R 2002 Theory of Nonexponential NMR Signal Decay in Liver With Iron Overload or Superparamagnetic Iron Oxide Particles *Magn Reson Med* **47** 1131-1138
- [Jen03] Jendelova P, Herynek V, DeCroos J, Glogarova K, Andersson B, Hajek M, Sykova E 2003 Imaging the fate of implanted bone marrow stromal cells labeled with superparamagnetic nanoparticles *Magn Reson Med* **50** 767-776

## REFERENCES

- [Jung95] Jung CW, Jacobs P 1995 Physical and chemical properties of superparamagnetic iron oxide MR contrast agents: ferumoxides, ferumoxtran, ferumoxsil *Magn Reson Imaging* **13** 661-674
- [Kal93] Kaldoudi E, Williams SCR 1993 Relaxation Time Measurements in NMR Imaging Concepts *Magn Reson* **5** 217-242
- [Kal00] Kaller K 2000 NC100150 injection, a preparation of optimized iron oxide nanoparticles for positive-contrast MR angiography *J Magn Reson Imaging* **11** 488-494
- [Ken94] Kennan RP, Zhong J, Gore JC 1994 Intravascular Susceptibility Contrast Mechanism in Tissues *Magn Reson Med* **31** 9-21
- [King95] Kingsley PB 1995 Magnetic field gradients and coherence pathway elimination *J Magn Reson Series B* **109** 243-250
- [Kir03] Kirchin M, Runge VM 2003 Contrast agents for magnetic resonance imaging: safety update *Top Magn Reson Imaging* **14** 426-435
- [Kis99] Kiselev VG, Posse S 1999 Analytical model of susceptibility-induced MR signal dephasing: effect of diffusion in a microvascular network *Magn Reson Med* **41** 499-509
- [Kno98] Knollmann FD, Bock JC, Rautenberg K, Beier J, Ebert W, Felix R 1998 Differences in predominant enhancement mechanism of superparamagnetic iron oxide and ultrasmall superparamagnetic iron oxide for contrast enhanced portal magnetic resonance angiography: preliminary results of an animal study investigation *Invest Radiol* **33** 637-643
- [Lau73] Lauterbur PC 1973 Image formation by induced local interactions: examples employing Nuclear Magnetic Resonance *Nature* **242** 190-191
- [Lau86] Lauterbur PC, Bernardo ML, Mendonca-Dias MH, Hedges LK 1986 Microscopic NMR Imaging of the magnetic fields around magnetite particles *Proc Soc Magn Reson Med* 229-230
- [Lau06] Laurent S, Vander Elst L, Muller RN 2006 Comparative study of the physicochemical properties of six clinical low molecular weight gadolinium contrast agents *Contrast Med Mol Imaging* **1** 128-137
- [Law97] Lawaczeck R, Bauer H, Frenzel T, Hasegawa M, Ito Y, Kito K, Miwa N, Tsutsui H, Vogler H, Weinmann HJ 1997 Magnetic iron oxide particles coated with carboxydextran for parenteral administration and liver contrasting. Pre-clinical profile of SH U 555A *Acta Radiologica* **38** 584-597

## REFERENCES

- [Li01] Li L 2001 Magnetic susceptibility quantification for arbitrarily shaped objects in inhomogeneous fields *Magn Reson Med* **46** 907-916
- [Lüd85] Lüdke KM, Röschmann P, Tischler R 1985 Susceptibility Artefacts in NMR Imaging *Magn Reson Imaging* **3** 329-343
- [Mac87] MacFall JR, Wehrli FW, Breger RK, Johnson GA 1987 Methodology for the measurement and analysis of relaxation times in proton imaging *Magn Reson Imaging* **5** 209-220
- [Mani06] Mani V, Briley-Saebo KC, Itskovich VV, Samber DD, Fayad ZA 2006 Gradient echo Acquisition for Superparamagnetic particles with Positive contrast (GRASP): Sequence Characterization in Membrane and Glass Superparamagnetic Iron Oxide Phantoms at 1.5 T and 3 T *Magn Reson Med* **55** 126-135
- [Man73] Mansfield P, Grannell PK 1973 NMR diffraction in solids *J Phys C: Solid State Phys* **6** L422-L427
- [Mat05] Matuszewski L, Persigehl T, Wall A, Schwindt W, Tombach B, Fobker M, Poremba C, Ebert W, Heindel W, Bremer C 2005 Cell Tagging with Clinically Approved Iron Oxides: Feasibility and Effect of Lipofection, Particle Size, and Surface Coating on Labeling Efficiency *Radiology* **235** 155-161
- [Mes06] Meschede D 2006 Gerthsen Physik *Springer* **23** edition
- [Metz04] Metz S, Bonaterra G, Rudelius M, Settles M, Rummeny EJ, Daldrup-Link HE 2004 Capacity of human monocytes to phagocytose approved iron oxide MR contrast agents in vitro *Eur Radiol* **14** 1851-1858
- [Mue04] Müller-Bierl B, Graf H, Lauer U, Steidle G, Schick F 2004 Numerical modelling of needle tip artifacts in MR gradient echo imaging *Med Phys* **31** 579-587
- [Mue05] Müller-Bierl B, Graf H, Steidle G, Schick F 2005 Compensation of magnetic field distortions from paramagnetic instruments by added diamagnetic material: Measurements and numerical simulations *Med Phys* **32** 76-84
- [Oga90] Ogawa S, Lee TS, Glynn P 1990 Oxygenation-sensitive contrast in Magnetic Resonance Imaging of rodent brain at high magnetic fields *Magn Reson Med* **14** 68-78
- [Paul36] Pauling L, Coryell CD 1936 The magnetic properties and structure of hemoglobin, oxyhemoglobin, and carbonmonooxyhemoglobin *Proc Natl Acad Sci USA* **22** 210-216

## REFERENCES

- [Pint05a] Pintaske J, Helms G, Bantleon R, Kehlbach R, Wiskirchen J, Claussen CD, Schick F 2005 A preparation technique for quantitative investigation of SPIO-containing solutions and SPIO-labeled cells by MRI *Biomed Techn* **19** 46-53
- [Pint05b] Pintaske J, Martirosian P, Claussen CD, Schick F 2005 Positive contrast in the detection of magnetically labeled cells by MRI – in vitro experiments *Biomed Techn* **50** 271-276
- [Pint06a] Pintaske J, Müller-Bierl B, Schick F 2006 Effect of spatial distribution of magnetic dipoles on Larmor frequency distribution and MR Signal decay: a numerical approach under static dephasing conditions *Magn Reson Mater Phys* **19** 46-53
- [Pint06b] Pintaske J, Bantleon R, Kehlbach R, Claussen CD, Wiskirchen J, Schick F 2006 Effect of Concentration of SH U 555A Labeled Human Melanoma Cells on MR Spin Echo and Gradient Echo Signal Decay at 0.2 T, 1.5 T, and 3 T *Magn Reson Mater Phys* **19** 71-77
- [Pint06c] Pintaske J, Müller-Bierl B, Schick F 2006 Geometry and extension of signal voids in MR images induced by aggregations of magnetically labeled cells *Phys Med Biol* **51** 4707-4718
- [Pint06d] Pintaske J, Martirosian P, Graf H, Erb G, Lodemann KP, Claussen CD, Schick F 2006 Relaxivity of gadopentetate dimeglumine (Magnevist), gadobutrol (Gadovist) and gadobenate dimeglumine (MultiHance) in human blood plasma at 0.2 T, 1.5 T and 3 T *Invest Radiol* **41** 213-221
- [Pint06e] Pintaske J, Müller-Bierl B, Schick F 2006 Field perturbations by magnetic dipoles as a model for magnetically labelled cells in MRI *Z Med Phys* **16** 252-260
- [Port05] Port M, Corot C, Violas X, Robert P, Raynal I, Gagneur G 2005 How to compare the efficiency of albumin-bound and nonalbumin contrast agents in vivo: the concept of dynamic relaxivity *Invest Radiol* **40** 565-573
- [Pre92] Press WH, Teukolsky Sa, Vetterling WT, Flanery BP 1992 Numerical recipes in C – the art of scientific computing. 2<sup>nd</sup> edn. Cambridge University Press, Cambridge
- [Pur46] Purcell EM, Torrey HC, Pound RV 1946 Resonance absorption by nuclear magnetic moments in a solid *Phys Rev* **69** 37-38
- [Rei97] Reichenbach JR, Venkatesan R, Yablonskiy DA, Thompson MR, Lai S, Haacke EM 1997 Theory and application of static field inhomogeneity effects in gradient-echo imaging *J Magn Reson Imaging* **7** 266-279
- [Roch99] Roch A, Muller RN 1999 Theory of proton relaxation induced by superparamagnetic particles *J Chem Phys* **110** 5403-5411

## REFERENCES

- [Roh05] Rohrer M, Bauer H, Mintorovitch J, Requardt M, Weinmann HJ 2005 Comparison of magnetic properties of MRI contrast media solutions at different magnetic field strengths *Invest Radiol* **40** 715-724
- [Sae98] Saeed M, Wendland MF, Engelbrecht M, Sakuma H, Higgins CB 1998 Value of blood pool contrast agents in magnetic resonance angiography of the pelvis and lower extremities *Eur Radiol* **8** 1047-1053
- [Sch96] Schick F, Lutz O 1996 Assessment of the magnetic field distribution in yellow and red bone marrow by the MAGSUS technique *Magn Reson Imaging* **14** 507-519
- [Sch05] Schick F 2005 Whole-body MRI at high field: technical limits and clinical potential *Eur Radiol* **15** 946-959
- [Sch96] Schenck JF 1996 The role of magnetic susceptibility in magnetic resonance imaging: MRI magnetic compatibility of the first and second kinds *Med Phys* **23** 816-850
- [Shel06] Shellock FG 2006 Reference manual for magnetic resonance safety, implants, and devices *Biomedical Research Publishing Group*
- [Sep03] Seppenwoolde JH, Viergever MA, Bakker CJG 2003 Passive tracking exploiting local signal conservation: the white marker phenomenon *Magn Reson Med* **50** 784-790
- [Sep05] Seppenwoolde JH, von Zijtveld M, Bakker CJG 2005 Spectral characterization of local magnetic field inhomogeneities *Phys Med Biol* **50** 361-372
- [Sha06] Shapiro EM, Sharer K, Skrtic S, Koretsky AP 2006 In Vivo Detection of Single Cells by MRI *Magn Reson Med* **55** 242-249
- [Sim06] Simon GH, Bauer J, Saborovski O, Fu Y, Corot C, Wendland MF, Daldrup-Link HE 2006 T1 and T2 relaxivity of intracellular and extracellular USPIO at 1.5 T and 3 T clinical MR scanning *Eur Radiol* **16** 738-745
- [Sta88] Stark DD, Weissleder R, Elizondo G, Hahn PF, Saini S, Todd LE, Wittenberg J, Ferucci JT 1988 Superparamagnetic iron oxide: clinical application as a contrast agent for MR imaging of the liver *Radiology* **168** 297-301
- [Stroh05] Stroh A, Faber C, Neuberger T, Lorenz P, Sieland K, Jakob PM; Webb A, Pilgrimm H, Schober R, Pohl EE, Zimmer C 2005 In vivo detection limits of magnetically labeled embryonic stem cells in the rat brain using high field (17.6 T) magnetic resonance imaging *Neuroscience* **24** 635-645

## REFERENCES

- [Suk03] Sukstanskii AL, Yablonskiy DA 2003 Gaussian approximation in the theory of MR signal formation in the presence of structure-specific magnetic field inhomogeneities *J Magn Reson* **163** 236-247
- [Tan01] Tanimoto A, Oshio K, Suematsu M, Pouliquen D, Stark DD 2001 Relaxation effects of clustered particles *J Magn Reson Imaging* **14** 72-77
- [Tan98] Tanimoto A, Yuasa Y, Hiramatsu K 1998 Enhancement of phase-contrast angiography with superparamagnetic iron oxide *J Magn Reson Imaging* **8** 446-450
- [Tau03] Taupitz M, Schmitz S, Hamm B 2003 Superparamagnetische Eisenoxidpartikel: Aktueller Stand und zukünftige Entwicklungen *Fortschr Roentgenstr* **175** 752-765
- [Thom92] Thomsen C, Wiggers P, Ring-Larsen H, Christiansen E, Dalhoj J, Henriksen O, Christoffersen P 1992 Identification of patients with haemochromatosis by magnetic resonance imaging and spectroscopic relaxation time measurements *Magn Reson Imaging* **10** 867-879
- [US03] U.S. Department of Health and Human Services, Food and Drug Administration, Center for Devices and Radiological Health, Guidance for Industry and FDA Staff. Criteria for Significant Risk Investigations of Magnetic Resonance Diagnostic Devices, July 14, 2003
- [Van01] Vander Elst L, Chapelle F, Laurent S, Muller RN 2001 Stereospecific binding of MRI contrast agents to human serum albumine: the case of Gd-(S)-EOB-DPTA (Eovist) and its (R) isomer *J Biol Inorg Chem* **6** 196-200
- [Wag02] Wagner S, Schnorr J, Pilgrim H, Hamm B, Taupitz M 2002 Monomer-coated very small superparamagnetic iron oxide particles as contrast medium for magnetic resonance imaging: Pre-clinical in vivo characterization *Invest Radiol* **37** 167-177
- [Wang01] Wang YXJ, Hussain SM, Krestin GP 2001 Superparamagnetic iron oxide contrast agents: physicochemical characteristics and applications in MR imaging *Eur Radiol* **11** 2319-2331
- [Wei90] Weissleder R, Elizondo G, Wittenberg J, Lee AS, Josephson L, Brady TJ 1990 Ultrasmall superparamagnetic iron oxide: an intravenous contrast agent for assessing lymph nodes with MR imaging *Radiology* **175** 494-498
- [Wei94] Weisskoff RM, Zho CS, Boxerman JL, Rosen BR 1994 Microscopic susceptibility variation and transverse relaxation: theory and experiment *Magn Reson Med* **31** 601-610
- [Yab94] Yablonskiy DA, Haacke EM 1994 Theory of NMR Signal Behavior in Magnetically Inhomogeneous Tissues: The Static Dephasing Regime *Magn Reson Med* **32** 749-763



## REFERENCES

- [Yab98] Yablonskiy DA 1998 Quantitation of Intrinsic Magnetic Susceptibility-Related Effects in a Tissue Matrix. Phantom Study *Magn Reson Med* **39** 417-428
- [Yung03] Yung KT 2003 Empirical models of transverse relaxation for spherical magnetic perturbers *Magn Reson Imaging* **21** 451-463
- [Zha05] Zhang Z, van den Bos EJ, Wielopolski PA, de Jong-Popijus M, Bernsen MR, Duncker DJ, Krestin GP 2005 In vitro imaging of single living human umbilical vein endothelial cells with a clinical 3.0-T MRI scanner *Magn Reson Mater Phys* **18** 175-185
- [Zie05a] Ziener CH, Bauer WR, Jakob PM 2005 Transverse Relaxation of Cells Labeled With Magnetic Nanoparticles *Magn Reson Med* **54** 702-706
- [Zie05b] Ziener CH, Bauer WR, Jakob PM 2005 Frequency distribution and signal formation around a vessel *MAGMA Magn Reson Mater Phys* **18** 225-230
- [Zur06] Zurkiya O, Hu X 2006 Off-Resonance Saturation as a Means of Generating Contrast with Superparamagnetic Nanoparticles *Magn Reson Med* **56** 728-732

## Journal papers

Lichy M, Pintaske J, Kottke R, Machann J, Anastasiadis A, Roell S, Hennenlotter J, Diergarten T, Schick F, Stenzl A, Claussen CD, Schlemmer HP  
**3D Proton MR spectroscopic imaging of prostate cancer using a standard spine coil at 1.5 T in clinical routine: a feasibility study**  
Eur Radiol 15: 653 - 660 (2005)

Pintaske J, Helms G, Bantleon R, Kehlbach R, Wiskirchen J, Claussen CD, Schick F  
**A preparation technique for quantitative investigation of SPIO-containing solutions and SPIO-labelled cells**  
Biomed Techn 50: 174 - 180 (2005)

Pintaske J, Martirosian P, Claussen CD, Schick F.  
**Positive contrast in the detection of magnetically labeled cells by MRI – in vitro experiments**  
Biomed Techn 50: 271-276 (2005)

Pintaske J, Müller-Bierl B, Schick F  
**Effect of spatial distribution of magnetic dipoles on Larmor frequency distribution and MR signal decay – a numerical approach under static dephasing conditions**  
Magn Reson Mater Phy 19: 46-53 (2006)

Pintaske J, Martirosian P, Graf H, Erb G, Lodemann KP, Claussen CD, Schick F  
**Relaxivity of gadopentetate dimeglumine (Magnevist), gadobutrol (Gadovist) and gadobenate dimeglumine (MultiHance) in human blood plasma at 0.2 T, 1.5 T and 3 T**  
Invest Radiol 41: 213-221 (2006)

Pintaske J, Bantleon R, Kehlbach R, Claussen CD, Wiskirchen J, Schick F  
**Effect of concentration of SH U 555A labeled human melanoma cells on MR spin echo and gradient echo signal decay at 0.2 T, 1.5 T, and 3 T**  
Magn Reson Mater Phy 19: 71-77 (2006)

Pintaske J, Müller-Bierl B, Schick F

**Geometry and extension of signal voids in MR images induced by aggregations of magnetically labelled cells**

Phys Med Biol 51: 4707-4718 (2006)

Pintaske J, Müller-Bierl B, Schick F

**Field perturbations by magnetic dipoles as a model for magnetically labelled cells in MRI**

Z Med Phys 16: 252-260 (2006)

Oppitz M, Pintaske J, Kehlbach R, Busch C, Schriek G, Schick F

**Magnetic resonance imaging of iron-oxide labelled SK-Mel 28 human melanoma cells in the chick embryo using a clinical whole body MRI scanner**

Magn Reson Mater Phy (2007), in press

Schäfer R, Kehlbach R, Wiskirchen J, Bantleon R, Pintaske J, Brehm R, Schick F, Claussen CD

**Transferrin-Receptor Up Regulation in vitro of Rat Mesenchymal Stem Cells by Labeling with Superparamagnetic Iron Oxide Contrast Agent**

Radiology (2007), in press

# Curriculum Vitae

## Zur Person

---

Name: Jörg Pintaske  
Geburtsdatum: 17. August 1980  
Geburtsort: Marienberg  
Nationalität: Deutsch

## Bisheriger Bildungsweg

---

1992 - 1999 Gymnasium Marienberg, Abitur  
1999 - 2004 Studium „Medizinische Physik“ an der Martin-Luther-Universität Halle-Wittenberg  
2003 - 2004 Diplomarbeit im Studiengang „Medizinische Physik“, angefertigt in der Abteilung für Radiologische Diagnostik, Universitätsklinikum Tübingen, unter der Anleitung von Prof. Dr. Dr. Fritz Schick  
2004 Abschluss als Diplom-Physiker  
2004 - 2007 Anfertigung der Dissertation „Magnetic field distribution and relaxation effects in the presence of interstitial and intracellular contrast agents for magnetic resonance imaging“ in der Abteilung für Radiologische Diagnostik, Universitätsklinikum Tübingen, unter der Anleitung von Prof. Dr. Dr. Fritz Schick

Meine akademischen Lehrer während meiner Ausbildung waren: Berg, Braun, Carl, Dräger, Dunst, Fischer, Gerlach, Graener, Heiliger, Hempel, Hergert, Höche, Jenderka, Leipner, Louis, Mertig, Pluschke, Reichert, Renelt, Schick, Stölzer, Tannert, Trimper, Wagner

# Danksagung

Prof. Dr. Dr. Fritz Schick begleitete mich während der Dissertation stets in einer sehr freundlichen Art und Weise und gab mir die Freiheit zum selbstständigen Arbeiten und Erfahrungen sammeln im *Ozean der Wissenschaft*. Besonders wertvoll waren seine konkreten Hilfestellungen zur systematischen Bearbeitung selbst scheinbar undurchdringlicher Probleme.

Wesentliche Ergebnisse dieser Arbeit verdanke ich den Vorarbeiten von Herrn Dr. Bernd Müller-Bierl, welcher mich in die Simulation und Berechnung der hier analysierten Feldverteilungen einweihte, mich hervorragend unterstützte und zahlreiche nützliche Vorschläge unterbreitete.

Ein besonderer Dank gebührt Herrn Dipl.-Phys. Petros Martirosian. Seine stets aufgeschlossene und zuvorkommende Art in der Diskussion physikalischer Probleme war für die erfolgreiche und zügige Bearbeitung der Dissertation von grundlegender Bedeutung.

Eine fruchtbare Zusammenarbeit bei den Versuchsreihen mit Zellkulturen und Tiermodellen ergab sich durch die Initiativen von Dr. Rüdiger Bantleon, Dr. Rainer Kehlbach, Dr. Matthias Oppitz und PD Dr. Jakob Wiskirchen.

Herr Dipl.-Phys. Jürgen Machann gab mir einen Einblick in die kulinarische und musikalische Kulturlandschaft des amerikanischen Kontinents.

Den Herren Graf, Machann, Martirosian und Schick danke ich für ausführliches Korrekturlesen der vorliegenden Arbeit.

Allen hier nicht persönlich aufgeführten Mitgliedern der Sektion für Experimentelle Radiologie und der Abteilung für Radiologische Diagnostik sei ebenfalls herzlichst gedankt.

Ohne Zweifel mein größter Dank gilt meinen Eltern, welche mich stets, auch in etwas schwierigeren *Sturm und Drang Perioden*, bedingungslos unterstützt haben.

Von unschätzbarem Wert ist Sabine als die *wirkliche Welt* außerhalb des Berufslebens, und nicht nur das.